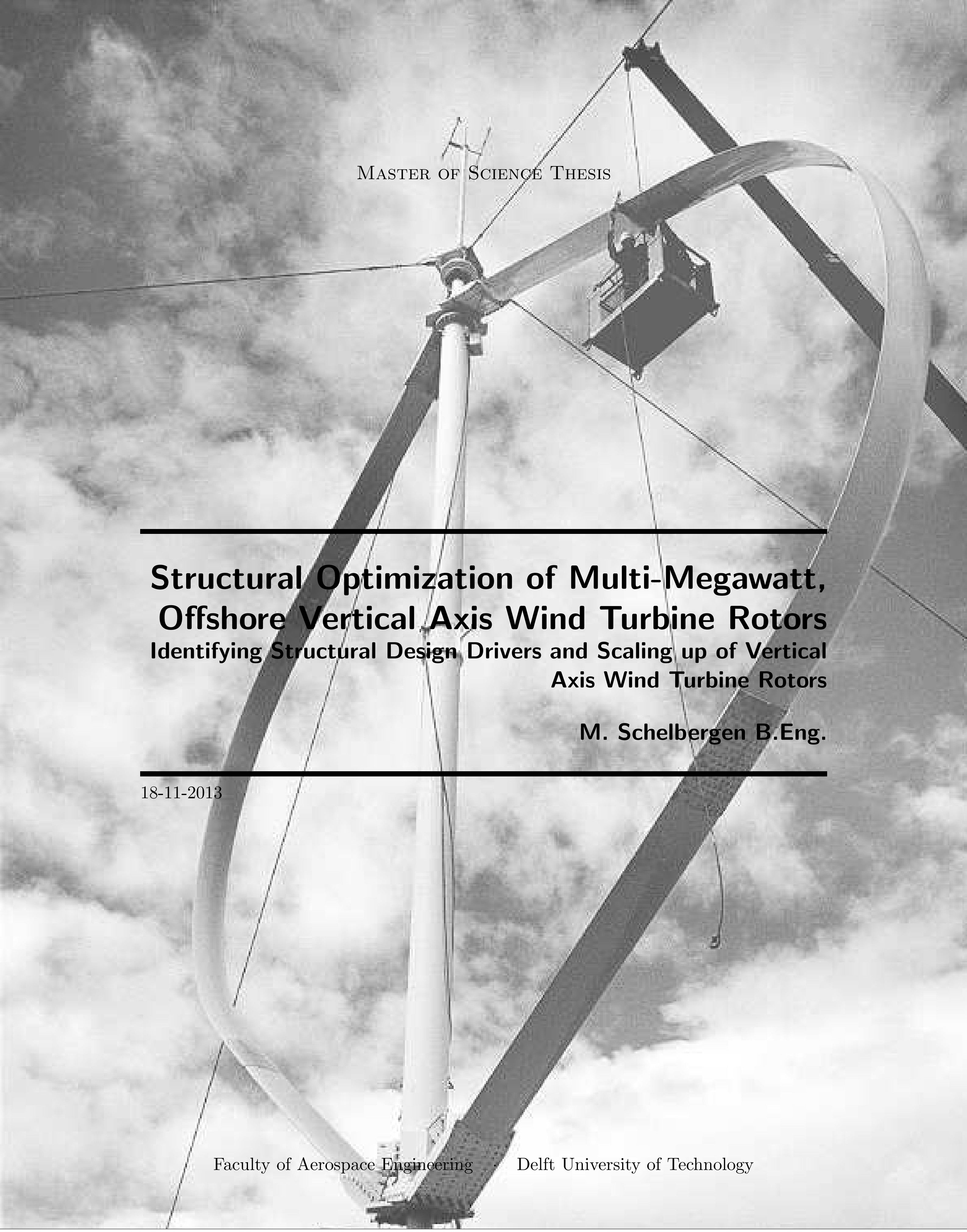

Master of Science Thesis

Structural Optimization of Multi-Megawatt, Offshore Vertical Axis Wind Turbine Rotors

Identifying Structural Design Drivers and Scaling up of Vertical Axis Wind Turbine Rotors

M. Schelbergen B.Eng.

18-11-2013

Faculty of Aerospace Engineering · Delft University of Technology

TU Delft Delft University of Technology

Challenge the future

Structural Optimization of Multi-Megawatt, Offshore Vertical Axis Wind Turbine Rotors

Identifying Structural Design Drivers and Scaling up of Vertical Axis Wind Turbine Rotors

Master of Science Thesis

For obtaining the degree of Master of Science in Aerospace Engineering at Delft University of Technology

M. Schelbergen B.Eng.

18-11-2013

Faculty of Aerospace Engineering · Delft University of Technology

Delft University Of Technology
Department Of
Wind Energy

The undersigned hereby certify that they have read and recommend to the Faculty of Aerospace Engineering for acceptance a thesis entitled **"Structural Optimization of Multi-Megawatt, Offshore Vertical Axis Wind Turbine Rotors"** by **M. Schelbergen B.Eng.** in partial fulfillment of the requirements for the degree of **Master of Science**.

Dated: 18-11-2013

Head of department: ______________________
Prof. Dr. G.J.W. Van Bussel

Supervisors: ______________________
Dr. Ir. C.J. Simão Ferreira

____
Ir. L.O. Bernhammer

Reader: ______________________
Dr. Ir. R. De Breuker

Abstract

The knowledge about Vertical Axis Wind Turbines (VAWT) lags behind the knowledge about Horizontal Axis Wind Turbines (HAWT), since most of the development of VAWT's ceased after the 80's. A lack of insight exists about how certain design parameters affect the rotor design of a modern VAWT. The objective of this thesis is to gain knowledge about the influence of the size (power capacity) of the turbine on the structural rotor performance of multi-megawatt VAWT's by optimizing the rotor design. The influence of the size is expressed by scaling trends. The scope is limited to the structural design of the rotor blade and struts.

The major loads on the rotor structure are aerodynamic, gravitational, and centrifugal loads. Fatigue, buckling, and resonance are the failure modes driving the design of the VAWT rotor. Modern manufacturing techniques of composite materials are believed to have a significant effect on the VAWT rotor design, since they offer more flexibility in the blade geometry. The mass increase of the blades is identified as a limiting factor for upscaling wind turbines.

Gradient-based optimizations are performed to find the optimum 3-bladed H-rotor and Darrieus rotor designs for different rotor sizes and heights. The structural rotor performance is assessed by the ratio of the rotor mass over projected area. The laminate thicknesses and the shape of the rotor structure are varied in search of the optimum performance. A constant tip speed ratio and blade solidity is imposed on the optimization. Furthermore, constraints are imposed to prevent failure of the rotor structure.

Optimizations of the VAWT rotor are performed for rotor sizes ranging from 3 MW to 20 MW. Rotor mass reductions for the carbon-fiber 20 MW H-VAWT and Darrieus VAWT of respectively 35% and 44% are obtained with respect to the fiberglass HAWT rotors. Despite this mass reduction, the material cost of the HAWT rotor will be significantly smaller. The optimized VAWT rotors are rough approximations of the best design solutions because of restrictions on the design space. In general, expanding the design space of the optimization yields better design solutions. In future VAWT rotor design optimization, the design space should allow for a variable diameter-to-height ratio of the rotor, since this parameter is driving the structural rotor performance.

Acknowledgements

I wish to thank my supervisors Carlos Simão Ferreira and Lars Bernhammer for their support throughout my thesis. The weekly meetings, valuable discussions, and motivational speeches helped me a lot in the progress of my thesis.

I like to thank Etana Ferede for providing me with his geometrical blade representation. Furthermore I like to thank him for the time he put into helping me enhancing his code and to apply it to the optimization.

Last, but not least, I want to thank my family and friends for their patience during my thesis.

Delft, The Netherlands
18-11-2013

M. Schelbergen B.Eng.

Contents

Nomenclature

Latin Symbols

$\mathbf{A}_{CLT}$	Membrane stiffness matrix from classical laminate theory	
A	Projected rotor area	[m^2]
a	Curve coefficient of power curve fit	
b	Curve exponent of power curve fit	
C_p	Power coefficient	
C_t	Tangential aerodynamic force coefficient	[-]
$\mathbf{c}_{eq}$	Equality constraints	
$\mathbf{c}_{ineq}$	Inequality constraints	
c	Chord	[m]
$\mathbf{D}_{CLT}$	Bending stiffness matrix from classical laminate theory	
D	Rotor diameter	[m]
D_{MR}	Fatigue damage following Miner's rule	
E	Annual energy yield	[Wh]
E_{xx}	Young's modulus in x-direction	[Pa]
E_{yy}	Young's modulus in y-direction	[Pa]
F_t	2D tangential aerodynamic force	[N/m]
$\mathrm{f}_{\mathrm{mesh}}$	Mesh factor	
f_V	Wind speed probability	
G_{xy}	Shear modulus	[Pa]
h	Height	[m]
J	Objective function	

M	Bending moment	[Nm]
m	Mass	[kg]
N	Number of allowable load cycles	
n	Number of occuring load cycles	
R	Rotor radius	[m]
R_σ	Stress ratio of stress cycle: $\frac{\sigma_{min}}{\sigma_{max}}$	
P	Power capacity	[W]
p	Mean stress exponent in the expression of the S-N curve	
S	Allowable (shear) stress	[Pa]
s	Length along the blade	[m]
T	Torque	[Nm]
T_{oper}	Total number of operational hours per year	[h]
t	Laminate thickness	[m]
V	Wind speed	[m/s]
v_{xy}	Poisson ratio	
w	Width	[m]
X_c	Allowable compressive stress in x-direction	[Pa]
X_t	Allowable tensile stress in x-direction	[Pa]
$\mathbf{x}$	Design vector	
Y_c	Allowable compressive stress in y-direction	[Pa]
Y_t	Allowable tensile stress in y-direction	[Pa]

Greek Symbols

α	Angle of attack	[°]
λ	Tip speed ratio	[-]
Ω	Rotational speed	[rad/s]
ρ	Density	[kg/m^3]
σ	Normal stress	[Pa]
$\Delta\sigma$	Amplitude of stress cycle	[Pa]

Abbreviations

ARIS	Aeronautical Research Institute of Sweden
BM	Blade Mode
CFRP	Carbon Fiber Reinforce Plastic
DW	Downwind

EV	Eigenvalue
FI	Failure index
GFRP	Glass Fiber Reinforced Plastic
HAWT	Horizontal Axis Wind Turbine
LC	Load Case
MDO	Multidisciplinary Design Optimization
NURBS	Non-Uniform Rational Basis Spline
P	Parked
S-N	The cyclic stress amplitude against the number of cycles to failure due to fatigue
SF	Safety Factor
SM	Strut Mode
SNL	Sandia National Laboratories
SQP	Sequential Quadratic Programming
UD	Uni-Directional tape
UW	Upwind
VAWT	Vertical Axis Wind Turbine

Chapter 1

Introduction

Wind power is an increasingly important source of sustainable energy. About every 3 years the wind power capacity is doubled. This makes wind power one of the fastest growing energy sources around the world. Energy is extracted from the wind by means of a wind turbine. A lot of wind turbine concepts have been developed through history. The Horizontal Axis Wind Turbine (HAWT) has evolved as the dominant type of wind turbine. A trend can be observed towards larger turbines to reduce the cost of wind energy. Although the size of onshore wind turbines appears to level out, the design development of larger wind turbines continues due to the development of an offshore wind turbine market. Offshore wind turbines are in general larger than onshore wind turbines to compensate for the relative high cost of the infrastructure (e.g. the foundation and the grid) and maintenance. These additional costs make it more economically viable to place fewer turbines with the same total capacity.

The blades of a HAWT are subject to a reversing internal load each revolution due to gravity. This cyclic load increases with the size of the turbine and is believed to be one of the main limiting factors for upscaling HAWT's due to fatigue [1]. In the blades of Vertical Axis Wind Turbines (VAWT) gravity does not cause such a cyclic load. However, aerodynamic blade loads do cause reversing internal loads each revolution. It is believed that the cyclic loads for VAWT's are less severe for the fatigue life of the turbine compared to the cyclic loads for HAWT's and therefore less of a limiting factor for further upscaling of wind turbines. Furthermore VAWT's have other inherent characteristics, which make them more favorable for offshore application:

- A VAWT does not require a yawing mechanism.
- Heavy systems of the turbine (such as the generator, gearbox, and brakes) are located at the bottom of the turbine, which provides relatively easy installation and maintenance.

The knowledge about VAWT's lags behind the knowledge about HAWT's, since most of the development of VAWT's ceased after the 80's. A lack of insight exists about how certain design parameters affect the rotor design of a modern VAWT.

The objective of this thesis is to gain knowledge about the influence of the size (power capacity) of the turbine on the structural rotor performance of multi-megawatt VAWT's by optimizing the rotor design. Next to the effect of the size, the effect of the diameter-to-height ratio of the rotor on the structural rotor performance is evaluated. The scope of this thesis is limited to the structural design of the rotor blade and struts; other structures and systems of the turbine are omitted in the optimization (e.g. the tower and the generator). The structural design of two rotor configurations are evaluated: the 3-bladed H-rotor and Darrieus rotor.

Gradient-based optimizations are performed to find the optimum structural rotor performance for different rotor sizes and heights. The structural rotor performance is assessed by the ratio of the rotor mass over projected area. The laminate thicknesses and the shape of the rotor structure are varied in search of the optimum performance. A constant tip speed ratio and blade solidity is imposed on the optimization, furthermore constraints are imposed to prevent failure of the rotor structure. A mathematical representation of the rotor geometry generates a finite element method (FEM) formulation of the geometry, which is used for analyzing the structure. The FEM analysis uses a pressure distribution to apply the aerodynamic load to the blade. The applied pressure distributions follow from the angles of attack seen by the blade provided by a 2D unsteady panel model simulation. The influence of the rotor size on the structural rotor performance and diameter-to-height ratio are expressed by scaling trends. Scaling trends are constructed by a power curve fit using data of the optimized rotor designs.

The body of the report starts in Chapter 2 with a historical overview of VAWT's, followed by a review of the relevant literature. Chapter 3 describes the structural model for the rotor optimization. First, the parameterization of the rotor geometry is explained. Second, the load cases and material strengths are covered. Finally, the FEM formulation of the geometry and application of the loads are discussed. Chapter 4 discusses the optimization approach taken. It elaborates on the optimization algorithms, objective function, design variables, and constraints. In Chapter 5 the results of the optimization are presented. A more thorough structural analysis is performed on these results, furthermore the results are used to construct scaling trends. The discussion of the results is presented in Chapter 6. The constructed scaling trends are compared with HAWT rotor scaling trends. Finally in Chapter 7, the methodology of the thesis is discussed, conclusions are drawn, and recommendations for future work are stated.

Chapter 2

Literature review

This chapter starts with a historical overview of VAWT's. The designs of the most important VAWT's built up to this date are discussed. Furthermore, some alternative VAWT concepts are discussed. Next, the structural design of wind turbine blades is addressed. The critical loading conditions and failure modes for which the blades need to be designed are covered, followed by the materials used in a wind turbine blade and the structural layout of a blade cross-section. Subsequently upscaling methods for wind turbines are discussed. Finally the multidisciplinary design optimization method is addressed.

2.1 Historical overview of vertical axis wind turbines

The work of Paraschivoiu [2] covers the general design of a VAWT and discusses the historical developments of the VAWT. The three most common VAWT's concepts are illustrated in Figure 2.1. The earliest VAWT's were drag based turbines. The first to introduce the idea of a lift based VAWT was G.J.M. Darrieus, who patented the concept in 1931 [2]: the Darrieus wind turbine. The rotor of the Darrieus wind turbine has curved blades fixed to the tower of the turbine on both ends, shown in the middle in Figure 2.1. The shape of the blades minimizes the internal flapwise bending moment due to the centrifugal load; the shape is called the Troposkien shape. Generally, the Darrieus wind turbine uses guy cables to stabilize the tower. These tensioned cables are mounted to the top of the tower and anchored to the ground at some distance from the tower. The third concept was mainly developed in the United Kingdom: the H-configuration VAWT, shown on the right in Figure 2.1. This section discusses the most important VAWT's built up to this date, followed by some alternative VAWT concepts.

2.1.1 Sandia National Laboratories turbines (United States)

Some of the most extensive research on VAWT's was performed by Sandia National Laboratories (SNL), the work of SNL is summarized by Sutherland et al. [3]. SNL built several

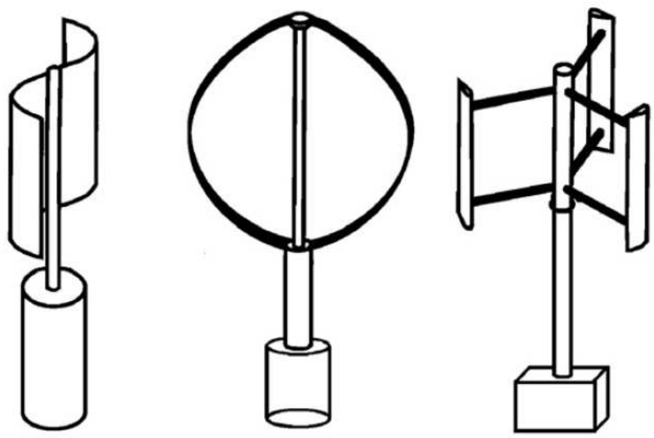

Figure 2.1: From left to right: Savonius rotor, Darrieus rotor and the H-rotor [1].

Darrieus-type VAWT's. In 1974 SNL built a research VAWT with a 5 m diameter, followed by a 17 m diameter turbine in 1977. In 1987 they built the 34 m diameter Test Bed turbine. This turbine was designed to serve as a research turbine and used to investigate the basic physics of wind turbines. Therefore, the design was very conservative and adaptable, such that different blades could be mounted to the machine. The machine was equipped with a lot of sensors by which a large number of measurements were obtained. The measurements were used to validate analysis techniques and design codes.

The Test Bed was variable speed and was designed to operate for rotor speeds between 28 and 38 rpm. A rotor speed of 37.5 rpm at a wind speed of 12.5 m/s, rated the turbine at 500 kW. The turbine used a NACA 0021 airfoil together with a SAND 0018/50 airfoil. The latter was specially designed for the wind turbine and its stall characteristics were designed to limit the power generation of the rotor at high wind speeds by stalling. The Test Bed turbine is illustrated in Figure 2.2.

The natural frequencies of the stationary turbine were determined using a modal test. The measured resonance frequencies agreed well with the predicted frequencies (almost all of them within 2%). The outcome determined the rotor speed operation range. One mode of guy cable resonance occurred at 36 rpm, which fell in the middle of the operation range of the rotor speed. This rotor speed, and thereby the resonance, was avoided with the use of a controller by quickly passing through the critical rotor speed range. In a later stage the guy cables were adjusted such that resonance occurred only outside the rotor speed operation range. A second resonance of the guy cables occurred at 25 rpm; this only needed to be avoided during start-up. The measured internal stresses in the blades agreed very well with the model predictions for the stationary turbine and the operative turbine. The measured data was used to provide one of the first measured fatigue load spectra; to give better insight in the fatigue of the structures.

The performance of the turbine also agreed very well with the predictions. However, its performance was unforeseen affected by the accumulation of insect remains on the blades, which formed during operation. The accumulation resulted in a delay of the blade stall, and thereby the rotor reached higher powers at wind speeds where normally stall would

Figure 2.2: Sandia Test Bed Turbine[a].

[a]Source: http://www.asme.org/, visited in October 2012.

occur. The effect of applying vortex generators near the outer blade connection and the blade-tower connection was tested, however no significant difference in performance was measured.

2.1.2 Canadian turbines

The largest VAWT up to today was built in 1986 in Canada: the Lavalin Eole Research Turbine. The paper of Richard et al. [4] discusses the design of the Eole. The two-speed Darrieus-type turbine had a 64 m diameter and a peak power output exceeding 1.3 MW (measured at a 14.7 m/s wind speed and a rotor speed of 11.35 rpm). The turbine was designed to have a variable speed and a maximum power output of 3.6 MW. In order to operate successfully for a 5 year energy purchase agreement, the rotor speed was limited to 13.25 rpm and the cut-out speed to 15 m/s because of fatigue. The turbine was shut down in 1993 due to premature failure of the bottom bearing (the design life of the turbine was 30 years). The Eole is illustrated in Figure 2.3.

Intermediate masts were applied to the guy cables to raise the natural frequencies of the cables. The blades of the turbine were manufactured in 5.7 m long straight sections; mounted together using bolted, spliced joints, such that the blade approximated a Troposkien shape. The three blade sections at the equator were equipped with aerodynamic brakes, which were actuated hydraulically additional to the mechanical brakes. The rotor was positioned on a concrete construction housing the power train. The construction needed to carry the weight of the rotor and the additional loads imposed by the guy cables.

2.1.3 FloWind turbines (United States)

FloWind was a commercial company operating and manufacturing Darrieus-type VAWT's from 1982 to 1997, supplying to the utility grid of the United States. They had a fleet

Figure 2.3: Lavalin Eole Research Turbine[a].

[a]Source: http://delta.tudelft.nl/, visited in October 2012.

of 170 turbines with a 19 m diameter and 250 kW power production at a wind speed of 20 m/s. In 1992 they developed a new rotor for their old fleet to improve fatigue and power production, as is discussed in the work of Sutherland et al. [3]. By improving the fatigue life of the rotor, the maintenance cost of their turbine decreased (the aluminum blades of the turbine required a lot of maintenance due to fatigue). Furthermore, the new rotor design increased energy yield without replacing the bases, gearboxes, and generators. This new rotor, called the extended height-to-diameter rotor, was based on the Sandia Point Design. The FloWind turbine is illustrated in Figure 2.4.

The number of blades for the retrofit rotor were increased to 3 and produced out of fiberglass. The blades were pultruded in sections of 48.2 m long and a constant chord of 0.69 m. The blades were bent-in-place to mount the blades on the rotor; this increased the out-of-plane bending moment in the blades. The slender blades required struts far away from the tower-blade mounting to decrease vibrations. The 3 bladed design reduced the size of the torque tube and improved the resonance stability significantly. From the Point Design it was concluded that the tower and its bearings have a major contribution to the total cost of the turbine. The costs for these parts were reduced significantly by improving the resonance stability. The blades went through some adjustments before they arrived to the final design. First a SNLA 2150 airfoil was used, which increased the rotor speed of the turbine to 60 rpm. This led to an early failure of the gearbox so another airfoil was used: the Somers S824, which would perform better at the original rotor speed of 52 rpm. The first blades produced with this airfoil needed to be redesigned with a larger skin thickness to avoid buckling. At first, in the redesign, struts were incorporated close to the blade roots. This design proved to be inadequate and the struts were positioned deeper (further away from the root).

Early studies of Sandia proved that a 3 bladed rotor was not cost effective, however the retrofit rotor proved differently. Improvement of the resonance stability of the rotor drove the design of the rotor when the rotor became very large. Therefore, for larger turbines adding a third blade was the most cost effective way to improve the resonance

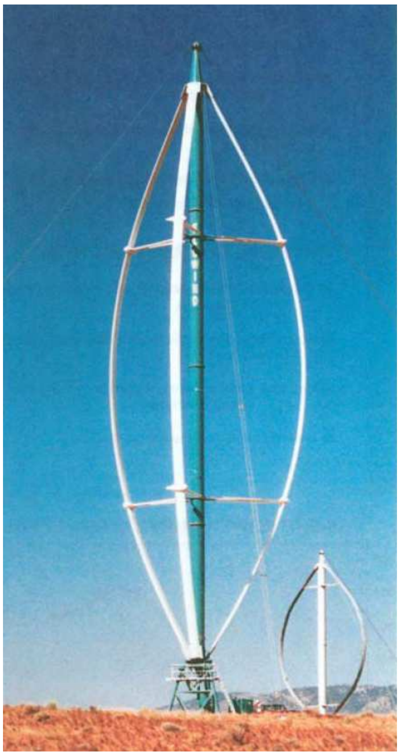

Figure 2.4: FloWind extended height-to-diameter rotor [3].

stability. The bend-in-place technique, used to mount the blades, reduced the fatigue life significantly. The deep struts decreased the aerodynamic performance of the design.

2.1.4 H-rotor turbines (United Kingdom)

The work of Mays et al. [5] discusses the design of the 500 kW VAWT 850 (35 m diameter) built in August 1990. This turbine is the successor of the research prototype VAWT 450 built at Carmarthen Bay Power Station and the demonstration VAWT 250 built on the Isles of Scilly, in 1986. The numbers in the name of the turbines indicate the swept area of the rotor. Initially the vertical axis wind turbine development program in the United Kingdom investigated the variable geometry rotor concept. Based on tests on the VAWT 450, it was concluded that there was no need to reef the blades for satisfactory control of the power output and blade loading (using passive stall regulation). Therefore, the VAWT 450 was no longer operated in the variable geometry mode. The VAWT 850 was built to show the advances made in the development of the H-type VAWT in the UK. The turbine did not have a large life time. One of the blades broke due to a manufacturing error in February 1991, after being in operation for approximately half an year [6].

The design philosophy of the VAWT 850 was to offer high reliability for its design life of 30 years and low cost through simplicity of the design. To minimize parasitic losses the blades were mounted to a horizontal arm at one point, connecting it to the rotor hub. A single bearing connected the rotor to the top of the tower, where all the systems of the turbine were positioned. The turbine operated at a single speed of 20.4 rpm and was

Figure 2.5: VAWT 450 with variable geometry; blades are in reefed position [6].

designed for a mean wind speed of 8 m/s. The length of the blades and the mean chord length were respectively 24.3 m and 1.75 m. The blades used the NACA 0018 profile and were manufactured out of fiberglass, using two spars and a load carrying skin.

The blades were mounted to the rotor arm through a flanged, bolted connection, which was covered with an aerodynamic fairing. The rotor arm consisted of three parts with rectangular cross-sections, which together had a length of 35 m. A NACA 0030 fairing was fitted over the outer part of the rotor arm to minimize parasitic losses. The tower of the turbine was a post tensioned cylindrical concrete tube with an outside diameter of 3.5 m and a wall thickness of 250 mm. Notice that in contrast to the previous discussed turbines, the H-rotor turbines do not use guy cables. The absence of guy cables is beneficial for offshore application of the turbine.

2.1.5 Alternative concepts

Some alternative VAWT concepts were explored by amongst others the Aeronautical Research Institute of Sweden (ARIS). The work of Ljungstrom [7] discusses the L-180 Poseidon concept. This concept had a 180 m diameter, a rated power of maximum 20 MW at a maximum operation wind speed of 25 m/s, and operated at a single rotor speed of 6.4 rpm. The total mass of the turbine was estimated to be about 13,000 tonnes. The L in the name of the concept stands for its shape when seen from above; it has two blades mounted at a relative 90 degree angle (in contrast to the earlier discussed 2 bladed turbines, for which the blades were mounted at a relative 180 degree angle). This configuration mitigated the rotor thrust oscillations, carried by the tower and the foundation. Furthermore, the torque ripple is smoothened out compared to the conventional configuration.

The concept incorporated a bi-blade configuration (two airfoil cross-sections in one blade cross-sections), as earlier demonstrated on Vestas VAWT's. This configuration significantly increased the bending stiffness of the blade and lowered the mass. An aerodynamic penalty was paid compared to a mono-blade configuration. The use of a mono-blade design would have increased the chord from 2.25 m to 4.5 m and result in a blade weight increase of 65%. The spacing between the blades was 2.3 m and the blades were interconnected every 38 m.

Finally the concept incorporated an alternative transmission: a rotor-ring-bearing-transmission. The cantilever rotor-tower was attached to a large diameter ring of 60 m supported by a large number of horizontal rollers, of which some were driving the generator. The rotor-ring-bearing carried the bending moment induced by the rotor thrust such that guy cables could be omitted from the design. Besides that, the configuration provided a direct one-step transmission from rotor speed to favorable generator speed. To the knowledge of the author no attempts were made to realize this concept.

Succeeding work of Ljungstrom [8] discusses other concepts investigated by the ARIS. First of all, the 3X-Triol concept was developed to smoothen out the thrust load on the blade. This concept utilized swept Troposkien blades (spiral Troposkien), which were able to reduce the blade load peaks by 65%-70% relative to unswept Troposkien blades. The design incorporated 6 blades; 3 with a positive sweep angle and 3 with a negative sweep angle. A blade with a positive sweep and a blade with a negative sweep formed a pair. The pair met at the rotor equator, where they were joined together. Another concept was proposed to mount the machine to the ground, to improve the structural efficiency: the Inclined-Shaft-Tripod. One strut of the tripod functioned as the centre column of the rotor and met the other two supporting struts at the top of the rotor. An inclination of the first strut, and thereby the rotor, of 26.5 degrees caused approximately a 3% reduction in energy yield relative to the non-inclined turbine.

At the ARIS also the Y- or V-configuration VAWT was investigated for offshore application. This configuration was earlier developed by amongst others Sharpe et al. [9]. The name of the configuration refers to the geometry of the rotor where the (straight) blades move along the surface of an upside down cone. The V-configuration requires only a short tower. The root of the blades are mounted with a hinge to the rotor hub at the vertex of the cone, a second connection of the blade with the hub is located further along the blade. The hinged connection enables the blades to be raised and lowered; making erection, inspection, and maintenance relatively simple. For a given swept area of the rotor, the blades of the V-configuration VAWT need to be longer than for other VAWT configurations. The blades however do not have to be heavier because of the way they are supported. The optimal cone angle of the blades is found to be 45 degrees. The V-configuration VAWT has good self-starting capabilities because of the high starting torque compared to other VAWT configurations. ARIS contributed to the V-configuration VAWT by proposing a system to sweep the blades of the turbine in high winds to smoothen out the thrust loads on the blades.

2.2 Structural wind turbine blade design

Safe operation of the wind turbine during its design life is a general requirement on the wind turbine. This requirement imposes constraints on the design of the turbine system and its subsystems, such as the rotor. For the rotor blade, these constraints are formulated based on the loading conditions to which they can be exposed and the failure modes which can occur. The loading conditions and the failure modes should be well understood when designing a wind turbine blade. The constraints need to be satisfied by altering the materials used in a wind turbine blade and the structural layout of a blade cross-section.

This section addresses the most important aspects of the structural design of wind turbine blades. The critical loading conditions and failure modes for which the blades need to be designed are covered. Finally, the materials used in a wind turbine blade and the structural layout of a blade cross-section are covered.

2.2.1 Loading conditions for vertical axis wind turbines

Raciti Castelli et al. [10] worked on a numerical method to perform the combined aerodynamic and structural analysis of an H-configuration VAWT blade. The emphasis of the paper is put on assessing the contributions of the aerodynamic and inertial loads to the stresses and deformations of the blade in normal operation. The paper evaluates different skin thicknesses of the blade; the contribution of the inertial load to the blade displacement seems to be dominant over the aerodynamic load for all the evaluated skin thicknesses. In the upwind position of the blade it is observed that the aerodynamic loads are almost constant along the length of the blade, except for the aerodynamic loads at the tip (as expected). On the other hand, for the downwind position of the blade, it is observed that both the direction and the magnitude of the aerodynamic load are changing significantly. To understand the exact reason for this phenomenon further research is recommended by the authors. Furthermore, it is recommended by the authors to analyze the aeroelastic effect on the performance of the turbine, in particular the influence of the deformation of the airfoil geometry to the performance of the turbine.

The loads experienced by the rotor during normal operation as discussed in the last paragraph are of great importance for determining the fatigue life of the rotor. As is stressed by Sutherland et al. [3], fatigue is very important for wind turbines as for a 30-year life the structures typically need to withstand at least 10^9 cycles. For VAWT blades the radial aerodynamic loads change sign every revolution, and therefore have a dominant role in the fatigue life of the blade of a VAWT.

A more complete example of the considered static and fatigue load cases in the design of a VAWT is presented by Reimerdes [11] and stated in Table 2.1. It should be noted that the specified load cases were set up for the design of relatively small VAWT of 20 kW power at a wind speed of 7 m/s.

Table 2.1: Load cases for a 20 kW VAWT [11].

No.	Load case	Cycles	Wind velocity [m/s]	Horizontal gust [m/s]	Vertical gust [m/s]	Rotational speed factor
1	Normal operation	1	15	15	$\pm$ 7.6	1.3
2	Normal operation	3e8	15	10	$\pm$ 7.6	1.2
3	Parked (ice load: 7 [kN/m^3])	1e2	44.2	-	$\pm 5°$ wind incidence	-
4	Parked (snow load: 0.75 [kN/m^2])	1e2	44.2	-	$\pm 5°$ wind incidence	-
5	Starting	2e3	15	10	-	0.6
6	Braking (air brakes)	1	15	15	-	1.3
7	Braking (mechanical brakes)	2e3	15	10	-	1.2
8	Emergency braking (mechanical brakes)	1	15	15	-	1.3

In the work of Touryna et al. [12] three major load cases for VAWT rotors are identified, listed below. The latter load cases are all covered in Table 2.1. Therefore, the load cases in the table should form a good basis for the design of a larger VAWT, however the stated values may need to be reconsidered.

1. The blades subjected to aerodynamic and gravitational loads for parked rotor conditions at high winds.

2. The blades subjected to aerodynamic, gravitational and centrifugal loads during normal operation.

3. The rotor tube subjected to aerodynamic, blade, cable and gravitational loads for parked rotor conditions at high winds.

2.2.2 Critical failure modes

Years of knowledge about wind turbine design of HAWT's has been gathered in design standards. The most critical failure modes for the blades stated in the standards are blade tip deflection, buckling, fatigue, and aeroelastic instability. The failure modes for VAWT blades differ from the failure modes for HAWT blades. For exmpale the tip deflection will be more critical for HAWT blades, since the VAWT blades have more tower clearance.

Fatigue is for both turbine types a design driver. In normal operation, the blades experience in each revolution a reversing load in the blade causing fatigue. The causes of these cyclic loads for HAWT's and VAWT's are respectively the gravitational loads and the aerodynamic loads. Structural joints are prone to fatigue and require extra attention in evaluating fatigue.

Structural resonance is also an often recurring failure mode for VAWT's in literature. The work of Berg [13] on the design of the Sandia Test Bed extensively discusses resonance of the turbine. In the design process the focus is put mainly on determining the resonance frequencies of the turbine systems. The operating ranges of the rotor speed for the evaluated design concepts are all strongly limited because of resonance. The work of Touryna et al. [12] further elaborates on the possible causes of resonance. Four major causes are stated and have been listed below.

1. Aerodynamic excitations at multiples of the rotor speed.

2. Aerodynamic excitations due to the stochastic nature of the wind.

3. Aerodynamic excitations on the downwind blade due to shed vortices at the rotor tower.

4. Aeroelastic excitations due to flutter. (The flutter speeds tend to be 2 to 3 times greater than the operating rotor speeds.)

A similar analysis to that of Berg is performed by Malcolm [14] for the Indal 6400 VAWT. In his paper, written in 1986, Malcolm concludes: "Progress in the technology of the blade manufacturing will greatly affect the configuration selected." Based on this conclusion it is expected that modern technologies will lead to different rotor designs.

2.2.3 Applied materials and structural layout of a blade

For the design of a wind turbine blade a complex trade-off study needs to be performed between several interlinked aspects. These aspects are geometry, materials and production process. The geometry of the rotor structure can not be optimized without taking into account the applied materials and the production process.

The material of choice for the earlier VAWT's blades was metal: the Sandia Test Bed used aluminum for their blades and the Eole used steel. The blades of the Sandia Test Bed were manufactured by extrusion and subsequently permanently bend to obtain the Troposkien shape. Both turbines utilized a step-tapered chord configuration. In later designs, full composite blades were introduced; the blades of both the FloWind extended height-to-diameter rotor and the VAWT 850 were made from Glass Fiber Reinforced Plastics (GFRP). For manufacturing the blades of the FlowWind turbine, a pultrusion method was used. The blades were bend-in-place to obtain the Troposkien shape. Manufacturing techniques of composite (horizontal axis) wind turbine blades have progressed a lot in the last decades. Modern manufacturing techniques offer more flexibility in the blade geometry.

Composites do not only offer more flexibility in the blade geometry, also the mechanical properties of a laminate can be altered. The stiffness and strength of composite laminates in any direction can be tailored to meet the requirements of a design. The laminates are tailored by controlling the fiber orientations in the laminate. In Table 2.2 a typical weight breakdown is provided of the used materials in a 48.8 m (2.5 MW) HAWT blade of approximately 10.7 tonnes.

Table 2.2: Weight break-down of a HAWT blade [15].

Material	Weight contribution
Dry fibers	
$45°/-45°/0°$	24%
$\pm 45°$	2%
UD	25%
Resin	34%
Paste	2%
Steel	2%
Rest	9%

In Table 2.3 the structural members are listed of a typical structural layout of a wind turbine blade together with their function in the structure. The structural members are illustrated in Figure 2.6. Table 2.3 states the dominant fiber angles in the laminates applied to the structural members. GFRP (E-glass/Epoxy) is the most common composite material applied in wind turbine blades. In the work of Ashuri [16], the mass increase of the blades for large turbines is identified as a limiting factor for upscaling HAWT's. Ashuri believes the application of Carbon Fiber Reinforce Plastics (CFRP) is a good design solution to reduce mass of the blades. The blades of VAWT's carry large inertial loads. The use of CFRP in VAWT blades could reduce the mass, and thereby the inertial loads, significantly.

Table 2.3: Structural members of a wind turbine blade [15].

Structural member	Function	Dominant fiber angles in laminate	Remarks
Spars/shear webs	Carrying mainly transverse loads	±45°	Large thickness (40-50 mm)
Spar caps/girders	Carrying mainly bending loads	0°	Sandwich
Skin	Directly subjected to the aerodynamic loads, responsible for transferring the loads	±45°	Sandwich

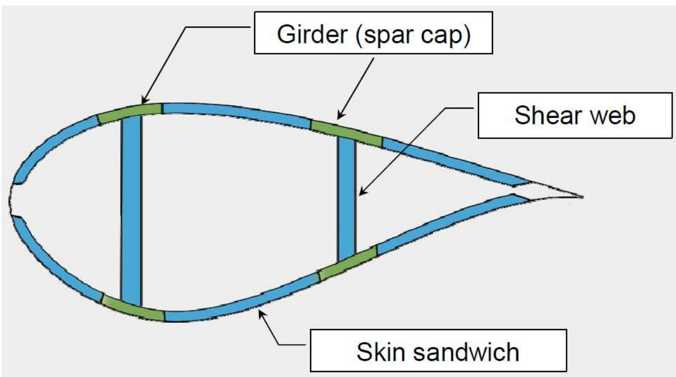

Figure 2.6: A typical structural layout of a blade section [15].

2.3 Upscaling methods of wind turbines

To the knowledge of the author, not a lot of past research is performed on developing scaling laws for VAWT's. However, for HAWT's there is a lot of research performed on developing scaling laws. Therefore, this section will focus mainly on the literature on scaling laws for HAWT's.

Linear scaling laws are defined by formulating analytical relations between important parameters (blade mass, energy yield, et cetera) as a function of the rotor diameter of the turbine. The analytical relations assume that all geometrical parameters scale linearly (blade chord, thickness et cetera). The important parameters are used to determine the cost of energy of the turbine. The size for minimum cost of energy of the turbine indicates the optimum turbine size. Another approach is studying the trends of existing turbines. However, for evaluating relatively large turbine sizes, which do have not been realized up to this date, extrapolation is required. Extrapolation is prone to misjudgments, furthermore the amount of VAWT data available is limited compared to HAWT's. Most of the data that is available is dated and would not be representative for modern turbines.

The work of Ashuri [16] compares linear scaling laws and the trends in existing turbines for, amongst others, the mass of the blade. Linear scaling law shows the mass of the blade is a function of the radius cubed. The trends in existing turbines show the mass of the blade is a function of the radius to the power 2.09. The lower curve exponent of the existing trend compared to the linear scaling law can be explained due to better design and manufacturing techniques developed in the last years. The linear scaling law approximates the rated power output quite well. From the linear scaling law it follows that the rated power output is function of the radius squared. The trends in existing turbines show that the rated power is function of the radius to the power 1.85. This good correlation can be explained by the aerodynamic design of the turbines, which reached a level of maximum achievable efficiency.

The linear scaling law is especially useful in the early stages of the design of a wind turbine to get an understanding of the scaling phenomenon. However, for investigating the technical feasibility of a turbine both scaling laws are insufficient. Therefore, Ashuri opts for a new approach for defining a scaling law. Multidisciplinary design optimizations are used to deliver three wind turbine designs of different sizes, from which scaling trends can be deduced. The three designs are obtained by optimizing for the cost of energy of the turbine. The design variables set the external blade and tower geometry, the thicknesses of the structures, and the rated rotor speed. A power curve is fitted to the data of the resulting three designs, illustrating the new scaling law.

2.4 Multidisciplinary design optimization

Traditional design methodologies are focused on finding a good design which satisfies the design requirements. In the design process a lot of repetitive human actions are required to find a good design. Different designs need to be analyzed, which requires iteration. Often a design analysis consist of multiple disciplines, amongst others: aerodynamics, structural mechanics, and control for wind turbines. These disciplines are interacting, which also requires iteration between the disciplines to yield a consistent design analysis. These repetitive actions are very labor intensive, also because each discipline has its own tool operated by a specialist. Automation of this multidisciplinary design analysis enables a numerical optimization. Multidisciplinary Design Optimization (MDO) uses an optimization algorithm to explore the design space of the problem, in search of the optimal design. In the process a lot of possible designs are evaluated and scored by an objective function. The objective function uses the outcomes of the automatically controlled tools to assess the designs. MDO aims at finding, not just a good; but the best design solution by minimizing the value of the objective function.

In MDO the design problem is mathematically represented, in order to perform a numerical optimization. The objective function J, represents the function which needs to be minimized for finding the optimal design. A set of design variables $\mathbf{x}$, needs to be composed, of which the objective is a function. During the optimization the design variables are altered in an attempt to proceed to the optimal solution. The design space (possible solutions) is limited by equality, inequality constraints (respectively $\mathbf{c}_{eq}$ and $\mathbf{c}_{ineq}$) and bounds. A simple optimization problem can be formulated as followed:

$$\begin{aligned} \underset{\mathbf{x}}{\text{minimize}} \quad & J(\mathbf{x}) \\ \text{subject to} \quad & c_{ineq,i}(\mathbf{x}) \leq 0, \; i = 1, \ldots, m \\ & c_{eq,j}(\mathbf{x}) = 0, \; j = 1, \ldots, n \\ & \mathbf{x}_{lower} \leq \mathbf{x} \leq \mathbf{x}_{upper} \end{aligned} \tag{2.1}$$

The mathematical representation of the complex system requires the actual system to be expressed by a confined set of parameters. This set of parameters needs to enable the generation of a complete and relevant specification of the model. To limit the number of design variables for representing the geometry of the turbine; properties parameters of lines and surfaces are used instead of defining a large number of points. The lines and surfaces can be parameterized with the use of, amongst others, shape functions.

To enable analyzing the complex system it may be beneficial to divide the overall system into a set of sub-systems, such that the sub-systems can be evaluated individually. It is common to use the different disciplines as sub-systems. As stated before, these disciplines interact, therefore they require some form of coordination to ensure a consistent system. Different coupling strategies are developed for amongst others portability reasons, such that different sub-systems can easily be programmed by different specialist. It is required to have a good understanding of the coupling such that a sound coupling strategy can be applied. A good coupling strategy can increase the computational efficiency of the optimization.

2.5 Research objective

The main objective of this thesis is to gain knowledge about the influence of the size of the turbine on the structural rotor performance of multi-megawatt VAWT's by optimizing the rotor design. To achieve this objective, an answer is sought to the question: How do the structural failure modes restrict the shape of the rotor? To answer this question, the

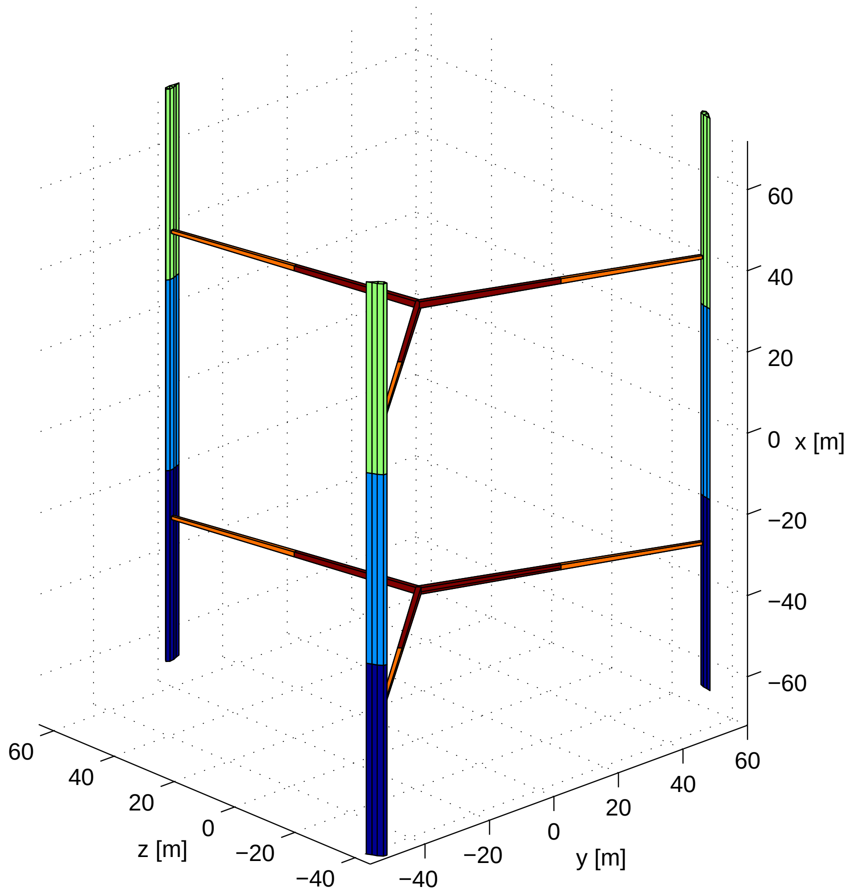

Figure 2.7: 3-bladed H-rotor.

critical failure modes are identified and the internal loads of the structures are decomposed to quantify the contribution of the centrifugal, aerodynamic, and gravitational load to the total. Together, the critical failure modes and decomposed loads show which load is causing which critical failure mode. The failure mode-driving loads give insight on improving the geometry of the rotor designs.

The scope of the design optimization is limited to the rotor subsystem. Furthermore, the assessment of the design in the optimization is limited to the structural analysis of the rotor. The design of two rotor configurations are evaluated: the 3-bladed H-rotor and Darrieus rotor, shown in Figure 2.7 and Figure 2.8. The number of evaluated rotor configurations is restricted to limit the number of optimizations. Therefore, other interesting rotor configurations, such as the V-rotor and helical rotor, are not evaluated.

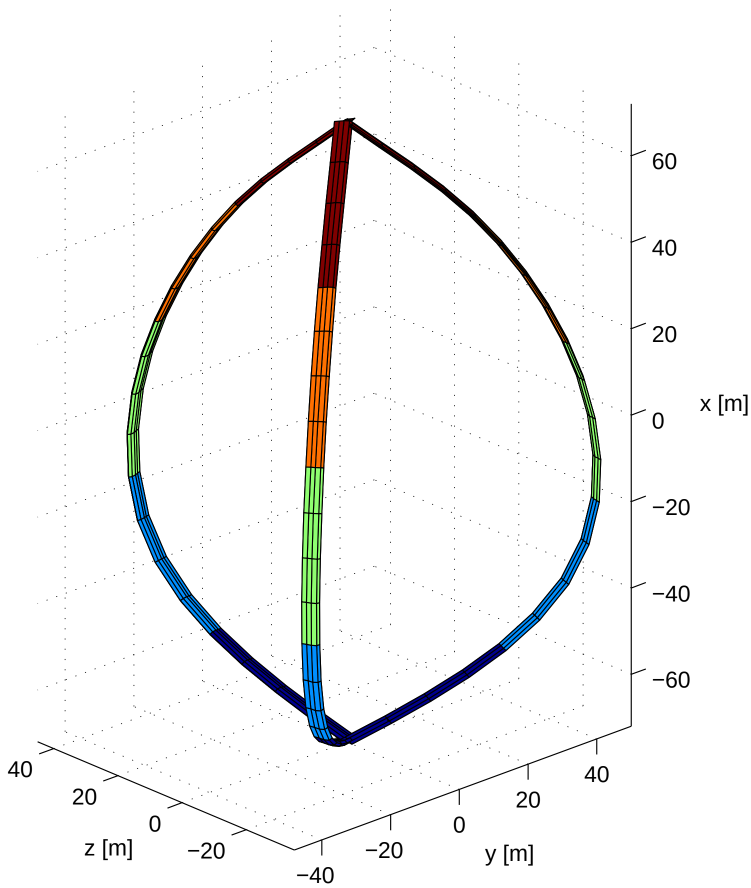

Figure 2.8: 3-bladed Darrieus rotor.

Chapter 3

Structural model for the rotor optimization

This chapter describes the different models, which are applied to the structural optimization of the VAWT rotor. The first section discusses the mathematical representation of the blade and strut geometry, and how the geometry is divided in sections. Subsequently, the structural modeling of the VAWT rotor is discussed, which elaborates on the evaluated loading conditions and failure modes in the optimization, the applied materials, and the finite element model used to analyze the structure. Finally, the application of the aerodynamic loads is covered.

3.1 Mathematical representation of the rotor geometry

For the numerical optimization it is required to convert the design of the structures into a mathematical representation. The mathematical representation uses a set of design parameters to initiate the design. This set of parameters needs to enable the generation of a complete and relevant specification of the model. To offer enough variety of the properties of the structures, a large set of design variables is desired. On the other hand, to reduce the optimization time, it is desired to have a limited number of design variables. The mathematical representation of the geometry should be able to generate the H-rotor and Darrieus rotor configurations, which are illustrated in Figure 2.1.

The mathematical representation is used to generate the FEM formulation of the rotor geometry. The FEM software used in this thesis is MSC Nastran. The geometry is formulated using CQUAD4 elements, which are two dimensional, four-noded elements. The elements are obtained by meshing the geometry.

3.1.1 Blade geometry representation

The work of Ferede et al. [17] discusses a geometry parameterization method for wind turbines blades. This method is enhanced and applied to the optimization framework to

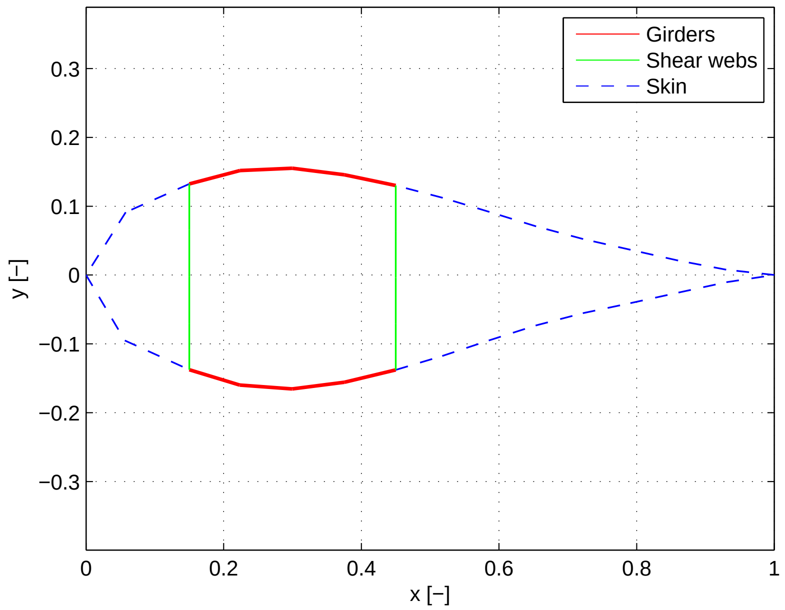

Figure 3.1: Structural members of the discretized cross-section of the blade.

model the blade geometry. It uses Non-Uniform Rational Basis Splines (NURBS) [18]. NURBS are used in computer aided design for generating curves and surfaces. NURBS can generate a large variety of curve and surface shapes, offering the freedom to investigate a large design space.

NURBS use control points to generate these curves and surfaces. The blade is parameterized at these control points in terms of its beam axis, twist, and (weighted) airfoil shape. The beam axis controls the geometrical shape of the blade such as sweep and curvature. The weighted airfoil shapes are products of the airfoil, their fractional contribution to the total shape, and the chord at the control point. The weighted airfoil shapes control the chord and cross-sectional shape distribution along the blade. The code is able to discretize (mesh) the geometry in shell elements, which makes it easy to apply the geometry in a finite element analysis.

The cross-section of the blade is divided in three structural members: the girders, shear webs and skin, as shown in Figure 3.1. The girders are located at the upper and lower surface of the blade, they start at 15% of the chord and end at 45% of the chord. The remaining of the upper and lower surfaces is defined as the skin of the blade. Two shear webs are used in the blade, positioned at 15% and 45% of the chord.

3.1.2 Strut geometry representation

A simple geometry is used for the strut: a tapered beam with a rectangular cross-section. The shape of the cross-section of the strut can be controlled at both ends of the beam by the width and height of the cross-section. This gives a total of 4 strut cross-section parameters, which are varied in the optimization. The beam is linearly meshed for the finite element analysis.

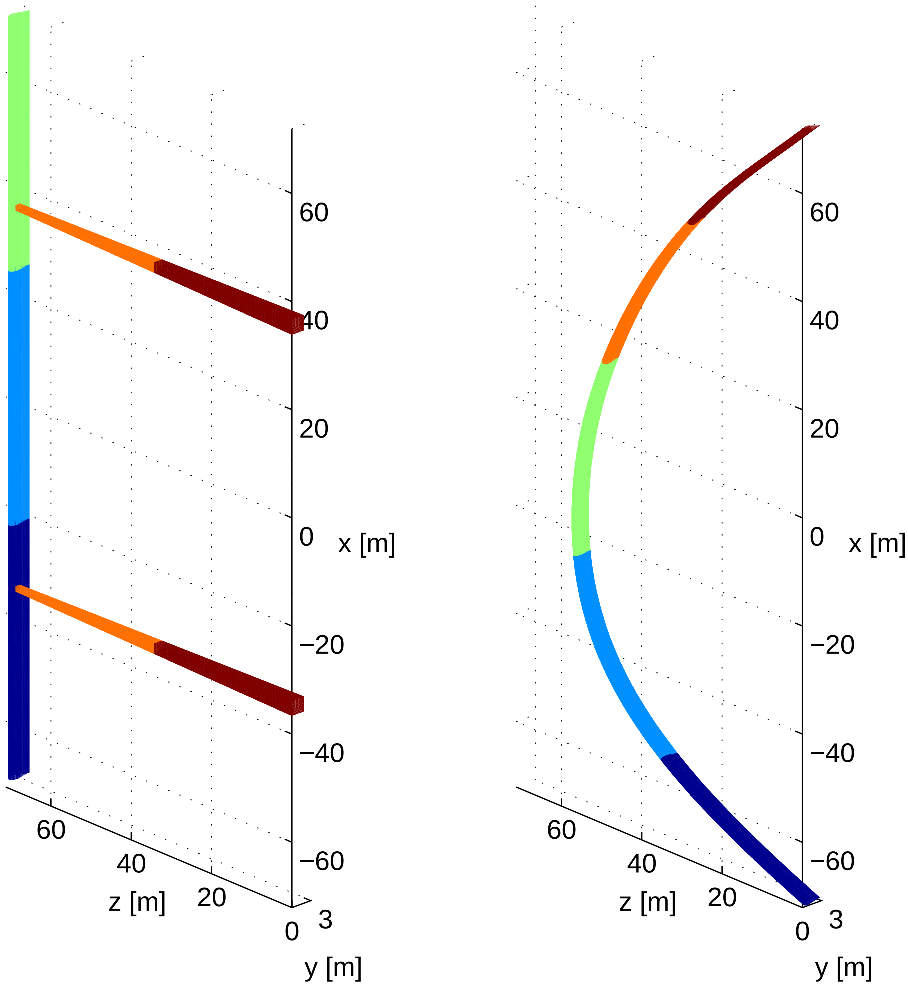

(a) H-rotor.

(b) Darrieus rotor.

Figure 3.2: Section division of the FEM model of the rotors.

3.1.3 Section division of the blade and strut

Discretization points on the blade and strut axis can be allocated, such that they can be used for dividing them in sections. A desired number of sections can be appointed to the structures. Per section the laminate thicknesses of the structural members can be set. For a heavy loaded section the laminate thickness can be increased separate from the rest of the sections. The H-rotor is illustrated in Figure 3.2a with 3 sections along the length of the blade and 2 sections along the length of the struts. The Darrieus rotor is illustrated in Figure 3.2b with 5 sections along the length of the blade.

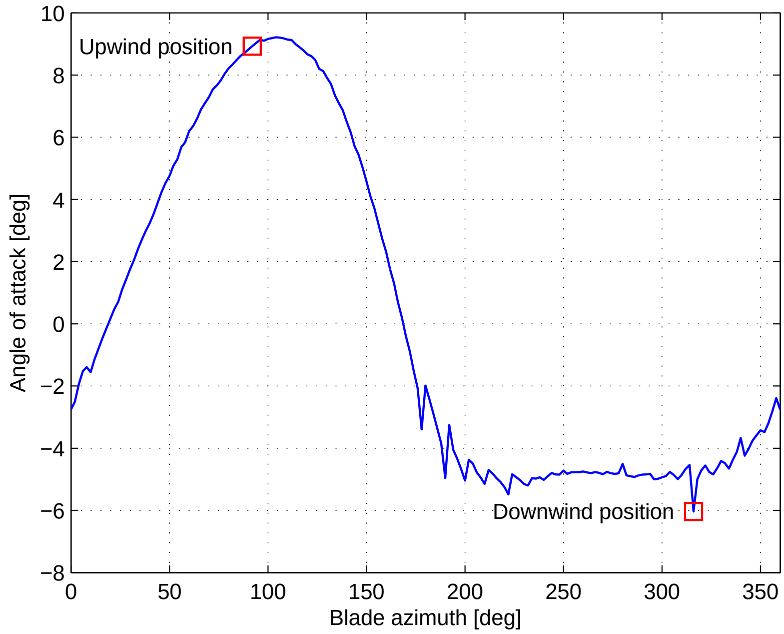

Figure 3.3: Angle of attack seen by the blade during one revolution[a].

[a]Results of an airfoil optimization, received on: 30-10-12 from Carlos Simão Ferreira.

3.2 Evaluated loading conditions and failure modes in the optimization

The considered load conditions for the optimization are limited to realize a reasonable optimization time. Only the normal operation condition in upwind and downwind position (see Figure 3.3) and parked condition are considered. In Table 3.1 the assumed conditions in normal operation are stated. The structural analysis accounts for gravitational, centrifugal, and aerodynamic loads. The applied safety factors (SF) are taken from the work of Ashuri [16], see Table 3.2.

The structure is analyzed for ultimate strength and (ultimate) buckling for both loading conditions. The fatigue analysis accounts only for the upwind and downwind normal operation load conditions at rated wind speed. The turbine is designed for a 20 year life time, in which it is in operation at rated wind speed 35% of its life. The rotational speed of the turbine depends on the rotor shape, since the tip speed ratio (TSR) is kept constant. The product of the time in operation and the rotational speed yields the number of rotations the turbine needs to withstand in its life. It is assumed no aerodynamic and centrifugal load is acting on the rotor in parked condition.

The resulting designs of the combined optimizations are used to assess fatigue more thoroughly, using more azimuthal blade positions to determine the variation of the load per revolution more exactly. Furthermore, it became clear from the literature study that resonance is an important design driver for VAWT's. Therefore, the undamped, free vibration modes of the rotors and the minimum emergency stop braking time are evaluated. The latter results are used to assess the feasibility of these designs.

Table 3.1: Normal operation conditions.

Parameter	Value
Rated wind speed	12 [m/s]
Tip speed ratio	4.5 [-]

Table 3.2: Safety factors.

Load case	Value
Ultimate	1.5
Fatigue	1.265
Limit	1

3.3 Strength analysis of the carbon-fiber laminates

The mass increase of the blades is identified as a limiting factor for upscaling wind turbines. The use of carbon-fiber laminates in the blade design is considered as a good design solution to reduce mass and allow further upscaling. Therefore, the focus is put on CFRP laminates in the optimization. The material properties of a CFRP ply are stated in Table 3.3. Multiple laminates are build, tailored for the application of the laminate, see Table 3.4. Classical laminate theory is used to determine the ABD-matrices of the laminates. The first-ply-failure (Tsai-Hill) criterion [19] is applied to determine the allowable load magnitude, when the load is applied in a single in-plane normal or shear direction. The corresponding strains are used to assess failure separately per loading direction. The strains are translated to an averaged stress along the laminate thickness, neglecting variation of material properties along the thickness of the laminate. The allowable stresses are stated in Table 3.5. Material property matrices (modified A & D matrices, see Equation 3.1) of the laminates are fed into the FEM model. Thus, the FEM analysis does not explicitly take the laminate layup into account, but uses the membrane and bending stiffness averaged along the laminate thickness.

$$\begin{aligned} \mathbf{A}_{CLT,mod} &= \frac{\mathbf{A}_{CLT}}{t} \\ \mathbf{D}_{CLT,mod} &= \frac{12 \cdot \mathbf{D}_{CLT}}{t^3} \end{aligned} \tag{3.1}$$

The fatigue life of a $[45/90/\text{-}45/0]_s$ CFRP laminate was studied by Poursartip et al. [20]. An expression for the allowable number of cycles for a certain cyclic loading is provided in their paper, stated in Equation 3.2. For p, a value of 1.6 is used (for high stress ratios).

$$N_{all} = 3.108 \cdot 10^4 \cdot \left(\frac{\Delta\sigma}{\sigma_{all}}\right)^{-6.393} \cdot \left(1.222 \cdot \frac{1 - R_\sigma}{1 + R_\sigma}\right)^p \cdot \left(1 - \frac{\Delta\sigma}{(1 - R_\sigma) \cdot \sigma_{all}}\right) \tag{3.2}$$

Where R_σ is the stress ratio:

$$R_\sigma = \frac{\sigma_{min}}{\sigma_{max}} \tag{3.3}$$

Table 3.3: Material properties.

	Standard carbon-fiber UD
E_{xx} [GPa]	135
E_{yy} [GPa]	10
G_{xy} [GPa]	5
v_{xy} [-]	0.3
ρ [kg/m^3]	1600
X_t [MPa]	1500
X_c [MPa]	1200
Y_t [MPa]	50
Y_c [MPa]	250
S [MPa]	70

Table 3.4: Laminates per structural member.

Application	**Layup of laminate [deg]**	**Thickness fraction of core [-]**
Skin	$[0_2/90/(45/\text{-}45)_2]_s$	0.65
Shear web	$[0/(45/\text{-}45)_2/90/45/\text{-}45]_s$	0.65
Girder	$[0_6/45/\text{-}45]_s$	-
Strut	$[0_6/45/\text{-}45]_s$	0.65

Table 3.5: Allowable stresses of laminates.

Material	**Laminate**	X_t **[MPa]**	X_c **[MPa]**	Y_t **[MPa]**	Y_c **[MPa]**	S **[MPa]**
CRFP	Skin	308	485	218	361	244
	Shear web	208	313	208	313	304
	Girder & Strut	840	848	88	181	138

The latter expression for the S-N curve can be used in combination with rainflow counting and the Miner's rule to assess failure due to fatigue for multiple, different load cycles, see Equation 3.4. Failure occurs when D_{MR} is equal to or larger than 1.

$$D_{MR} = \sum_i \frac{n_i}{N_{all,i}} \tag{3.4}$$

3.4 Finite element method formulation of the geometry

The FEM models of the rotors are build out of shell elements. The first part of this section discusses how the boundary conditions are applied to the model. The second part argues the choice for the mesh densities applied to the FEM models.

3.4.1 Boundary conditions and connections

The Darrieus design does not include strut-blade connections, therefore its FEM model is less complex. The connections of both ends of the blade to the tower are modeled by clamps, which yield zero degrees of freedom of the nodes in the cross-sections of the blade ends.

The model of the H-rotor is more complex. The blades are connected to the tower via the struts. The connection of the strut to the tower is modeled by clamps. The blade-strut connection is modeled with the use of rigid body elements. The nodes connected by the rigid body element can not move relative to each other, only as a whole. A rigid body element is used to connect the nodes in the tip cross-section of the strut with the nodes of the girders and shear webs of the blade at the strut position, see Figure 3.4b. Furthermore, each blade tip uses a rigid body element such that the cross-section at the tip retains its shape.

The blade elements adjacent to the strut-blade connection are prone to singularities. Therefore, on both sides of the rigid body element, three spanwise strips of elements are disregarded in the ultimate and fatigue load case. These elements are illustrated in green in Figure 3.4a.

3.4.2 Mesh convergence

The convergence of the strain energy of the FEM model is analyzed to determine how dense the mesh of the FEM model needs to be. To increase the accuracy of the solution of the FEM problem, the mesh density of the model should be increased. An increase in mesh density comes at the cost of an increase in the run time of the solver. A trade-off is performed to attain sufficient accuracy of the solution for a reasonable optimization time. The accuracy of the FEM solution is tested by extracting the total strain energy of the solution for different mesh densities. In the FEM analysis the blades and strut are loaded by gravitational and centrifugal loads.

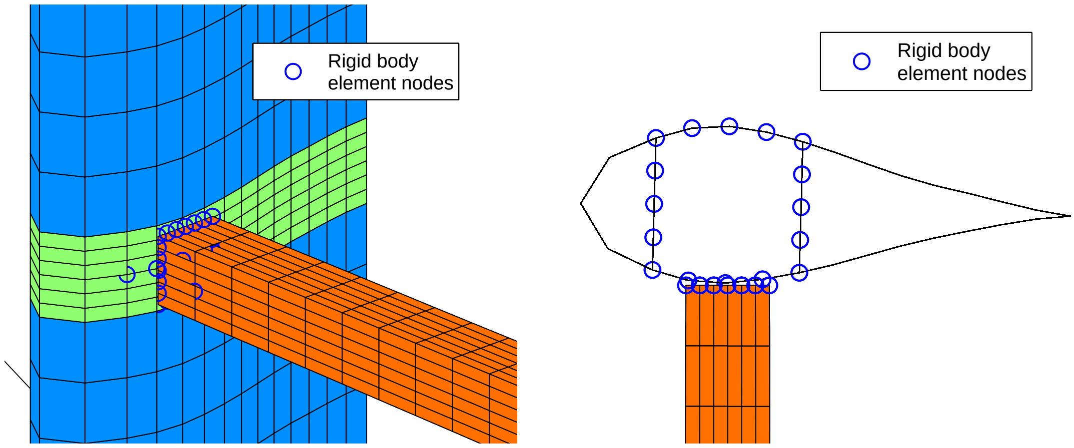

(a) Strips of elements disregarded from ultimate and fatigue load case.

(b) Nodes used for rigid body element of the blade-strut connection.

Figure 3.4: Modeling of the blade-strut connection.

Next to an accurate strain energy, the mesh density should allow for an accurate analysis of the buckling modes. In the work of Arden [21] the accuracy of MSC Nastran in determining the linear elastic buckling modes is investigated. Arden concludes that local, panel buckling can be accurately predicted using a minimum of four shell elements (QUAD4 elements) per half sine wave of the buckling mode. Furthermore, Arden states that the number of shell elements used in the secondary buckling mode direction are less important. Similar to the strain energy convergence, the accuracy of the FEM solution for the buckling modes is tested by extracting the eigenvalue of the first eigenmode for different mesh densities.

The mesh of the blade can be set by the number of elements along the x-direction (along the length) and y-direction (along the chord). The mesh ratio is defined as the ratio between the number of elements in x- & y-direction. The element side length ratio is defined as the ratio between the element side length along the blade or strut and along the cross-section. A mesh ratio is selected, which yields a maximum side length ratio smaller than 2.5 and 4.5 for respectively the square blade and strut elements. The mesh convergence of the strain energy and the buckling analysis are checked by keeping the mesh ratio constant, but varying the density. For these convergence analyses the number of elements in both directions are multiplied with a common factor.

Plots of the convergence of the strain energy and the buckling eigenvalue are generated for the Darrieus rotor blade, H-rotor blade, and strut. In these convergence plots the total number of elements are put on the horizontal axis. A power curve is fitted to the data for the different mesh densities, outputted by MSC Nastran. The value for the 'exact' solutions is determined by running the analysis with a very fine mesh, using approximately 750,000 and 290,000 elements for the blades and strut respectively. This value is used as a reference values in determining the absolute error of the raw data. The reference value is also used to normalize the absolute error. A power curve is fitted to the raw, normalized absolute error data. The mesh density is said to be acceptable for the region where the fitted curve of the strain energy error is underneath 5%. No criterion is set regarding the convergence of the buckling analysis.

Mesh density Darrieus rotor blade

Figure 3.5b shows that the error of the strain energy is around 3.5% for the full range of the total number of elements in the model. The selected mesh has 15 elements along the chord of the blade and 310 elements along the length of the blade, yielding a total of 11,160 elements. A static analysis with this mesh density takes around 45 seconds, see Figure 3.5c. Figure 3.5e shows the error of the buckling analysis is larger than 5% for almost the full range of the total number of elements. A buckling analysis for a total of 11,160 elements takes around 1 minute, see Figure 3.5f.

The mesh ratio 310 over 15 elements in respectively the x- and y-direction yields:

- A mean element length along the length of the blade of 0.63 meter.
- A mean element length along the cross-section of 0.29 meter.
- A mean ratio of the element length in x- and y-direction of 2.22.
- A maximum ratio of the element length in x- and y-direction of 2.50.

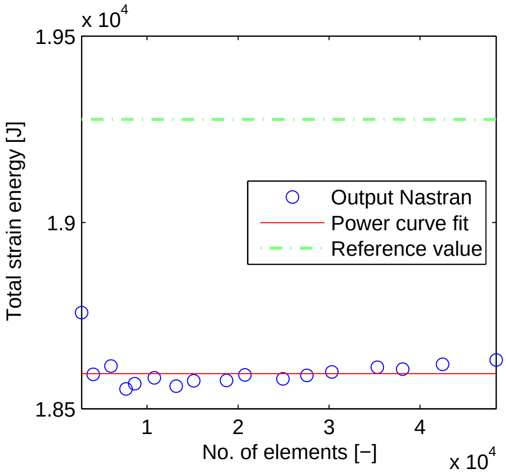

(a) Strain energy.

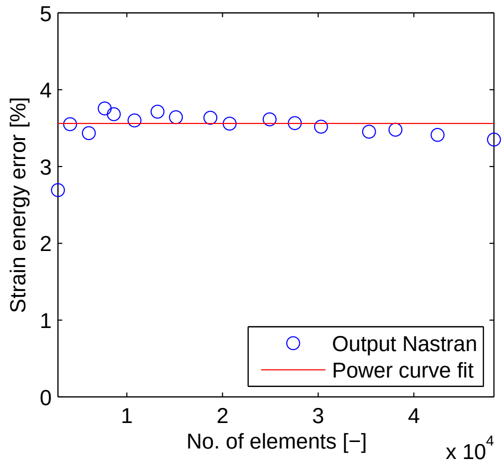

(b) Error of the strain energy.

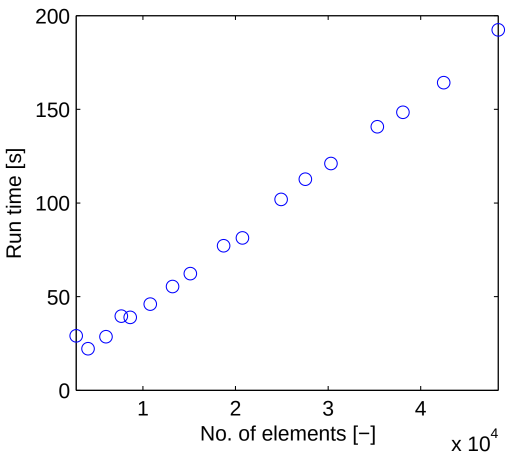

(c) CPU time of the static analysis.

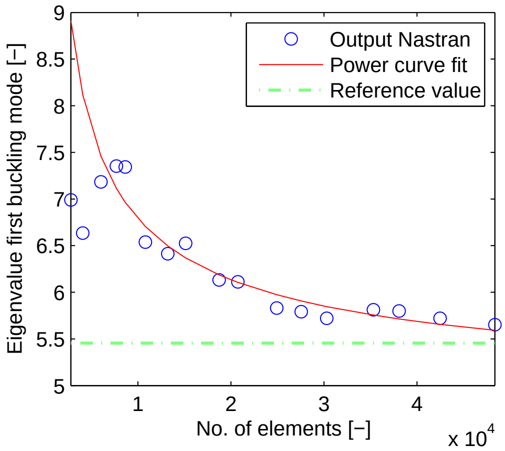

(d) First buckling mode.

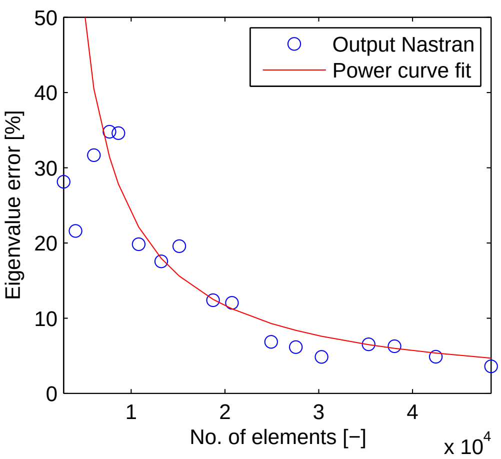

(e) Error of the first buckling mode.

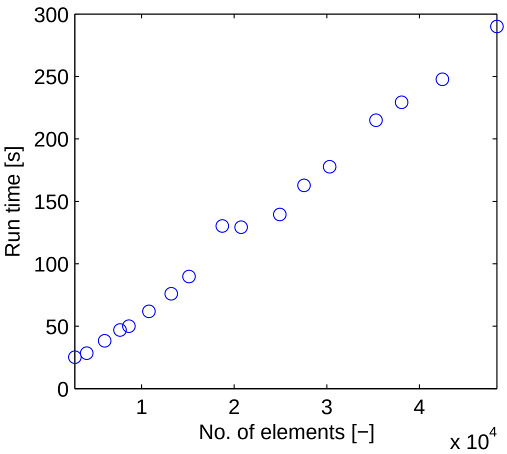

(f) CPU time of the buckling analysis.

Figure 3.5: Mesh convergence of the Darrieus rotor blade strain energy and first buckling mode.

Mesh density H-rotor blade

Figure 3.6b shows that the error of the strain energy is below 1% for the full range of the total number of elements in the model. The selected mesh has 15 elements along the chord of the blade and 200 elements along the length of the blade, yielding a total of 7488 elements. Figure 3.6d shows the error of the buckling analysis is still around 10% for 20,000 elements.

The mesh ratio 200 over 15 elements in respectively the x- and y-direction yields:

- A mean element length along the length of the blade of 0.68 meter.
- A mean element length along the cross-section of 0.35 meter.
- A mean ratio of the element length in x- and y-direction of 1.95.
- A maximum ratio of the element length in x- and y-direction of 2.32.

Mesh density strut

Figure 3.7b shows that the error of the strain energy is zero for the full range of the total number of elements in the model. The selected mesh has 6 elements along one side of the cross-section and 120 elements along the length of the blade, yielding a total of 2880 elements per strut. Figure 3.7d shows the error of the buckling analysis remains below 5% for more than 1800 elements, with the exception of one outlier point.

The mesh ratio 310 over 15 elements in respectively the x- and y-direction yields:

- A mean element length along the length of the strut of 0.60 meter.
- A mean element length along the cross-section of 0.18 meter.
- A mean ratio of the element length in x- and y-direction of 3.36.
- A maximum ratio of the element length in x- and y-direction of 4.46.

3.5 Application of the aerodynamic loads on the blade

A constant, chordwise pressure coefficient distribution is assumed along the blade. The results of a 2D unsteady panel model simulation in a potential flow[1] are used to determine the aerodynamic blade loads. The simulation uses a 32% thick airfoil, shown in Figure 3.8. The angles of attack seen by the blade in one revolution are shown in Figure 3.3. The work of Simao Ferreira [22] states that blade-wake interaction occurs in the windward, downwind, and leeward sections of the blade rotation. This interaction results in fluctuations in the angle of attack at these rotation sections. The normal and tangential force coefficient are also provided, see respectively Figure 3.9 and Figure 3.10. The

[1] Results of an airfoil optimization, received on: 30-10-12 from Carlos Simão Ferreira.

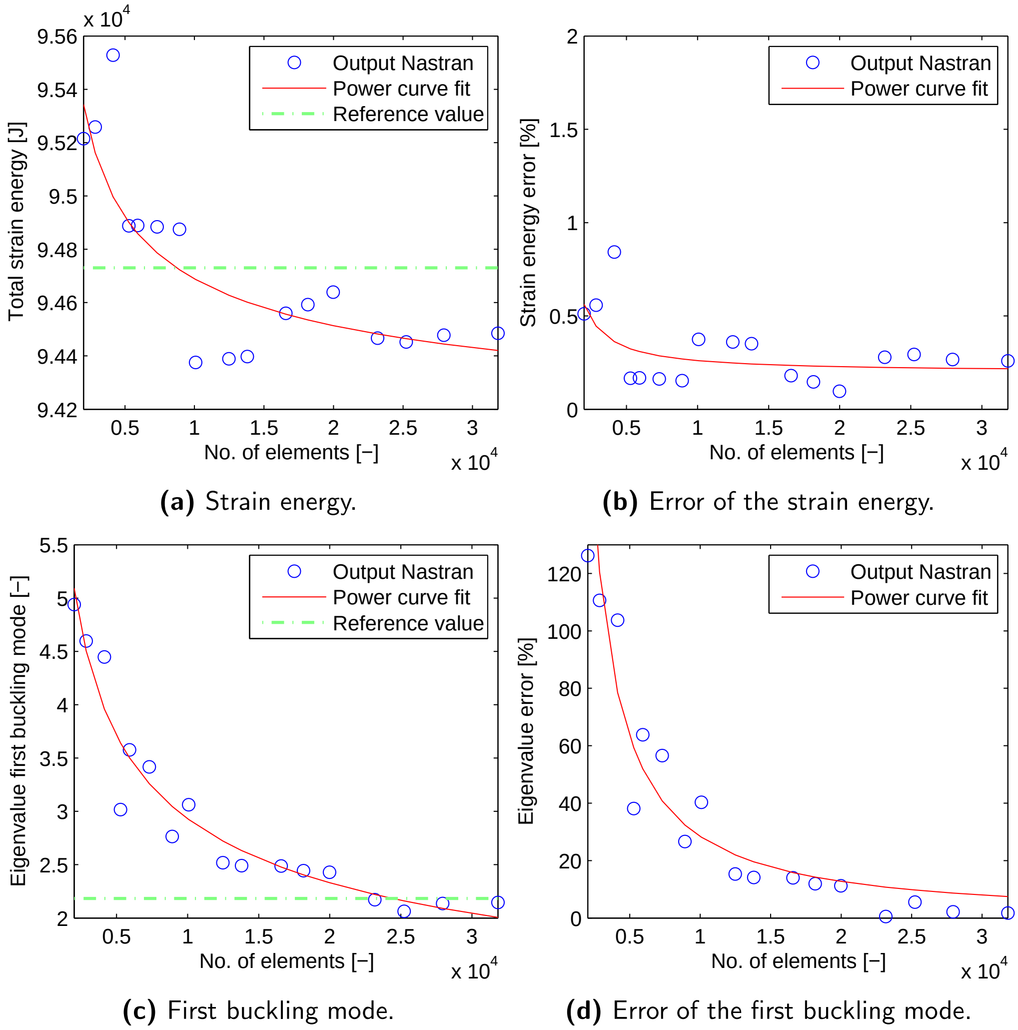

Figure 3.6: Mesh convergence of the H-rotor blade strain energy and first buckling mode.

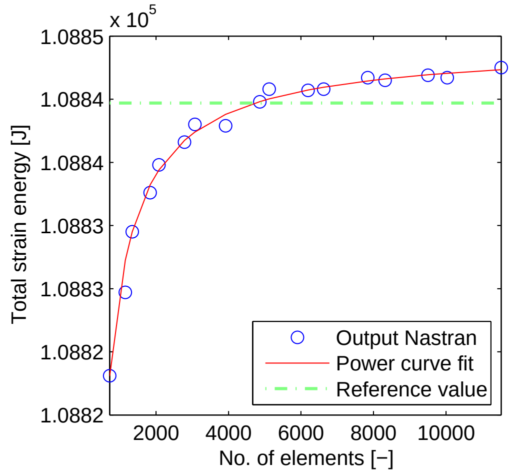

(a) Strain energy.

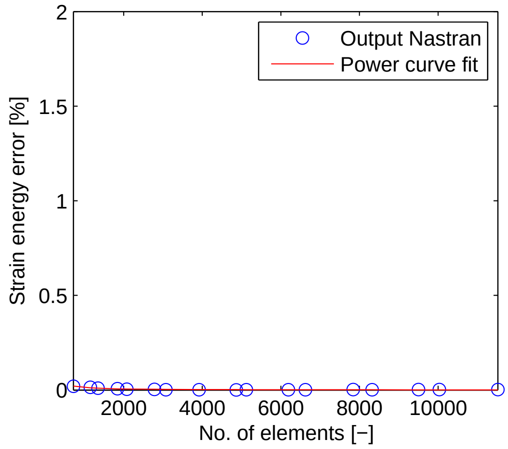

(b) Error of the strain energy.

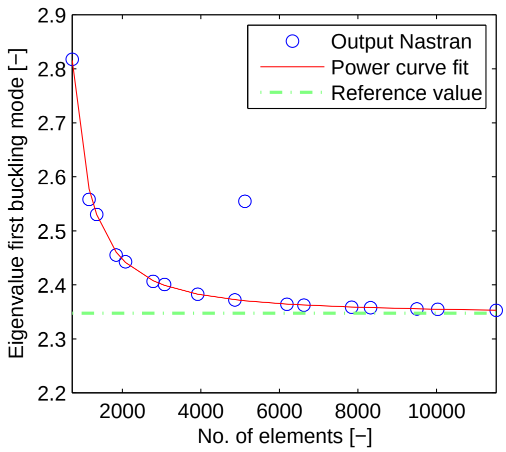

(c) First buckling mode.

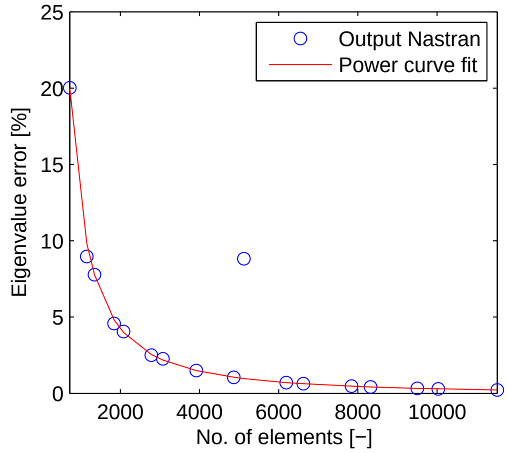

(d) Error of the first buckling mode.

Figure 3.7: Mesh convergence of the H-rotor strut strain energy and first buckling mode.

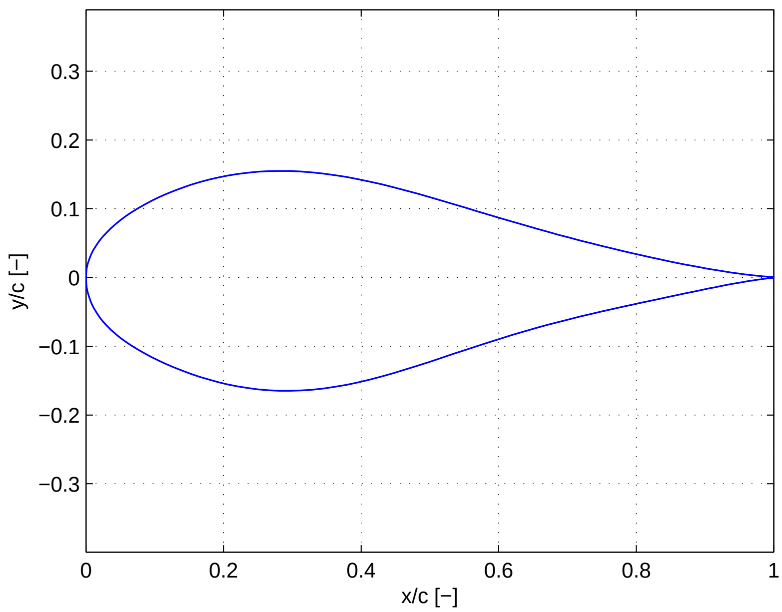

Figure 3.8: 32% thick airfoil used in the optimization.

provided angles of attack are used in XFOIL to obtain pressure coefficient distributions for different azimuthal blade positions. The air velocity perceived by a blade element is simplified to be a summation of the wind speed and the rotational speed. The pressure coefficient distribution together with the air velocity yields the aerodynamic load applied to the blade. The aerodynamic load is applied in the FEM model by linear pressure distributions normal to the elements, based on the pressure at the element corners. The pressure at the element corners are based on the pressure coefficient at the corresponding node locations, extracted from the pressure coefficient distributions.

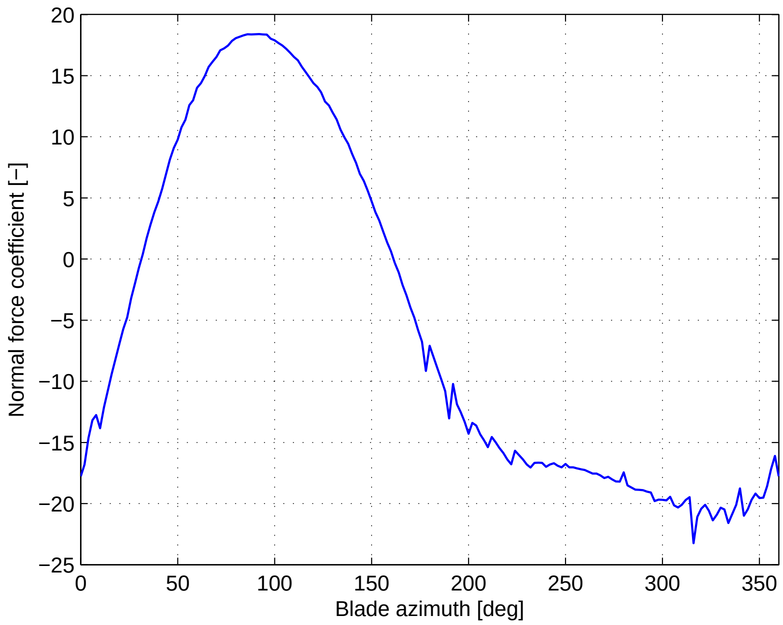

Figure 3.9: Normal aerodynamic force coefficient during one blade revolution.

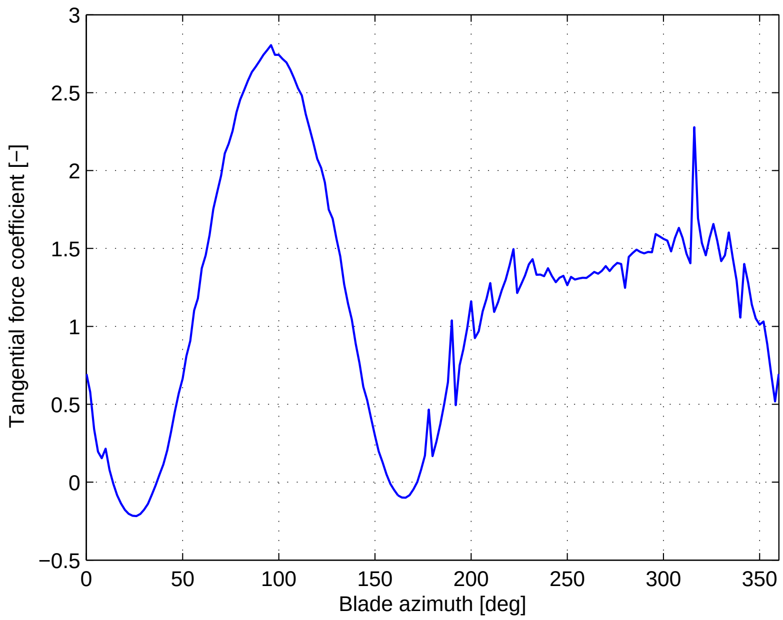

Figure 3.10: Tangential aerodynamic force coefficient during one blade revolution.

Chapter 4

Rotor optimization approach

This chapter starts with some practical considerations on the optimization. First, the optimization code is discussed together with the applied optimization algorithm. Subsequently a distinction is made between the different optimization types. The objective function, constraints, and design variables of the optimization are addressed. The objective function and constraints are the same for all the optimization types. The main difference between the optimization types is in the composition of the design vector.

4.1 Optimization algorithms

The optimization is conducted by Matlab. Each evaluation of the optimization Matlab calls the FEM solver: MSC Nastran. A flow diagram of the optimization is given in Figure 4.1. The pre-processor generates the FEM formulation of the rotor structure in the form of an input file for MSC Nastran. MSC Nastran is called multiple times to determine the stresses and buckling modes for the different loading conditions. The output of MSC Nastran is read by the post-processor. The raw output needs to be processed into optimization constraints, which are used by the optimizer to come to a feasible rotor design. In Appendix B the flow diagram of the optimization is further explained.

Matlab offers multiple readily available functions for optimization. For this thesis the *fmincon* function is used. The *fmincon* function enables finding a minimum of a constrained nonlinear multi-variable function using gradient-based algorithms. Matlab also provides genetic optimization algorithms, the use of these algorithms is out of the scope of this thesis. Genetic algorithms are more tolerant when it comes to noise in the optimization problem [23]. Genetic algorithms were not implemented for this thesis, since in general they take more time to converge to a solution.

The *fmincon* function can be used in combination with several gradient based optimization algorithms. The sequential quadratic programming (SQP) algorithm is selected. This algorithm combines the objective and constraint functions into a merit function, which is minimized. The SQP algorithm determines the gradients of the merit function by performing a sensitivity analysis. To do so, small steps are taken relative to its current point. The minimum step size taken by the algorithm can be set in the options of the *fmincon* function by changing the value for DiffMinChange. This is especially important when performing the optimization using MSC Nastran. The values inputted in MSC Nastran only contain 8 characters. This requires rounding the values provided by the optimizer. If DiffMinChange is set too small, the input for MSC Nastran will not experience any change and therefore the output will not change. In this case the gradient determined by the optimizer will be zero, and it will be impossible to determine for which direction in the design space the merit function value will decrease.

For the optimization, the initial design vector is preferably chosen such that it yields a feasible solution (no constraint violation). Furthermore, the closer the initial design vector to the optimal solution, the more likely it is to decrease the convergence time. Both the design vector and the objective function are normalized by their starting value, such that all the values start at 1. Having an equivalent order of magnitude for all the design variables helps the optimizer to converge.

4.2 Distinction between the optimization types

The mathematical geometry representation specifies the properties stated in Table 4.1, using a confined set of parameters. To restrict the optimization time it is important to vary only a limited number of these parameters: the design variables. The rotor design parameters are categorized using the definitions of types of design variables for structural optimization stated in the work of Choi et al. [24]. Choi makes a distinction between the five types of design variables listed below. The non-structural parameter, the tip speed ratio, is categorized as an operational design variable.

- Material property design variable: in most design problems the applied materials are predefined and thus the material properties are frozen. For some design problems it is desired to vary material properties, such as the properties stated in Table 3.3.
- Sizing design variable: sizing parameters do not change the global geometry of the structure. The most important sizing parameters are structural member thicknesses and parameters defining the cross-section geometry.
- Shape design variable: shape parameters do change the global geometry of the structure and thereby determine the structural domain. An example of a shape parameter is the length of a beam.
- Configuration design variable: configuration parameters determine the orientation of structural components.
- Topology design variable: topology parameters determine the layout of a structure and can control the birth or death of structural components. Material property parameters can be used for the purpose of topology parameters. Letting the Young's modulus approach zero on a part of the structural domain is equivalent to omitting that part of the structural domain in the analysis.

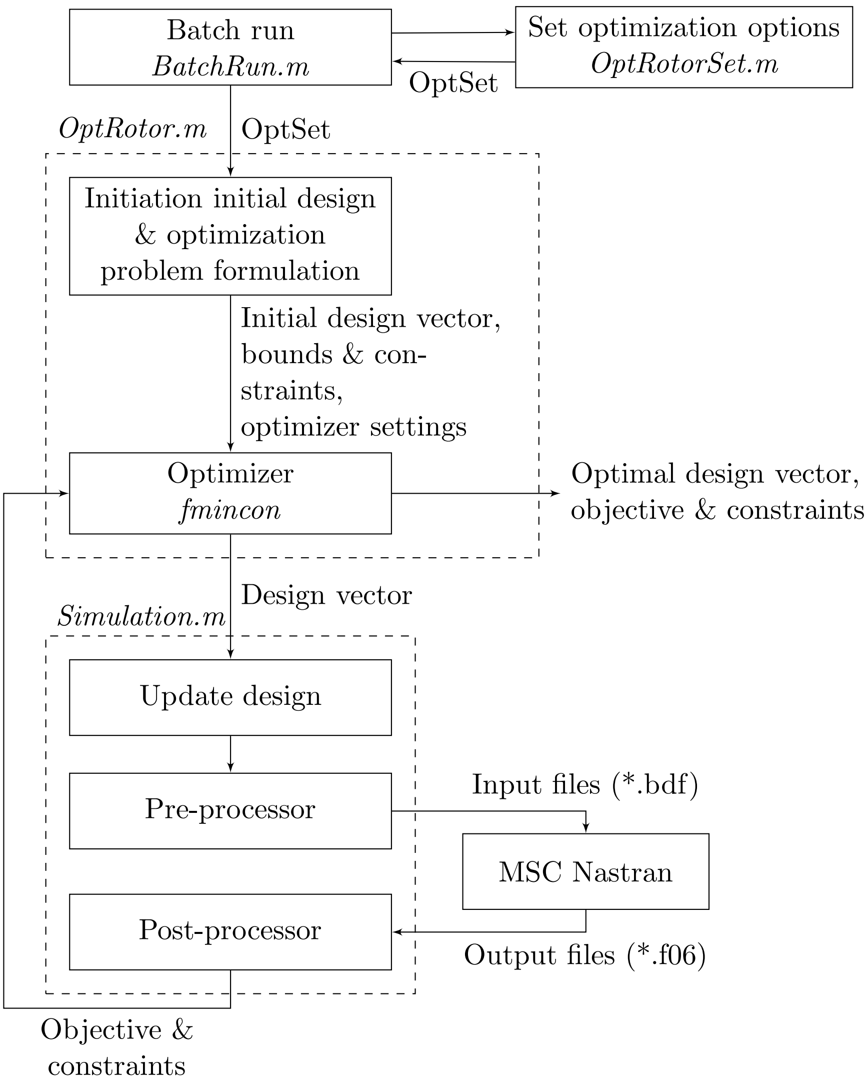

Figure 4.1: Optimization flow diagram.

The focus for this thesis is put on optimizing the structural sizing and rotor shape parameters. Only continuous design variables are used in the optimization. The only discontinuous design parameters in Table 4.1 are the topology parameters. The topology parameters will not be varied within an optimization.

Table 4.1: Design properties optimization.

Category	**Property**	**Variable type**	**No. of design vars sizing optimization**		**No. of design vars shape optimization**	
			H-rotor	**D-rotor**	**H-rotor**	**D-rotor**
Operation	Tip speed ratio	operation	frozen	frozen	frozen	frozen
Rotor	Number of blades	topology	frozen	frozen	frozen	frozen
	Rotor height	shape	frozen	frozen	frozen	frozen
	Rotor radius/blade curvature	shape	frozen	frozen	1	7
	Number of struts	topology	frozen	frozen	frozen	frozen
	Strut locations	shape	frozen	frozen	2	-
Blade	Airfoils	shape	frozen	frozen	frozen	frozen
	Number of spars	topology	frozen	frozen	frozen	frozen
	Spar locations	shape	frozen	frozen	frozen	frozen
	Chord distribution	shape	frozen	frozen	0	0
	Twist distribution	shape	frozen	frozen	frozen	frozen
	Internal dimensions	sizing	15	15	frozen	frozen
	Material properties	material	frozen	frozen	frozen	frozen
Strut	cross-section geometry	sizing	4	-	frozen	-
	Internal dimensions	sizing	4	-	frozen	-
	Material properties	material	frozen	frozen	frozen	frozen

4.3 Optimization objective function

All the optimizations serve the same goal: minimizing cost of the rotor, while maximizing the energy yield of the turbine. The cost of structures is often expressed as a linear function of the mass of a structure in upscaling methods using scaling laws. In practice, amongst others, the complexity of a structure and the applied materials are an important factor driving the cost of a structure. For this thesis, it is assumed that the cost of the rotor is a linear function of the mass of the rotor; an increase in mass increases the costs.

The expression for annual energy yield of a turbine E, is given in Equation 4.1, where T_{oper} is the total number of hours per year for which the turbine is in operation, P is the power output of the turbine, f_V is the wind speed probability, and V_{ci} and V_{co} are respectively the cut in and cut out wind speeds. Of all of the latter parameters, the shape of the rotor only influences the power output of the turbine.

$$E = T_{oper} \cdot \int_{V_{ci}}^{V_{co}} P(V) \cdot f_V(V) dV \tag{4.1}$$

The expression for the power output of a turbine is stated in Equation 4.2. The power capacity of the rotor P, is a linear function of the rotor area. In the latter equation ρ is the air density, V is the wind speed, C_p is the power coefficient, and A is the projected rotor area. The shape of the rotor will only influence the power coefficient and the projected rotor area. For this thesis it is assumed the power coefficient does not change significantly by keeping the tip speed ratio and blade solidity (the blade chord over rotor radius ratio) constant, discussed in Section 4.3.1. A constant power coefficient of 0.43, a rated wind speed of 12 m/s, a tip speed ratio of 4.5, and a blade solidity of 0.067 is assumed. The only remaining parameter which does change significantly is thus the projected rotor area, which needs to be maximized to maximize energy yield of the turbine. Notice that the shape of the rotor also influences the mass of the rotor.

$$P = \frac{1}{2} \cdot \rho \cdot V^3 \cdot C_p \cdot A \tag{4.2}$$

The cost of the rotor and the energy yield of the turbine are thus assumed to be a linear function of respectively the rotor mass and the projected rotor area. Therefore, minimizing the cost of the rotor, while maximizing the energy yield of the turbine is equivalent to minimizing the rotor mass over projected area ratio. For this thesis, the structural rotor performance is assessed by the value for this ratio.

4.3.1 Constant power coefficient for different H-rotor shapes

In this section the optimization condition is determined for a constant power coefficient, using simple derivations. The derivations are focused on the H-rotor geometry. Consider the top view of an 1-bladed VAWT H-rotor in Figure 4.2. The power generated by this single blade at a certain azimuthal angle is the product of the generated torque and the angular speed of the blade. The torque generated by the blade is the product of the local radius and the 2D tangential force on the airfoil, integrated along the length of the blade, see Equation 4.3.

In the optimization, the aim is to keep the power over projected rotor area ratio constant. A constant power over projected rotor area ratio is equivalent to a constant power coefficient, see Equation 4.4. The projected rotor area of the H-rotor is the product of the height and the diameter of the rotor. The relation for the projected rotor area and the relation for the power from Equation 4.3 are substituted in Equation 4.4. The radius and the height of the rotor appear in both the numerator and denominator and cancel each other out. The power over projected rotor area ratio is thus only a function of the 2D tangential force of the airfoil and the angular speed of the rotor.

$$\begin{aligned} P = \frac{1}{2}\rho V_\infty^3 \cdot C_P \cdot A \quad &= T \cdot \Omega \\ &= \int_0^H F_t \cdot R \, \mathrm{d}s \cdot \Omega \\ &= F_t \cdot H \cdot R \cdot \Omega \end{aligned} \tag{4.3}$$

$$\frac{P}{A} = \frac{1}{2}\rho V_\infty^3 \cdot C_P = \frac{1}{2} \cdot F_t \cdot \Omega \tag{4.4}$$

The 2D tangential force is a function of the dynamic pressure at the airfoil, the tangential force coefficient, and the chord, see Equation 4.5. In the expression for the dynamic pressure, the perceived air velocity by the blade is determined by the vector summation of the tip speed and the wind speed at the rotor, see Figure 4.3. During the optimization, the tip speed ratio (see Equation 4.6) is kept constant. Keeping the tip speed ratio constant for a given wind speed is equivalent to keeping the tip speed constant. The wind speed at the rotor is also constant, since the induction by the rotor is assumed to be constant (due to the constant power coefficient). The angles of attack seen by the blade are not changing during the optimization, because of the constant tip speed and wind speed at the rotor. The tangential force coefficient is only a function of the angle of attack and will not change either.

$$F_t = \frac{1}{2}\rho V_{per}^2 \cdot C_t(\alpha) \cdot c \overset{\text{for const } \lambda}{\Longrightarrow} F_t = f\left(c\right) \tag{4.5}$$

$$\lambda = \frac{\Omega \cdot R}{V_\infty} \overset{\text{for const } \lambda}{\Longrightarrow} \Omega = f\left(\frac{1}{R}\right) \tag{4.6}$$

The 2D tangential force remains only a function of the chord of the blade. For a constant tip speed ratio and a given wind speed, it is deduced from rewriting Equation 4.6 that the angular speed of the blade is solely a function of the reciprocal of the rotor radius. From Equation 4.4, it is concluded that the power over projected rotor area ratio is a function of the blade chord over rotor radius ratio for a constant tip speed ratio. Thus, to keep the power over projected rotor area ratio constant during the optimization, the blade solidity (chord over rotor radius ratio) needs to be kept constant.

It is assumed that the power over projected rotor area ratio also remains constant for the Darrieus rotor optimization, by imposing the same conditions as for the H-rotor optimization (constant tip speed ratio and blade solidity). Furthermore, it is assumed that the magnitude of the power coefficient of the Darrieus rotor is comparable to the power coefficient of the H-rotor. The latter assumptions justify comparing the power output between both rotors by comparing their projected rotor area.

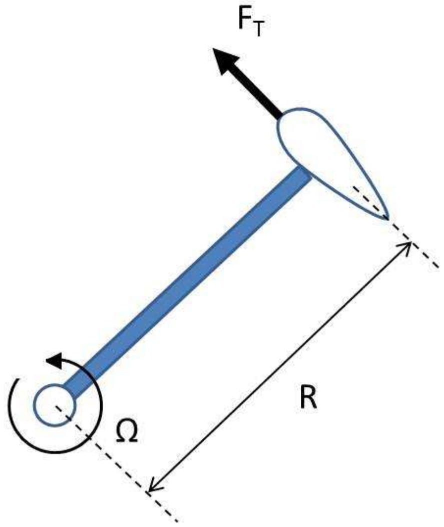

Figure 4.2: Tangential force acting on the blade.

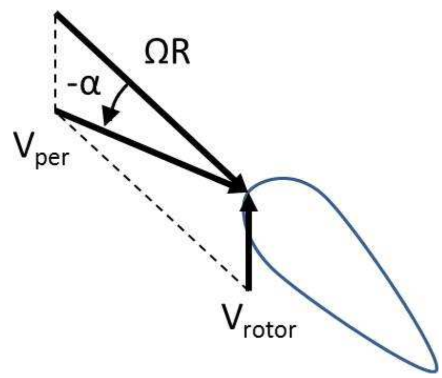

Figure 4.3: Air velocities perceived by the blade.

4.4 Design variables of the optimization

The definition of the design space is the set of possible designs. The design space is determined by the design vector. The design vector contains all the design parameters which are allowed to be varied during the optimization. Table 4.1 shows which properties are varied and which are frozen in the sizing optimization and shape optimization. Furthermore, the table states how many variables are used for the property specification of both rotor configurations. The blade chord distribution is not directly specified by any design variables. However, the chord length is varied in the shape optimization, since it is set by the blade solidity. Therefore, the table makes a distinction between frozen design properties and properties which are varied indirectly by the design variables.

The sizing variables of the blade consist of its laminate thicknesses. In general the blade is divided into 5 sections, for each of these sections the thicknesses of the three structural members are varied. This yields a total of 15 blade sizing variables. For the strut, a thin-walled rectangular cross-section is used. The thin-walled sides of the cross-section have the same thickness per section. In general the strut is divided in 4 equal sections along the length, which yields 4 variable thicknesses. The cross-section geometry is also varied for the strut. The height and width of the cross-section can be varied at both ends of the strut, yielding a total of 8 strut sizing variables.

For the H-rotor, the rotor radius and the individual strut locations are varied in the shape optimization, see Figure 4.4. This yields a total of 3 shape variables for a rotor with 2 struts. For the Darrieus rotor, the blade curvature is controlled by means of NURBS control points. To do so, 9 control points are used, for 7 of the control points the radial position is varied. The upper and lower control points are frozen, such that the blades are connected to the tower axis. The control points and the corresponding beam axis of the blade are illustrated in Figure 4.4. Variation of the blade spar locations is not considered in the optimization, neither is variation of the twist distribution. The blade uses a constant chord distribution, the chord length of the blade is determined by the blade solidity.

For the combined optimization, the design vector consists of both the sizing design variables and the shape design variables. The number of variables used in the combined optimization is determined by summing up the number of variables for the sizing and shape optimizations in Table 4.1.

4.5 Non-linear design constraints of the optimization

To ensure that the optimization yields a feasible solution, the optimization needs to be constrained. As stated before the focus in the optimization is put on the structural analysis. The rotor is only checked for failure requirements on the structure. The loading conditions and failure modes for which failure is assessed are stated in Chapter 3.2. An infeasible solution would be a rotor design which, for example, fails due to fatigue. This section discusses how the constraints are formulated.

The occurrence of failure is identified with the use of failure indices (FI) for all load cases. In general the failure index is determined by dividing the product of the occurring design

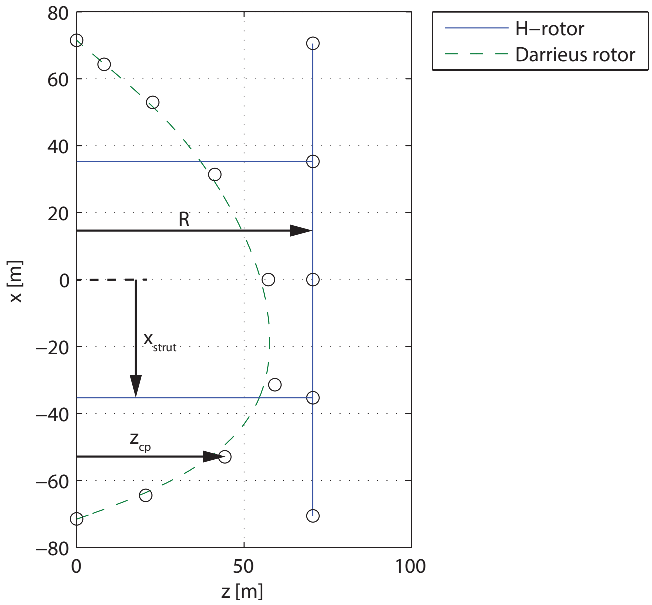

Figure 4.4: Shape variables of the optimization.

load and the safety factor by the allowable load, see Equation 4.7. A failure index value higher than 1 indicates failures. For ultimate strength failure, the failure index of each element is determined in axial, transverse, and shear direction using the occurring stresses from the FEM analysis and the laminate strengths.

$$FI = \frac{\text{Design load} \cdot SF}{\text{Allowable load}} \tag{4.7}$$

The damage D, due to fatigue is determined using Equation 3.4. The damage is a non-linear function of the applied load. To make the failure index appear linear and thereby help the optimization to converge, the 6th root of the fatigue damage is taken as failure index, see Equation 4.8. The safety factor already needs to be taken into account when determining the allowable number of load cycles using the S-N curves.

$$FI = D^{\frac{1}{6}} \tag{4.8}$$

The failure index for buckling is determined using the (minimum) eigenvalue corresponding to the first occurring buckling mode. The buckling eigenvalue is a linear function of the applied load. The buckling failure index is the reciprocal of this eigenvalue, see Equation 4.9. The safety factor is used as input for MSC Nastran to find the buckling modes.

$$FI = EV_{\min}^{-1} \tag{4.9}$$

The failure indices are translated to inequality constraints by subtracting 1, see Equation 4.10. A feasible design is indicated by values below zero for all the inequality constraints.

$$c_{ineq} = FI - 1 \tag{4.10}$$

In the optimizations which evaluate one rotor size (power capacity), the rotor projected rotor area needs to be kept constant. For the H-rotor, a given projected rotor area and rotor height yields the rotor radius. The projected rotor area of the Darrieus rotor is more complex to control. Two non-linear inequality constraints are added for these Darrieus rotor optimization. The first one imposes a minimum projected rotor area of the area corresponding to the evaluated rotor size. The second constraint imposes a maximum projected rotor area of 110% the evaluated rotor size.

4.6 Optimization bounds and linear constraints

Bounds and linear constraints are imposed on the design vector during the optimization. These bounds and constraints limit the design space, such that only feasible laminate thicknesses and shapes are evaluated during the optimization. The laminate thicknesses and H-rotor shape variables are only subject to lower and upper bounds, see Table 4.2. Next to bounds, a linear constraint is imposed on the shape variables of the Darrieus rotor. The linear constraint does not allow the position of two adjacent, variable control points of the blade beam axis to vary more than 50 meter. Furthermore, the upper and lower variable control point positions are not allowed to be larger than the adjacent, variable control point location.

Table 4.2: Bounds for design variables.

Design variable	Lower bound	Upper bound
t [mm]	5	150
R [m]	3.5	350
$\frac{x_{\text{strut}}}{H}$ [-]	0.1	0.4
$z_{\text{cp } 2,\ldots,6}$ [m]	3.5	350
$z_{\text{cp upper\&lower}}$ [m]	3.5	165

4.7 Optimization sequence

Three optimization types are identified according to the types of design parameters. Both the baseline H-rotor and Darrieus rotor are optimized using these three optimization types. The complexity of the optimization types is increased stepwise. First, sizing optimizations are performed. In the sizing optimization only sizing variables are used.

Second, shape optimizations are performed. The shape optimization only uses the shape variables. Subsequently, the two optimizations are combined. The combined optimization uses both the sizing and shape variables.

For the sizing and combined optimization of the baseline rotors, two optimizations per rotor configuration are performed using a different section division. This allows investigating the influence of the applied number of sections on the structural rotor performance. First, only a single section along the strut and blade is used. Subsequently, 5 sections along the blade and 4 along the strut are used. The shape optimization of the baseline rotors is only performed using a single section along the blade and strut.

The resulting designs of the combined optimizations (multiple sections) are used for more thorough structural analysis. Resonance and the minimum emergency stop braking time of the rotors are analyzed. The loads carried by the rotor are decomposed and the loads driving the design are identified. Furthermore, a more thorough buckling and fatigue analysis is performed. The results are used to assess the feasibility of the optimized designs.

A set op optimized designs for different rotor sizes and rotor heights is required to construct the scaling trends. Combined optimizations are performed for 3, 5, 8, 10, 15, and 20 MW and for 100, 140, and 180 m tall rotors. Performing optimizations for 6 rotor sizes, 3 rotor heights, and 2 rotor configurations yields a total of 36 optimizations. Additionally, a 260 m tall Darrieus rotor is evaluated for the 15 and 20 MW rotor sizes. The sequence of optimization is summarized in Table 4.3.

Table 4.3: Optimization sequence.

Opt. no.		**Opt. type**	**No. of axial sections**	**Area constraint**	**Remarks**
1.	a)	sizing	blade: 1 strut: 1	no	-
	b)	sizing	blade: 5 strut: 4	no	-
2.	a)	shape	blade: 1 strut: 1	no	-
	b)	shape	blade: 5 strut: 4	no	-
3.	a)	combined	blade: 1 strut: 1	no	-
	b)	combined	blade: 5 strut: 4	no	-
4.		combined	blade: 5 strut: 4	yes	Sizes: 3, 5, 8, 10, 15 & 20 MW; heights: 100, 140, 180 & 260[a] m

[a] Only the 15 and 20 MW Darrieus rotors are evaluated for a rotor height of 260 m.

4.8 Optimization starting points

The gradient based optimization algorithms take one design as a starting point for the optimization. In general a good starting point (close to the optimum point) decreases the convergence time of the optimization. For both the Darrieus rotor and H-rotor a baseline shape is appointed. The geometrical properties of both baseline rotors are summarized in Table 4.4. Table 4.5 and Table 4.6 state the values of the shape variables for respectively the baseline H-rotor and Darrieus rotor. The shape outlines of the baseline rotors are illustrated in Figure 4.4. Primarily, these baseline shapes are used as initial shapes in performing the sizing, shape, and combined optimization.

The optimizations for different rotor sizes and rotor heights require different initial shapes. For a given rotor height, the radial positions of the blade control points are scaled to match the rotor projected area to the evaluated rotor size.

Table 4.4: Properties for baseline rotor designs.

Property	H-rotor	D-rotor
Rotor diameter [m]	141	115
Rotor height [m]	141	143
Diameter-to-height [-]	1.00	0.80
Chord length [m]	4.70	3.84
Twist [deg]	-1.5	-1.5
Projected rotor area [m^2]	19,881	11,332
Equivalent power capacity [MW]	9.0	5.2

Table 4.5: Shape parameter values for baseline H-rotor.

Shape variable	Value
R [m]	70.5
$\frac{x_{\text{strut}}}{H}$ [-]	0.25

Table 4.6: Control point locations for baseline Darrieus rotor.

Control point no.	x-position [m]	z-position [m]
1	-64.4	20.7
2	-52.9	44.2
3	-31.5	59.1
4	0	57.3
5	31.5	41.3
6	52.9	22.7
7	64.4	8.2

Chapter 5

Optimization results

Optimizations are performed according to the method described in the previous chapter. This chapter presents their results. First; the sizing, shape, and combined optimizations of the baseline H-rotor and Darrieus rotor are addressed. Second, failure of the rotor designs resulting from the combined optimizations is more extensively analyzed. To conclude this chapter, combined optimizations are performed for different rotor sizes and heights.

5.1 Sizing optimization

The first set of sizing optimizations use a single section along the length of the blade and struts. In the second set of sizing optimizations, the blade uses 5 sections and the struts use 4 sections along their length. The results of the sizing optimizations are presented in Table 5.1.

Internal loads of the optimized H-rotor and Darrieus rotor blade are shown in Figure 5.1 and Figure 5.3. (More plots are provided in Appendix C and Appendix D.) In normal operation, during one revolution, the rotors experience the largest flapwise bending moments in the downwind blade position, since the normal aerodynamic force and the centrifugal force on the blade act in the same direction. In the upwind blade position, the normal aerodynamic force and centrifugal force act in the opposite direction. This causes a change of sign of the maximum blade deflection for both the H-rotor and Darrieus rotor blade, shown in Figure 5.2 and Figure 5.4. The edgewise bending moment is largest in the upwind position. The single and multiple sections H-rotor optimization result in exact the same edgewise bending moment and difference in flapwise bending moment in the blade.

The failure modes of the multiple sections optimized H-rotor are illustrated in Figure 5.5. (More plots are provided in Appendix C.) The highest ultimate strength failure indices in the H-rotor blade can be found in the girders and skin near the strut connections, at the downwind blade position. The highest fatigue damage is also found in the girders and skin near the strut connections, see Figure 5.8. The highest ultimate strength indices in

Table 5.1: Sizing optimization results.

Property	H-rotor		Darrieus rotor	
$n_{\text{sec, blade}}$ [-]	1	5	1	5
$t_{\text{girder, max}}$ [mm]	28.2	24.9	26.2	21.5
$t_{\text{girder, min}}$ [mm]	-	9.6	-	10.1
$t_{\text{shear web, max}}$ [mm]	8.0	11.0	5.0	6.9
$t_{\text{shear web, min}}$ [mm]	-	7.1	-	6.0
$t_{\text{skin, max}}$ [mm]	7.9	10.0	14.1	11.9
$t_{\text{skin, min}}$ [mm]	-	5.4	-	6.3
n_{struts} [-]	2	2	0	0
$n_{\text{sec, strut}}$ [-]	1	4	-	-
$t_{\text{strut, max}}$ [mm]	22.9	27.0	-	-
$t_{\text{strut, min}}$ [mm]	-	14.0	-	-
$h_{\text{strut, tip}}$ [m]	0.72	0.52	-	-
$w_{\text{strut, tip}}$ [m]	0.80	0.95	-	-
$h_{\text{strut, base}}$ [m]	1.60	1.31	-	-
$w_{\text{strut, base}}$ [m]	1.18	1.18	-	-
Blade mass [kg]	24,875	18,845	30,373	17,694
Strut mass [kg]	4146	3438	-	-
Projected rotor area [m^2]	19,881	19,881	11,332	11,332
Maximum FI				
- Ult. strength DW [-]	0.41	0.40	0.36	0.38
- Ult. strength UW [-]	0.46	0.53	0.24	0.52
- Ult. strength P [-]	0.32	0.27	0.21	0.20
- Fatigue [-]	0.91	0.92	0.98	1.00
- Ult. buck DW [-]	1.00	1.05	0.30	0.77
- Ult. buck P [-]	0.63	0.83	0.34	0.73
Critical LC	Buck DW	Buck DW	Fatigue	Fatigue
Initial rotor mass over area [$\frac{kg}{m^2}$]	7.40	6.27	9.11	9.11
Reduction factor [-]	0.68	0.62	0.88	0.51
Minimized rotor mass over area [$\frac{kg}{m^2}$]	5.00	3.88	8.04	4.68
Max. constraint violation [-]	0	5.48e-2	0	8.65e-4

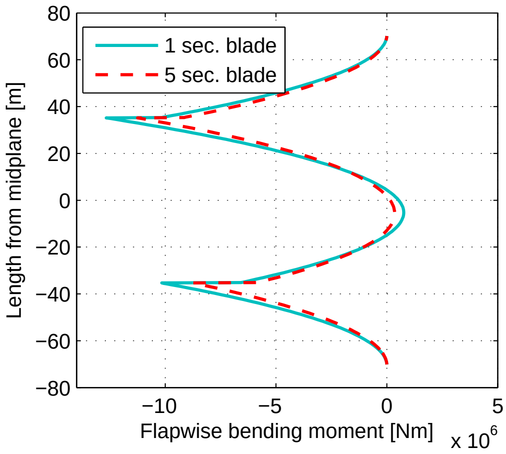

(a) Internal flapwise bending moment DW.

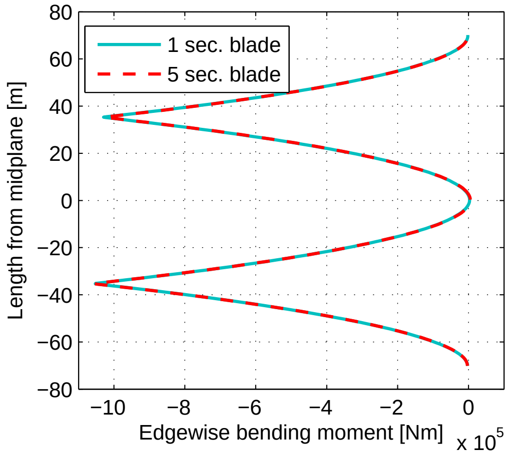

(b) Internal edgewise bending moment UW.

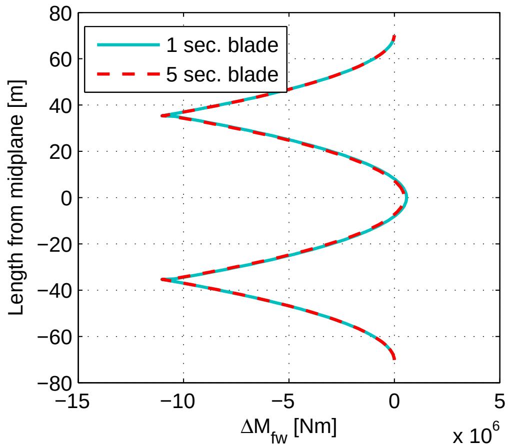

(c) Difference in flapwise bending moment between UW & DW.

Figure 5.1: Internal loads of H-rotor.

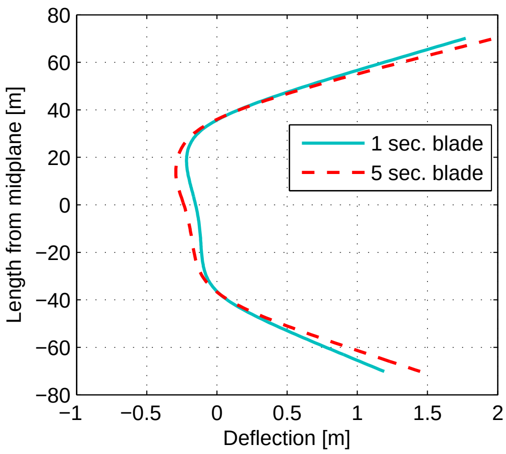

(a) Blade deflection DW (in z-direction).

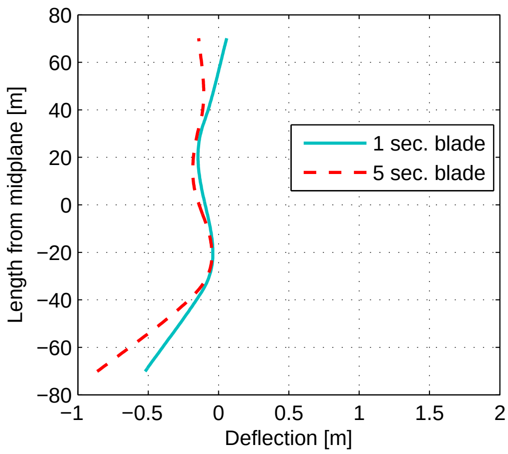

(b) Blade deflection UW (in z-direction).

Figure 5.2: Blade deflection of H-rotor.

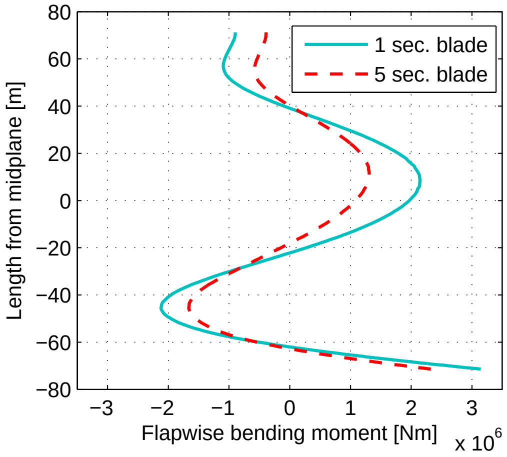

(a) Internal flapwise bending moment DW.

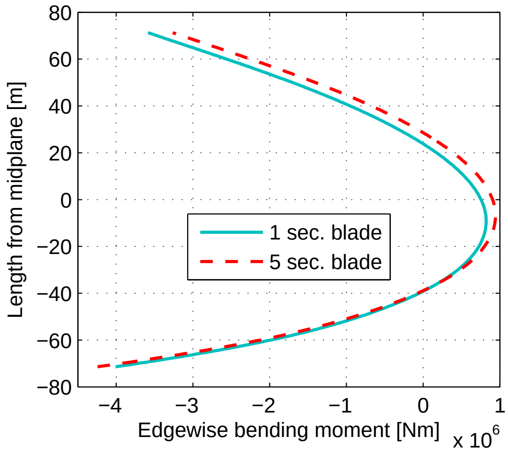

(b) Internal edgewise bending moment UW.

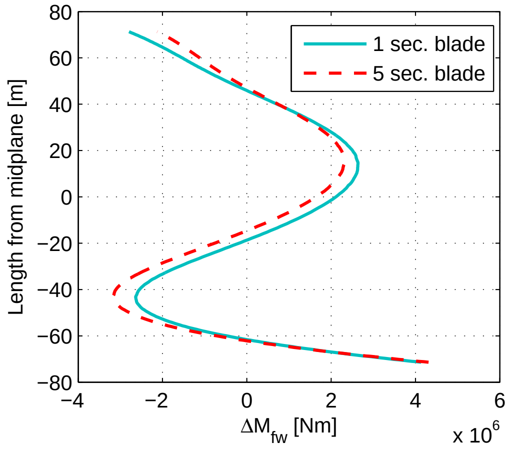

(c) Difference in flapwise bending moment between UW & DW.

Figure 5.3: Internal loads of Darrieus rotor.

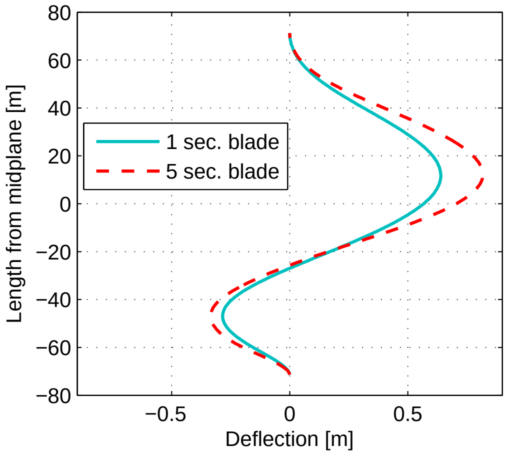

(a) Blade deflection DW (in z-direction).

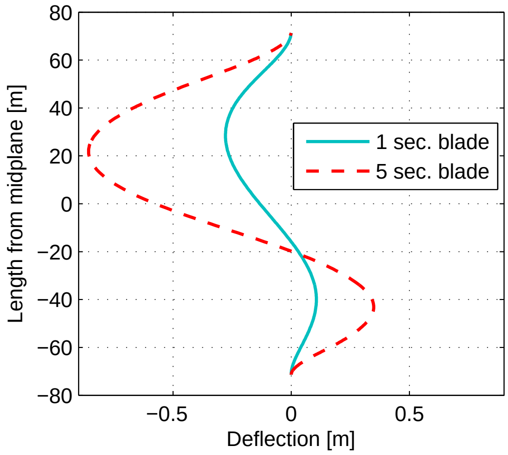

(b) Blade deflection UW (in z-direction).

Figure 5.4: Blade deflection of Darrieus rotor.

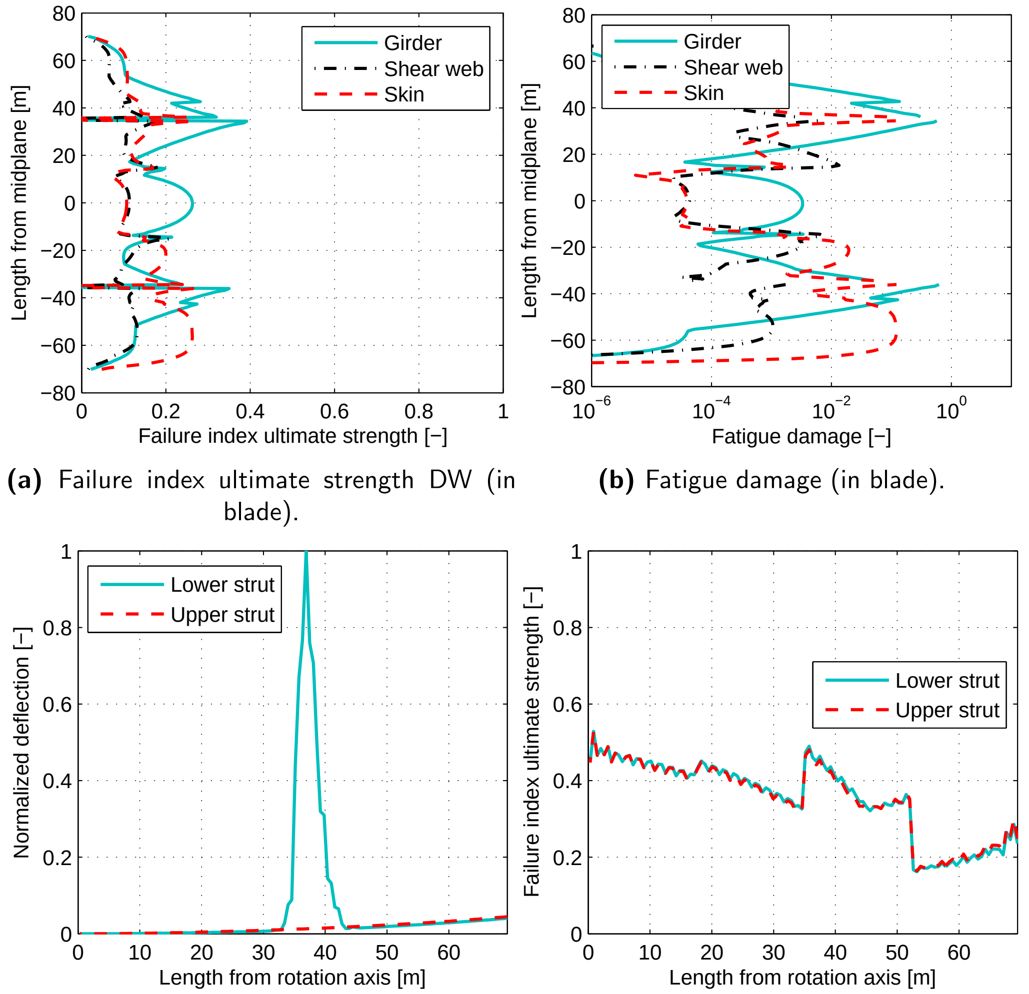

(a) Failure index ultimate strength DW (in blade).

(b) Fatigue damage (in blade).

(c) First buckling mode DW (in strut).

(d) Failure index ultimate strength UW (in strut).

Figure 5.5: Failure modes of multiple section H-rotor.

the struts are found at the root, at the upwind blade position. Buckling occurs first in middle of the strut, see Figure 5.7

The failure modes of the multiple sections optimized Darrieus rotor are illustrated in Figure 5.6. (More plots are provided in Appendix D.) The highest ultimate strength failure indices can be found in the girders near the point of maximum curvature, at the downwind blade position. High values for the fatigue damage are found along a large part of the length of the blade, see Figure 5.10. Buckling occurs first at the lower root of the blade.

In Figure 5.9 and Figure 5.11, the direction of the maximum fatigue damage is illustrated. In these figures, the most critical fatigue loading direction is illustrated per section of the structure.

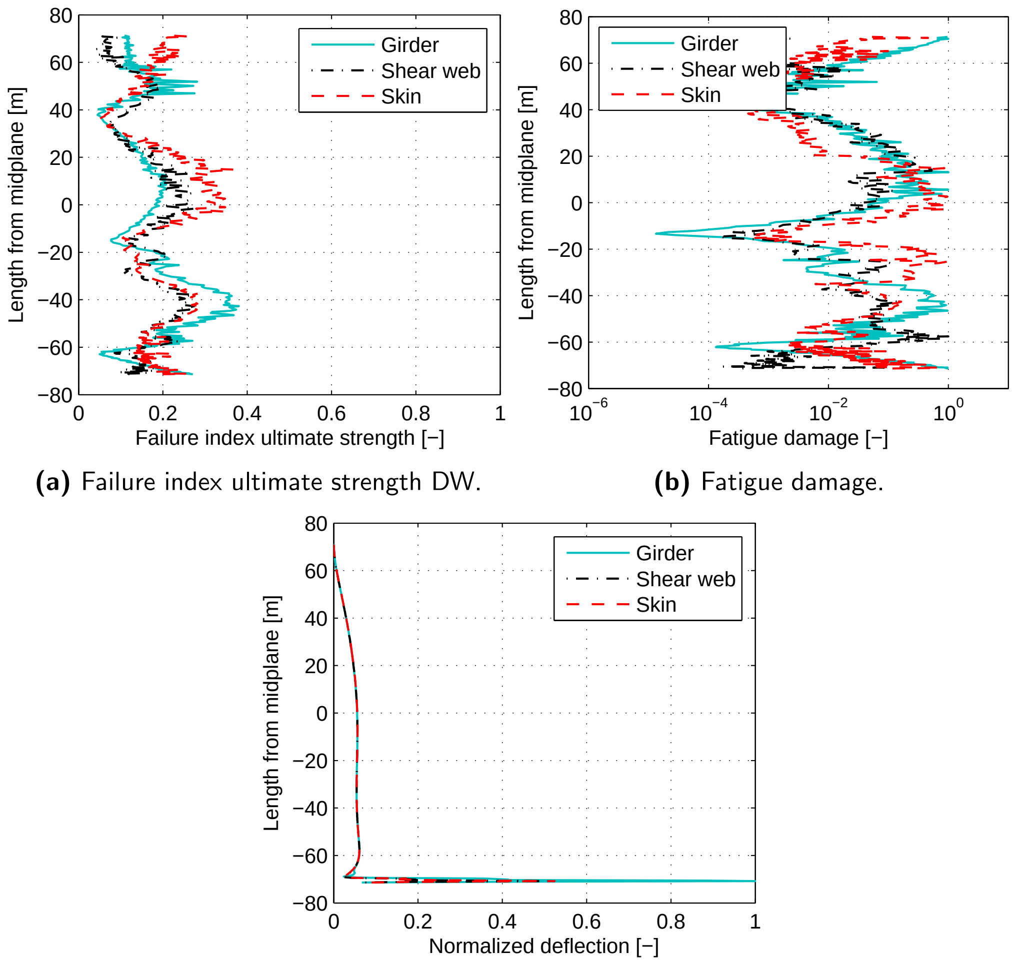

(a) Failure index ultimate strength DW.

(b) Fatigue damage.

(c) First buckling mode (DW).

Figure 5.6: Failure modes of multiple section Darrieus rotor.

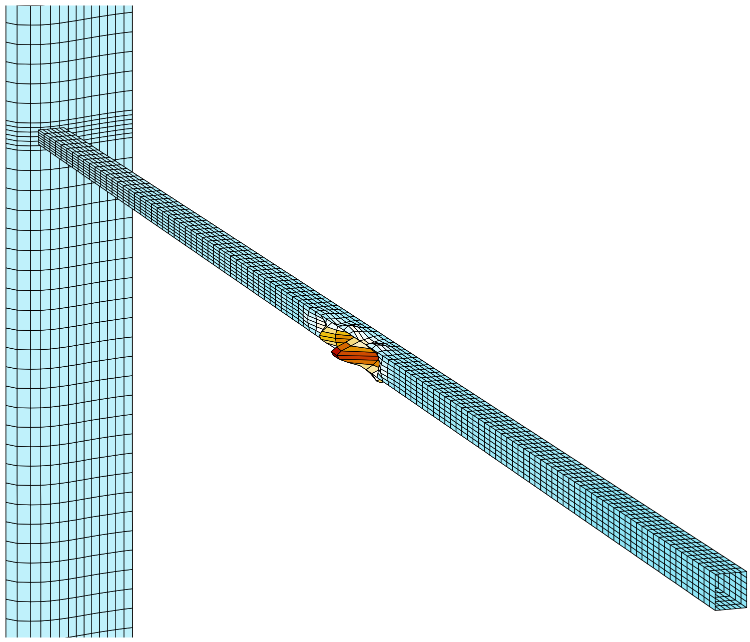

Figure 5.7: Local buckling in the H-rotor strut at the downwind position of the blade.

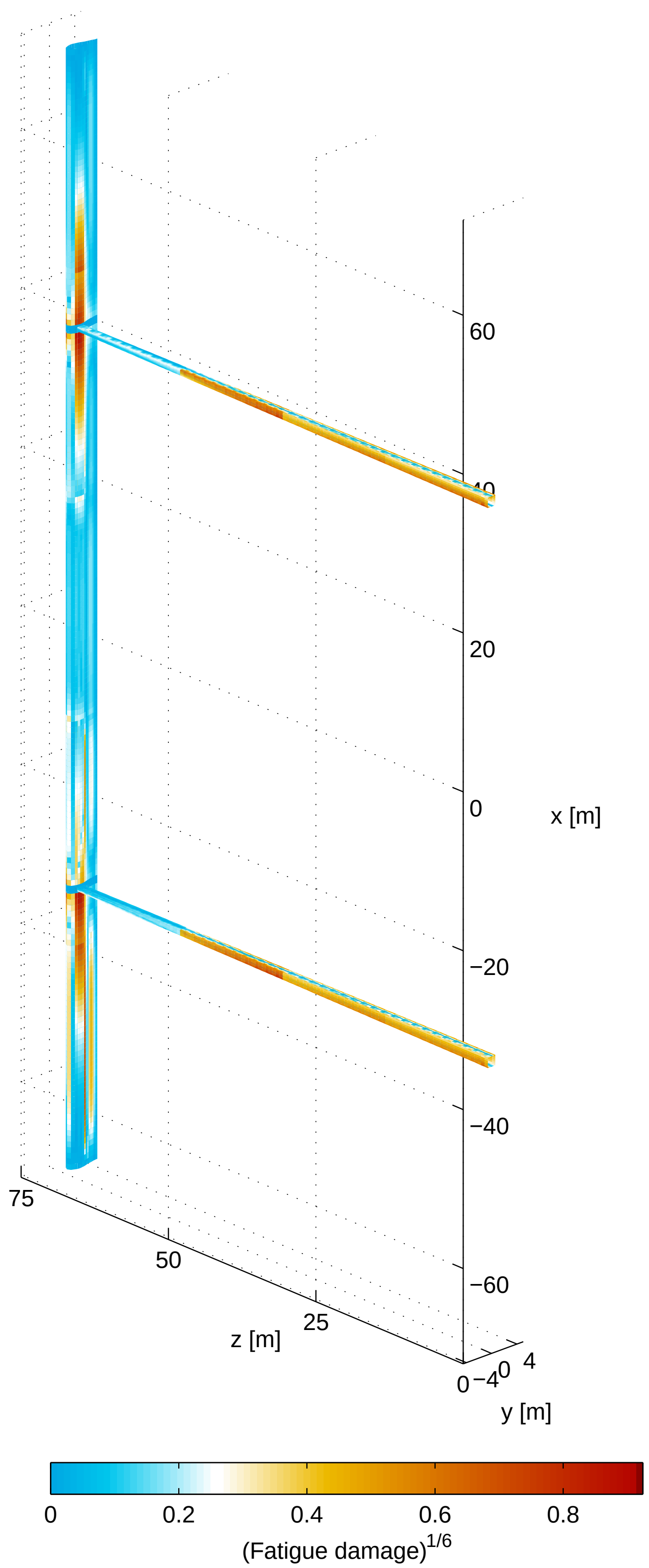

Figure 5.8: Fatigue damage of the optimized H-rotor (multiple sections).

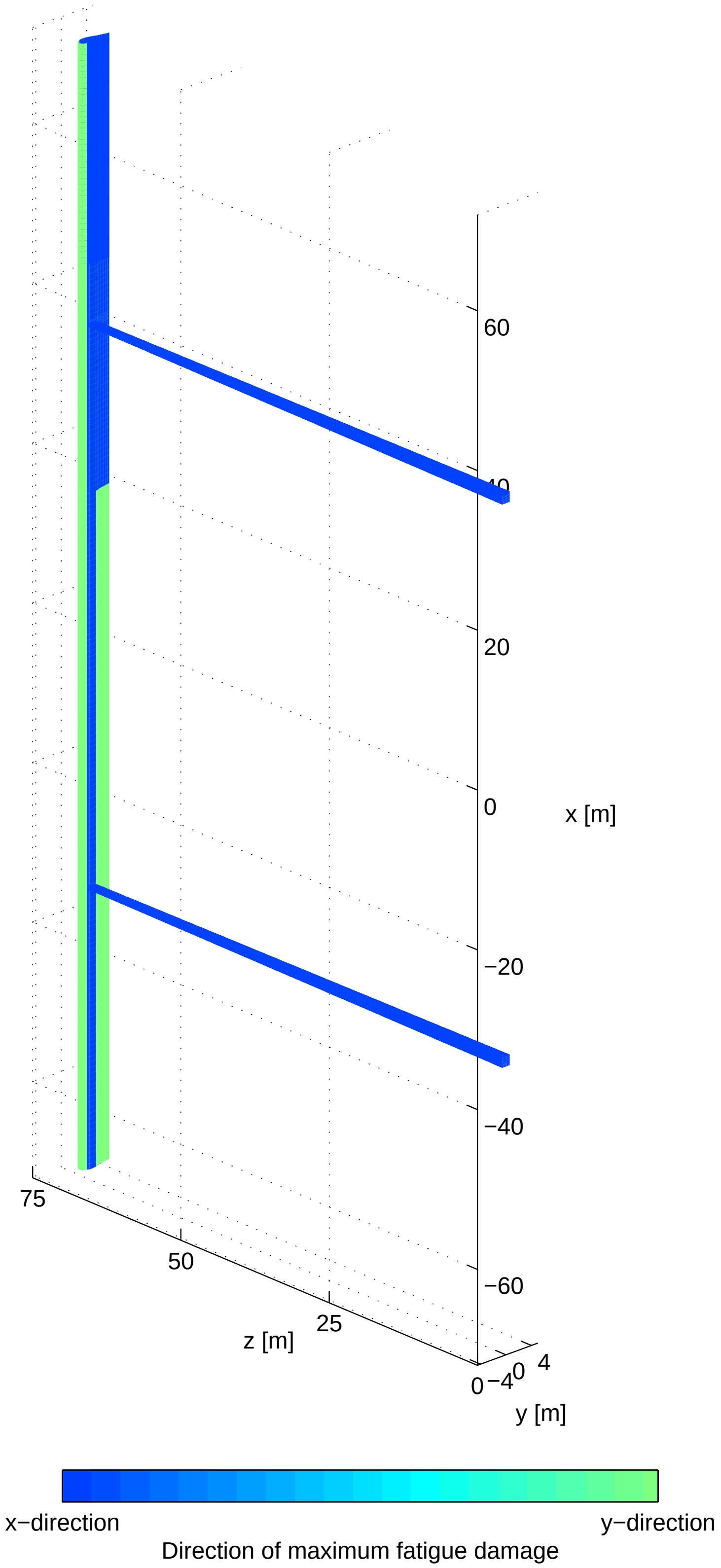

Figure 5.9: Maximum fatigue damage direction per section of the optimized H-rotor (multiple sections).

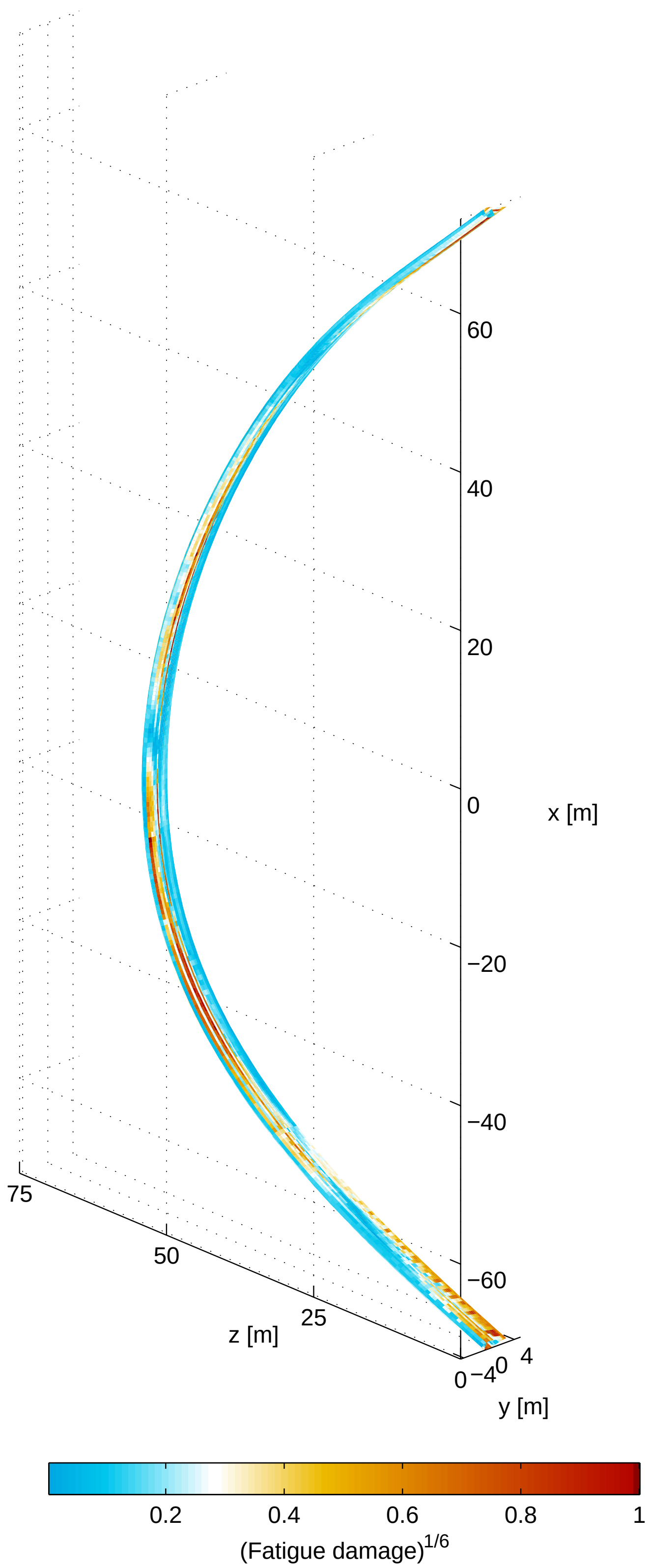

Figure 5.10: Fatigue damage of the optimized Darrieus rotor (multiple sections).

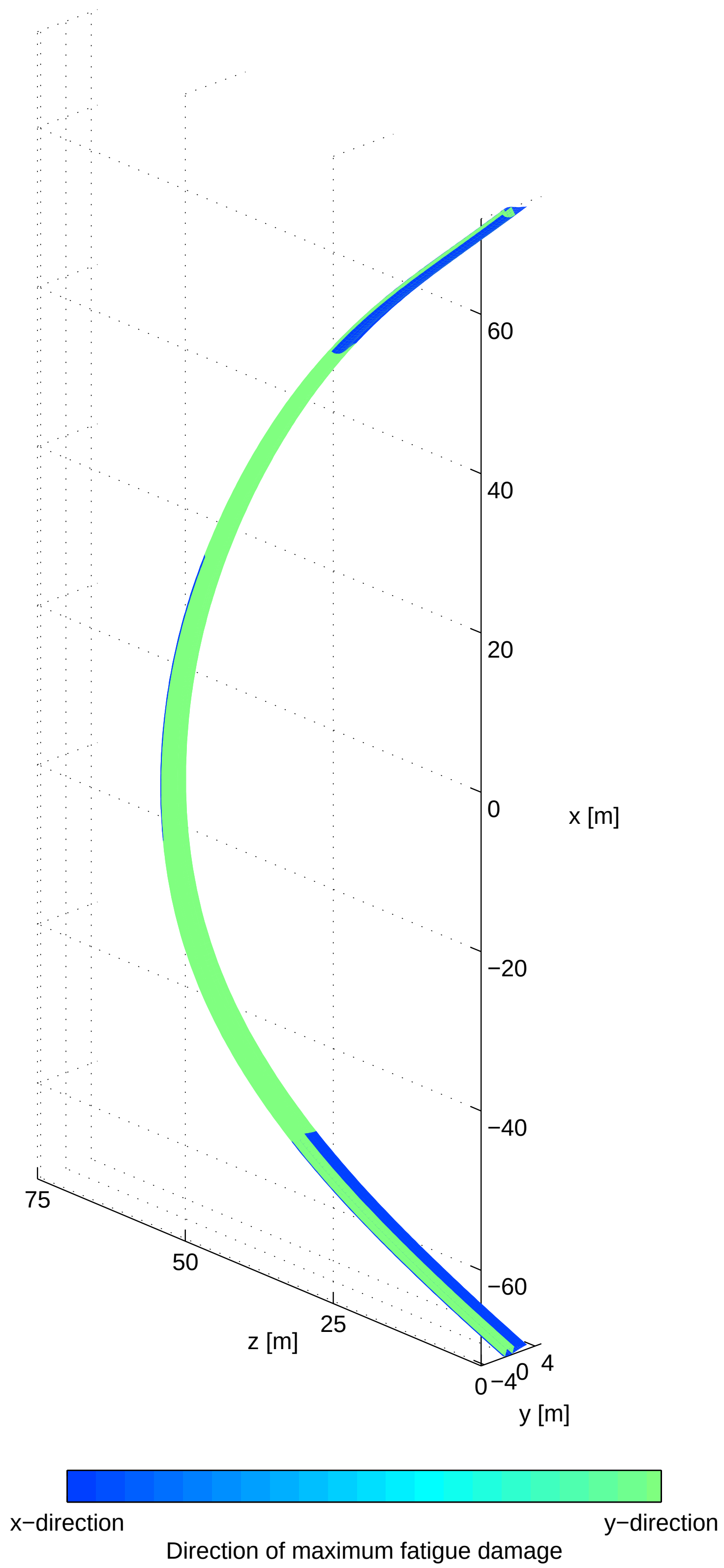

Figure 5.11: Maximum fatigue damage direction per section of the optimized Darrieus rotor (multiple sections).

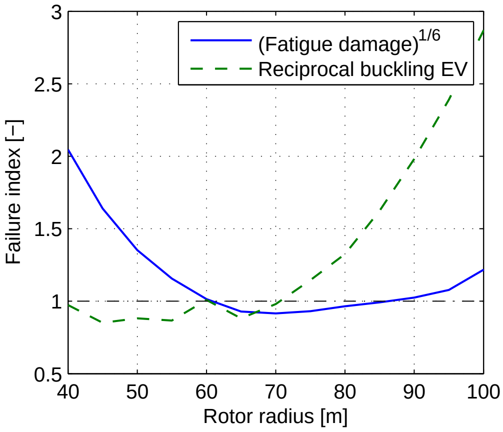

(a) Feasible region H-rotor design.

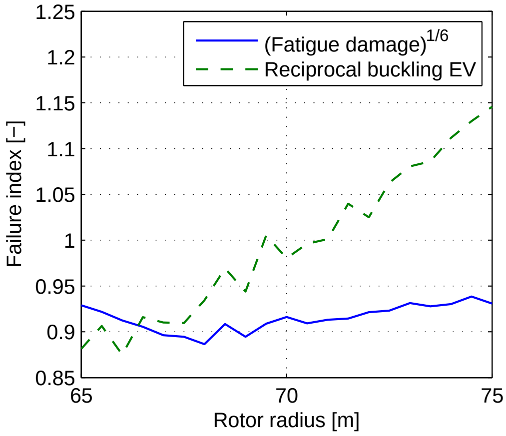

(b) Zoomed in on the critical failure indices.

Figure 5.12: Critical failure indices of the H-rotor shape optimization.

5.2 Shape optimization

Only the rotors with the single section blade and struts are shape optimized. The results of the shape optimizations are shown in Table 5.2.

For the shape optimization of the H-rotor, the strut locations are frozen and only the rotor radius is varied. The shape optimization of the H-rotor stops after 1 iteration virtually at the same point as the starting point. The effect of the rotor radius on the failure indices is illustrated in Figure 5.12a. For an increase in the rotor radius, failure occurs due to buckling in the downwind blade position. In contrast, for a decrease in the rotor radius, failure occurs due to fatigue damage. A rotor radius of roughly 60 to 70 m yields a feasible rotor design.

The shape optimization of the Darrieus rotor does yields an improvement of the objective function. The optimization yields a symmetric shape with respect to the midplane, shown in Figure 5.13. The radius of the rotor is reduced with 16%, while the projected rotor area is reduced with only 9%. The shape optimization yields a 19% mass reduction of the blade. (Plots of the internal loads and failure indices along the length of the blade are attached in Appendix E.)

5.3 Combined optimization

The first set of combined optimizations use a single section along the length of the blade and struts. In the second set of combined optimizations, the blade uses 5 sections and the struts use 4 sections along the length. The results of the combined optimizations are presented in Table 5.3.

The combined optimizations of the H-rotor use the same starting point as the multiple sections, sizing optimizations. The resulting shapes of the optimizations are shown in Figure 5.14. The radius of the single section optimized rotor is roughly the same as for the starting point. The radius of the multiple sections optimized rotor is decreased by

Table 5.2: Shape optimization results.

Property	**H-rotor**	**Darrieus rotor**
$n_{\text{sec, blade}}$ [-]	1	1
n_{struts} [-]	2	2
$n_{\text{sec, strut}}$ [-]	1	-
Rotor radius [m]	70.5	48.5
Diameter-to-height [-]	1.00	0.68
Blade mass [kg]	24,875	24,514
Strut mass [kg]	4146	-
Projected rotor area [m^2]	19,881	10,349
Maximum FI		
- Ult. strength DW [-]	0.41	0.44
- Ult. strength UW [-]	0.46	0.32
- Ult. strength P [-]	0.32	0.19
- Fatigue [-]	0.91	0.98
- Ult. buck DW [-]	0.99	0.48
- Ult. buck P [-]	0.63	0.26
Critical LC	Buck DW	Fatigue
Initial rotor mass over area [$\frac{kg}{m^2}$]	5.00	8.04
Reduction factor [-]	1.00	0.88
Minimized rotor mass over area [$\frac{kg}{m^2}$]	5.00	7.11
Max. constraint violation [-]	0	0

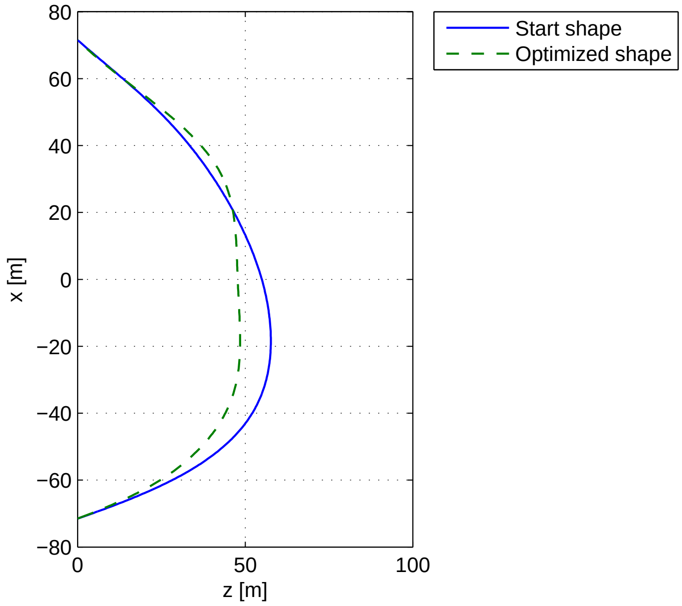

Figure 5.13: Resulting Darrieus rotor shape of shape optimization.

10% compared to the starting point. (Plots of the internal loads and failure indices along the blade and struts are attached in Appendix F.)

The combined optimizations of the Darrieus rotor use the same starting point as the shape optimization. The optimizations yield a 59% and 61% reduction of the objective function for respectively the single section and multiple sections optimization. The resulting shapes of the optimizations are shown in Figure 5.15. The rotor radius stays roughly constant for both the single and multiple sections optimization (respectively a 5% increase and a 4% decrease in radius), in contrast to the shape optimization. Similar to the shape optimization, the shapes tend to be symmetric with respect to the midplane. (Plots of the internal loads and failure indices along the blade are attached in Appendix G.)

Table 5.3: Combined optimization results.

Property	H-rotor		Darrieus rotor	
$n_{sec,\ blade}$ [-]	1	5	1	5
$t_{girder,\ max}$ [mm]	20.2	24.7	8.1	12.3
$t_{girder,\ min}$ [mm]	-	13.2	-	5.3
$t_{shear\ web,\ max}$ [mm]	9.6	7.1	5.2	5.1
$t_{shear\ web,\ min}$ [mm]	-	6.4	-	5.0
$t_{skin,\ max}$ [mm]	7.5	9.6	6.6	8.1
$t_{skin,\ min}$ [mm]	-	6.3	-	5.1
n_{struts} [-]	2	2	0	0
$n_{sec,\ strut}$ [-]	1	4	-	-
$t_{strut,\ max}$ [mm]	23.6	21.5	-	-
$t_{strut,\ min}$ [mm]	-	13.0	-	-
$h_{strut,\ tip}$ [m]	0.62	0.61	-	-
$w_{strut,\ tip}$ [m]	0.92	1.03	-	-
$h_{strut,\ base}$ [m]	1.60	1.19	-	-
$w_{strut,\ base}$ [m]	1.11	1.26	-	-
Rotor radius [m]	71.8	64.0	60.6	55.4
Diameter-to-height [-]	1.02	0.91	0.85	0.77
Blade mass [kg]	20,219	16,040	12,573	10,611
Strut mass [kg]	4309	2760	-	-
Projected rotor area [m^2]	20,236	18,060	11,517	10,287
Maximum FI				
- Ult. strength DW [-]	0.37	0.39	0.40	0.49
- Ult. strength UW [-]	0.51	0.46	0.62	0.57
- Ult. strength P [-]	0.28	0.36	0.25	0.24
- Fatigue [-]	0.98	0.99	0.99	0.98
- Ult. buck DW [-]	1.00	1.08	1.00	0.97
- Ult. buck P [-]	0.50	0.80	1.00	0.81
Critical LC	Fatigue & Buck DW	Fatigue & Buck DW	Fatigue, Buck DW & P	Fatigue & Buck DW
Initial rotor mass over area [$\frac{kg}{m^2}$]	6.27	6.27	8.04	8.04
Reduction factor [-]	0.68	0.57	0.41	0.39
Minimized rotor mass over area [$\frac{kg}{m^2}$]	4.27	3.58	3.28	3.09
Max. constraint violation [-]	0	0.082	3.94e-04	0

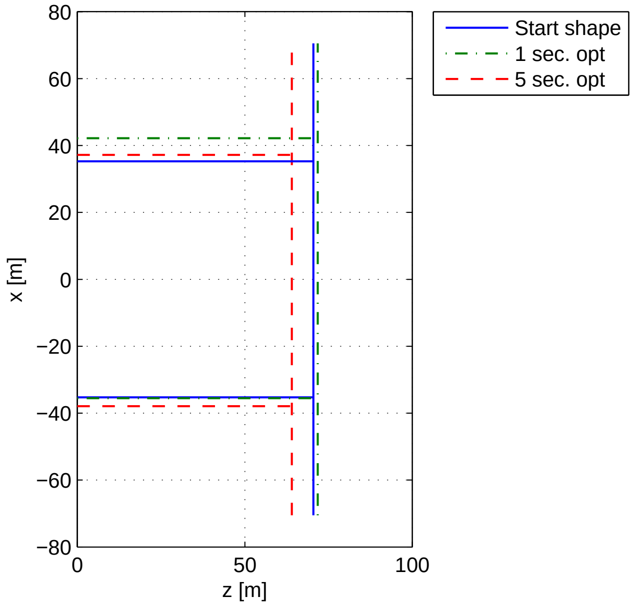

Figure 5.14: Resulting H-rotor shapes of combined optimizations.

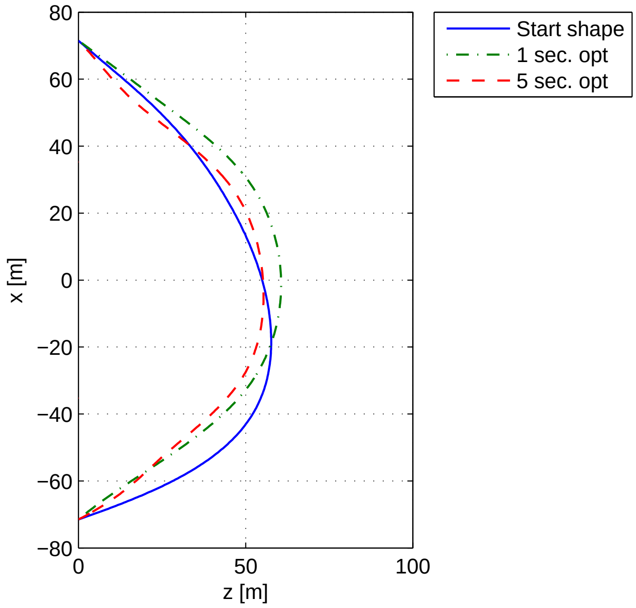

Figure 5.15: Resulting Darrieus rotor shapes of combined optimizations.

5.4 Post optimization analysis

Further analysis is performed on the rotor designs resulting from the combined optimizations using multiple blade and strut sections. Failure of the rotors is analyzed more thoroughly by accounting for stiffening of the structure due the rotation of the rotor and using a higher mesh density. Fatigue is more thoroughly analyzed by evaluating more azimuthal blade positions. Furthermore; the undamped, free vibration modes of the rotor and the emergency stop braking time are evaluated.

To account for the additional stiffness of the rotor structure due to the rotation, two successive analyses are performed using MSC Natran (using two subcases). The first analysis is used to determine the additional stiffness. For the second analysis, the stiffness matrix is updated. The pre-stiffening is applied to the structural resonance and buckling analysis. The stresses in the structure resulting from the linear analysis are not affected by the pre-stiffening, therefore the results for the ultimate and fatigue load case stay unchanged.

5.4.1 Structural resonance analysis

The undamped, free vibration modes are identified for both the H-rotor and the Darrieus. Their mode shapes are shown in Figure 5.16 and Figure 5.17. The Campbell diagrams in Figure 5.18 and Figure 5.19 show the relation between the eigenfrequencies and angular velocity of the rotor. The dashed lines in the figures are the harmonic lines of the rotation frequency. The intersection of these harmonic lines with the eigenfrequencies of the modes could indicate resonance. Some modes are only excited by the odd harmonic lines, others are only excited by the even harmonic lines. The harmonic lines of 5P and higher are believed not to cause resonance, because they do not contain sufficient energy [13]. For the H-rotor, it can be seen that the strut modes (SM) cross the 2P line near the design rotational speed. This indicates resonance of the rotor at the rated wind speed. For the Darrieus rotor, the first blade mode (BM) crosses the 3P line close to the design rotational speed. Further analysis is required to assess the strength of the resonance.

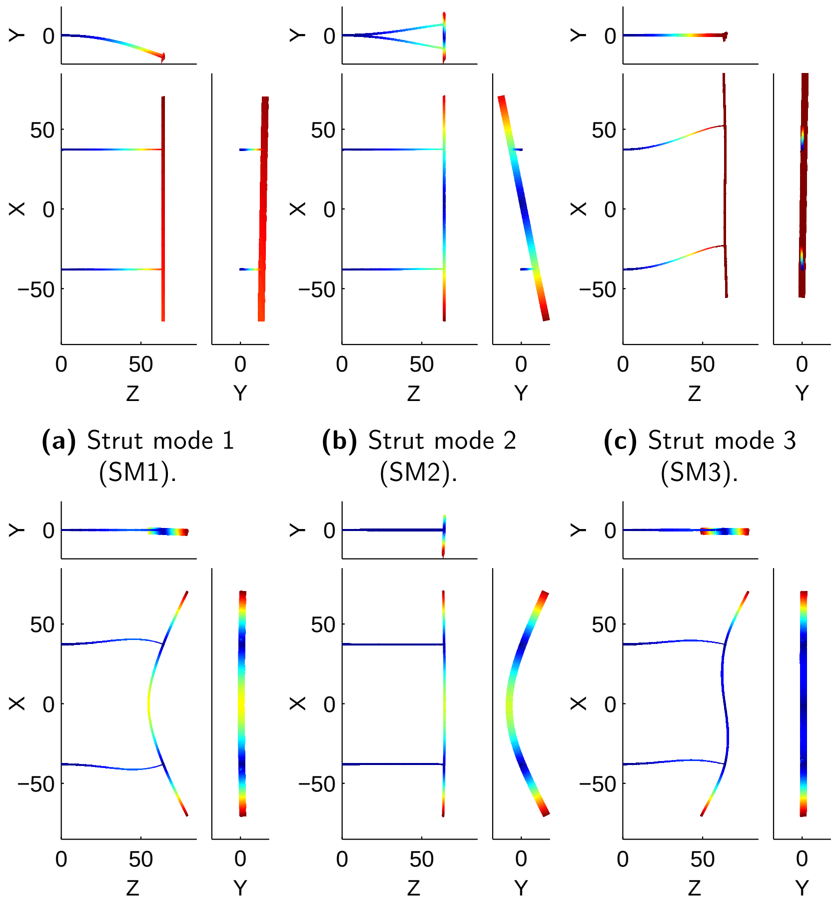

(a) Strut mode 1 (SM1).

(b) Strut mode 2 (SM2).

(c) Strut mode 3 (SM3).

(d) Blade mode 1 (BM1).

(e) Blade mode 2 (BM2).

(f) Blade mode 3 (BM3).

Figure 5.16: Mode shapes of the H-rotor.

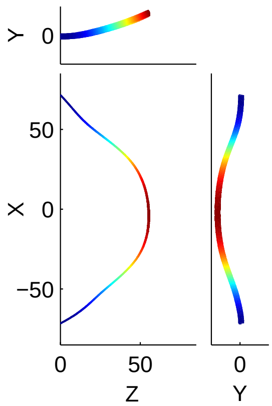

(a) Blade mode 1 (BM1).

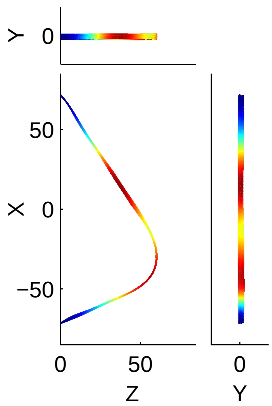

(b) Blade mode 2 (BM2).

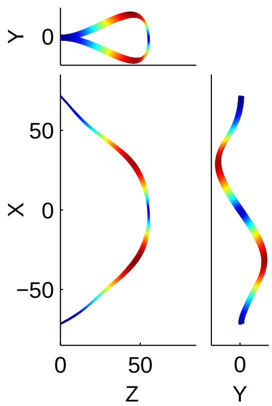

(c) Blade mode 3 (BM3).

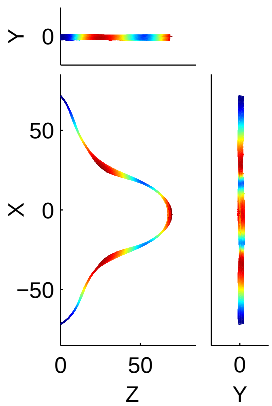

(d) Blade mode 4 (BM4).

Figure 5.17: Mode shapes of the D-rotor.

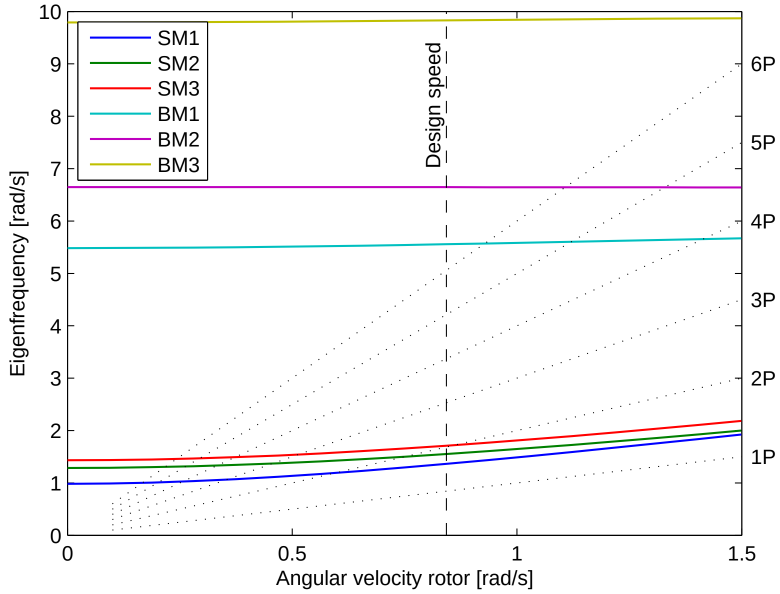

Figure 5.18: Campbell diagram of the H-rotor.

5.4.2 Buckling analysis

The pre-stiffening of the rotor structure results in higher eigenvalues of the buckling modes. A higher eigenvalue means that buckling occurs at higher loads. Table 5.4 and Table 5.5 show, for two mesh factors, the difference in the eigenvalues of the first occurring buckling mode, for applying and not applying pre-stiffening. A mesh factor of 1 indicates the same mesh as used for the optimization.

Table 5.4: Effect of pre-stiffening on the buckling eigenvalues of the H-rotor.

f_{mesh}	$n_{elements}$	Operation eigenvalue no pre-stiffening	Operation eigenvalue pre-stiffening	Parked eigenvalue
1	13,248	0.924	2.478	1.247
2	54,864	0.452	1.12	0.828

5.4.3 Extended fatigue analysis

The extent of the fatigue analysis in the optimizations is limited. This section extends the fatigue analysis by evaluating more azimuthal blade positions, to better approximate the variation of the load in a revolution. The applied method in the optimizations is only able to find one load cycle with the same period as one revolution of the rotor. The maximum and minimum of this cycle are determined by the aerodynamic loads corresponding to the downwind and upwind blade position in Figure 3.3. By evaluating more azimuthal positions and applying the rainflow counting method, multiple load cycles can be identified. In the extended fatigue analysis, 16 azimuthal positions are evaluated,

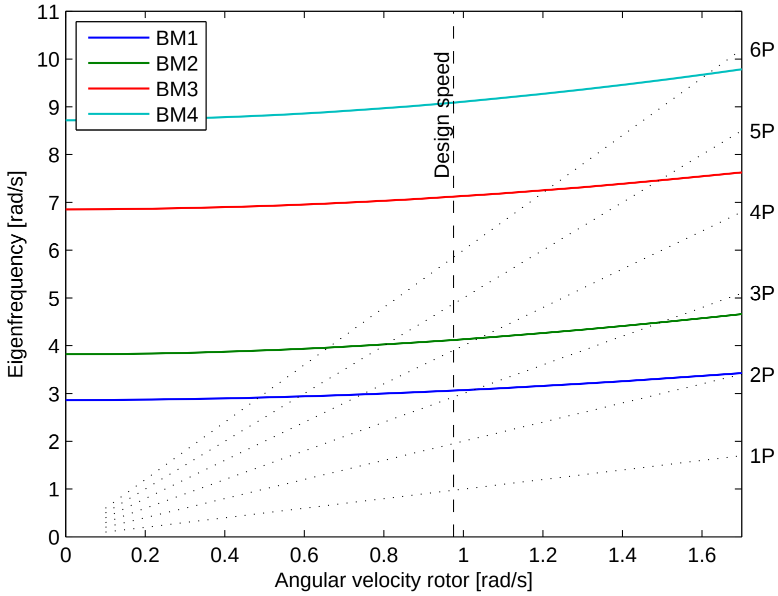

Figure 5.19: Campbell diagram of the Darrieus rotor.

Table 5.5: Effect of pre-stiffening on the buckling eigenvalues of the Darrieus rotor.

f_{mesh}	$n_{elements}$	Operation eigenvalue no pre-stiffening	Operation eigenvalue pre-stiffening	Parked eigenvalue
1	11,160	1.028	3.321	1.230
2	48,360	0.570	2.007	0.719

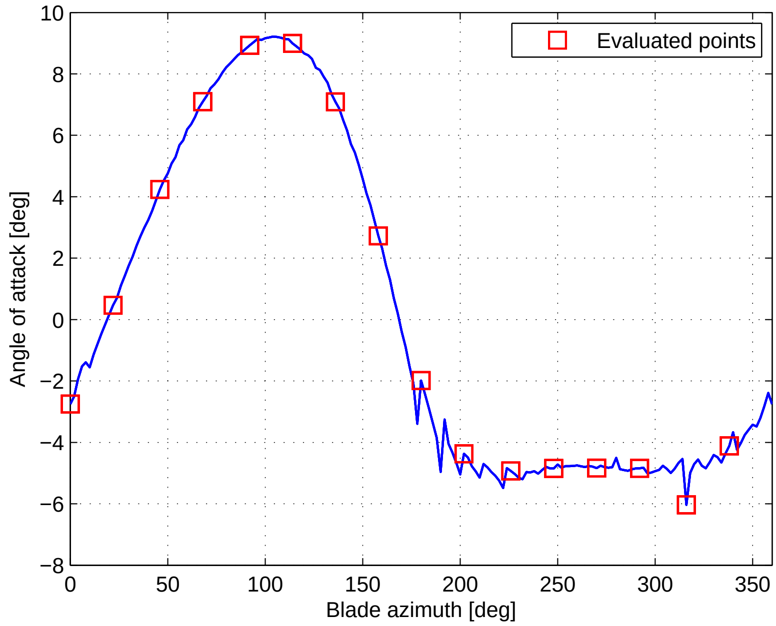

Figure 5.20: Evaluated azimuthal blade positions during extended fatigue analysis.

these points are indicated in Figure 5.20. The extent of this fatigue analysis is still limited, in the sense that only the normal operation conditions at one wind speed are considered.

Figure 5.21a shows the cyclic stress in the H-rotor element with the highest fatigue damage. A single load cycle is identified. The maximum and minimum of this load cycle are located at an azimuth angle of respectively 316 and 92 degrees, earlier defined as the downwind and upwind blade position. For this blade element, the extended fatigue analysis results in the same fatigue damage as the fatigue analysis performed during the optimization.

In Figure 5.21b, the cyclic stress in the strut element with the highest fatigue damage is shown. Multiple load cycles can be identified. Therefore, the fatigue damage changes for this strut element. The 2 and 16 evaluation points fatigue damages are respectively 0.10 and 0.59. In Figure 5.22, the fatigue damages from both analyses are shown along the length of the blade and strut. The fatigue damage of the structural members of the blade are not significantly increased by the extended fatigue analysis, in contrast to the fatigue damage of the strut.

Figure 5.23 shows the cyclic stress in the Darrieus blade element based on 2 and 16 evaluation points. In Figure 5.23b, the minimum turns out to be a maximum when using 16 evaluation points. The 2 and 16 evaluation points fatigue damages are respectively 0.35 and 9.58. In Figure 5.24, the fatigue damages from both analyses are shown along the length of the blade. It can be observed that the fatigue damage is increased significantly by the extended fatigue analysis in the shear web and the skin of the blade. The increase in fatigue damage is mainly located at the roots of the blade.

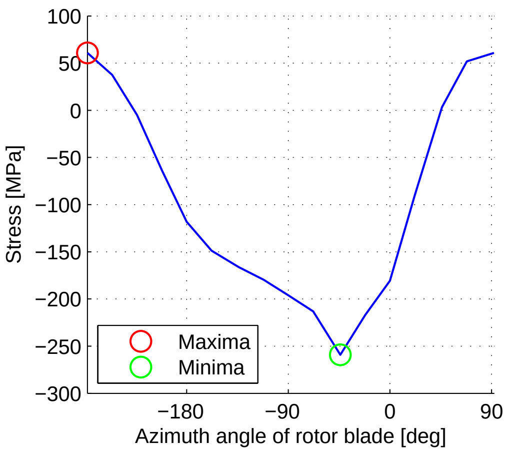

(a) Cyclic stress in a blade element; 16 evaluation points ($D_{MR} = 0.92$).

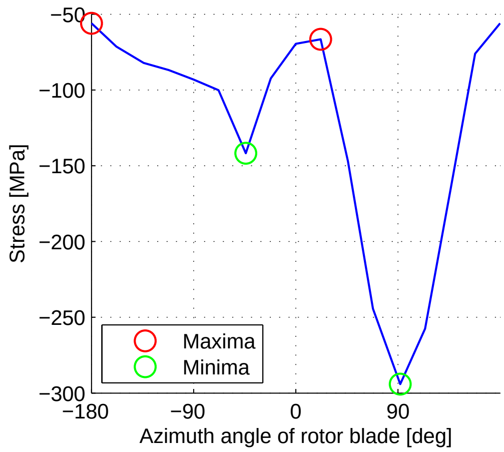

(b) Cyclic stress in a strut element; 16 evaluation points ($D_{MR} = 0.59$).

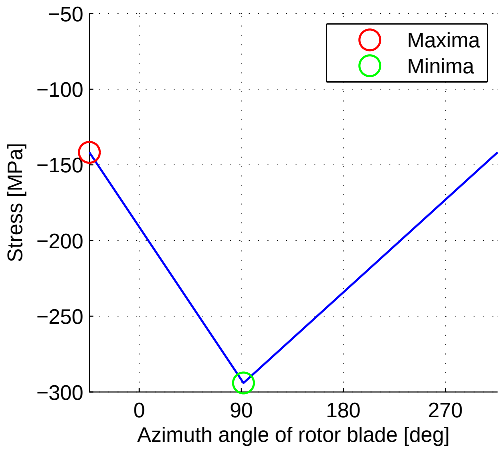

(c) Cyclic stress in same strut element; 2 evaluation points ($D_{MR} = 0.10$).

Figure 5.21: Stress cycles identified by the fatigue analysis of the H-rotor.

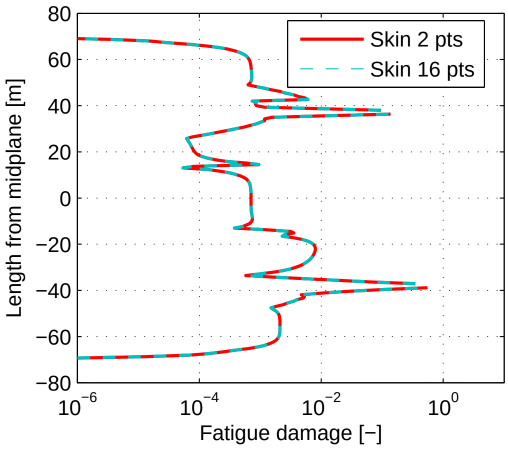

(a) Fatigue damage girder.

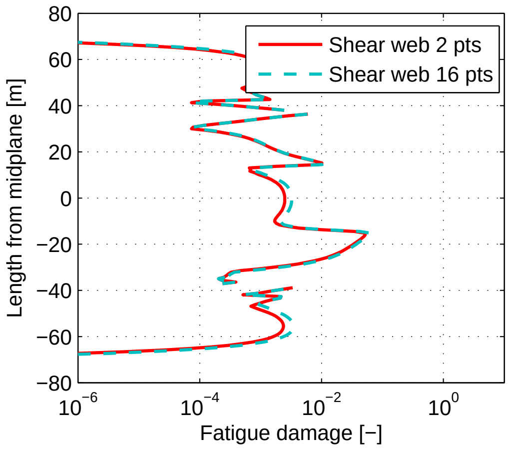

(b) Fatigue damage shear web.

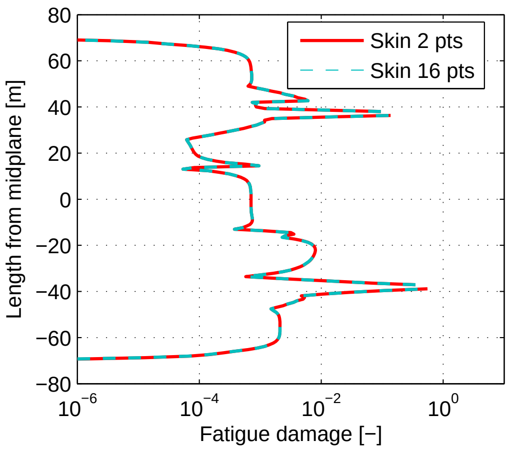

(c) Fatigue damage skin.

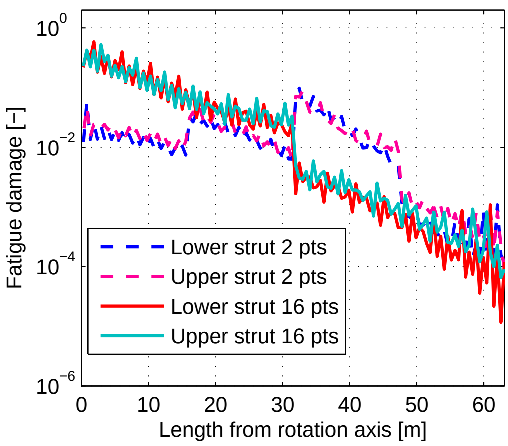

(d) Fatigue damage strut.

Figure 5.22: Comparison between the optimization and extended fatigue analysis of the H-rotor.

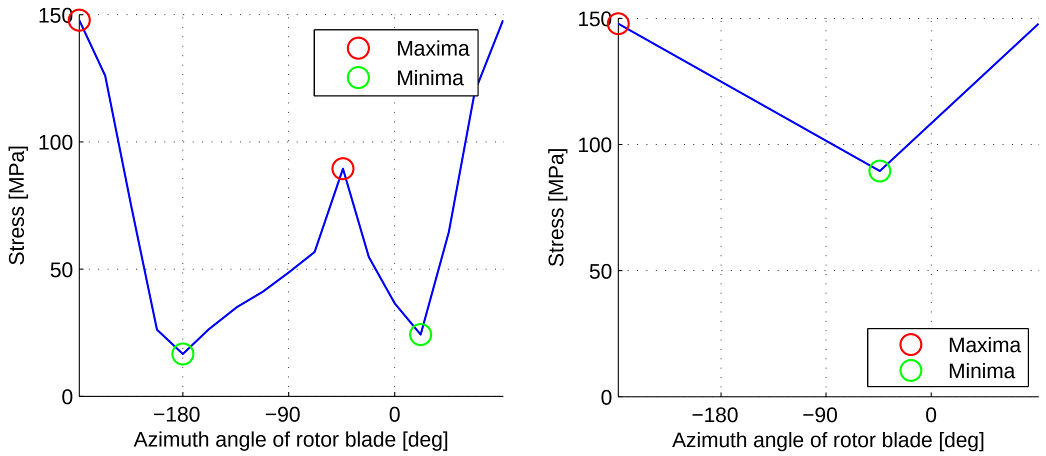

(a) Cyclic stress in a blade element; 16 evaluation points ($D_{MR} = 9.58$).

(b) Cyclic stress in same blade element; 2 evaluation points ($D_{MR} = 0.35$).

Figure 5.23: Stress cycles identified by the fatigue analysis of the Darrieus rotor.

5.4.4 Braking of the rotor

The effect of braking the rotor on the ultimate strength and buckling of the rotor structure is analyzed. Braking times of 1 to 30 seconds are considered. From the braking time, the constant angular deceleration required to bring the rotor to a standstill is determined. It is assumed this deceleration is applied to the structure from the normal operation rotational speed until standstill. Therefore, the considered conditions are the normal operation conditions, downwind position and (almost) parked conditions. The results are shown in Figure 5.25 and Figure 5.26 for respectively the H-rotor and the Darrieus rotor. The minimum braking time of the Darrieus rotor is around 8 seconds. Below 8 seconds the failure index of buckling in parked conditions is higher than 1 and indicates failure. In Figure 5.25, the line for the failure index of buckling in parked conditions shows a jump between 17.5 and 20 seconds braking time. Because of this jump, the minimum braking time of the H-rotor is difficult to judge. Notice that pre-stiffening is used to determine the eigenvalue of the first buckling mode.

5.4.5 Decomposition of the internal rotor loads

In Figure 5.27, Figure 5.28, and Figure 5.29; the internal bending moments and deflection of the structures are shown for respectively the H-rotor blade, the H-rotor strut, and the Darrieus rotor blade. The bending moment and the deflection are decomposed to quantify the contribution of the centrifugal, aerodynamic, and gravitational load to the total.

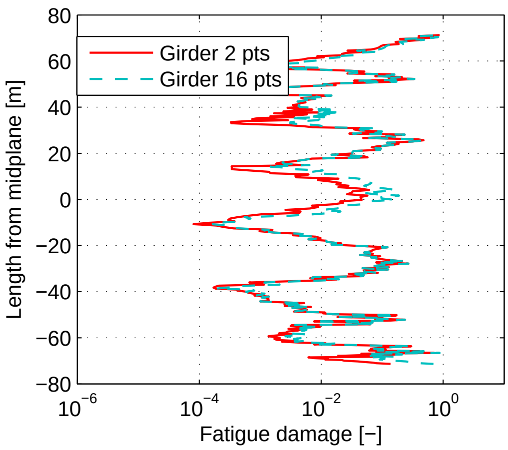

(a) Fatigue damage girder.

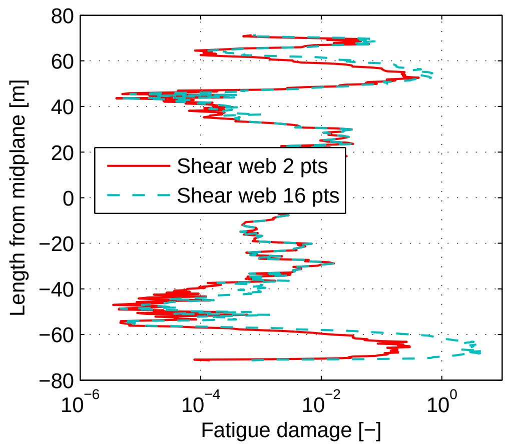

(b) Fatigue damage shear web.

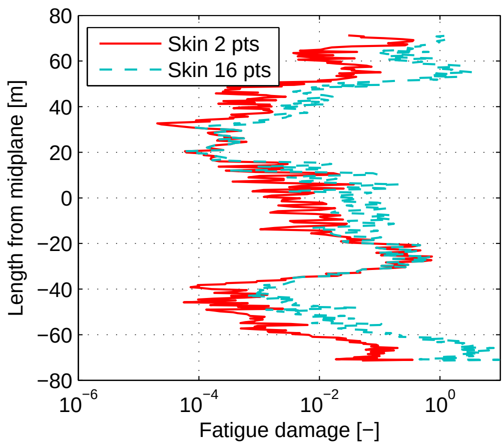

(c) Fatigue damage skin.

Figure 5.24: Comparison between the optimization and extended fatigue analysis of the Darrieus rotor.

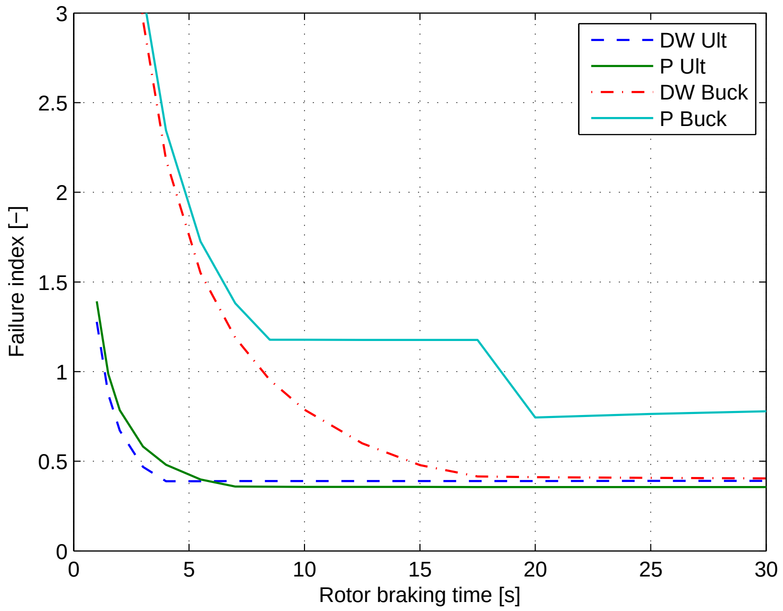

Figure 5.25: Effect of braking on the failure index of the H-rotor.

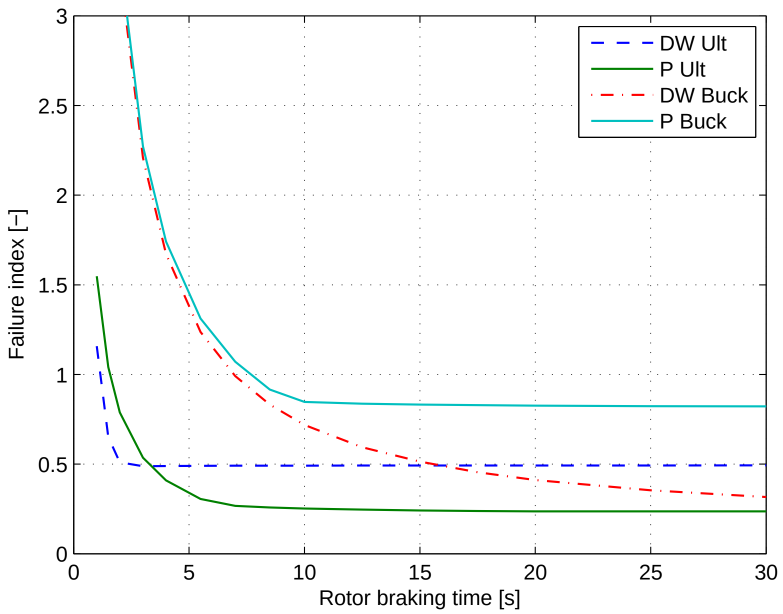

Figure 5.26: Effect of braking on the failure index of the Darrieus rotor.

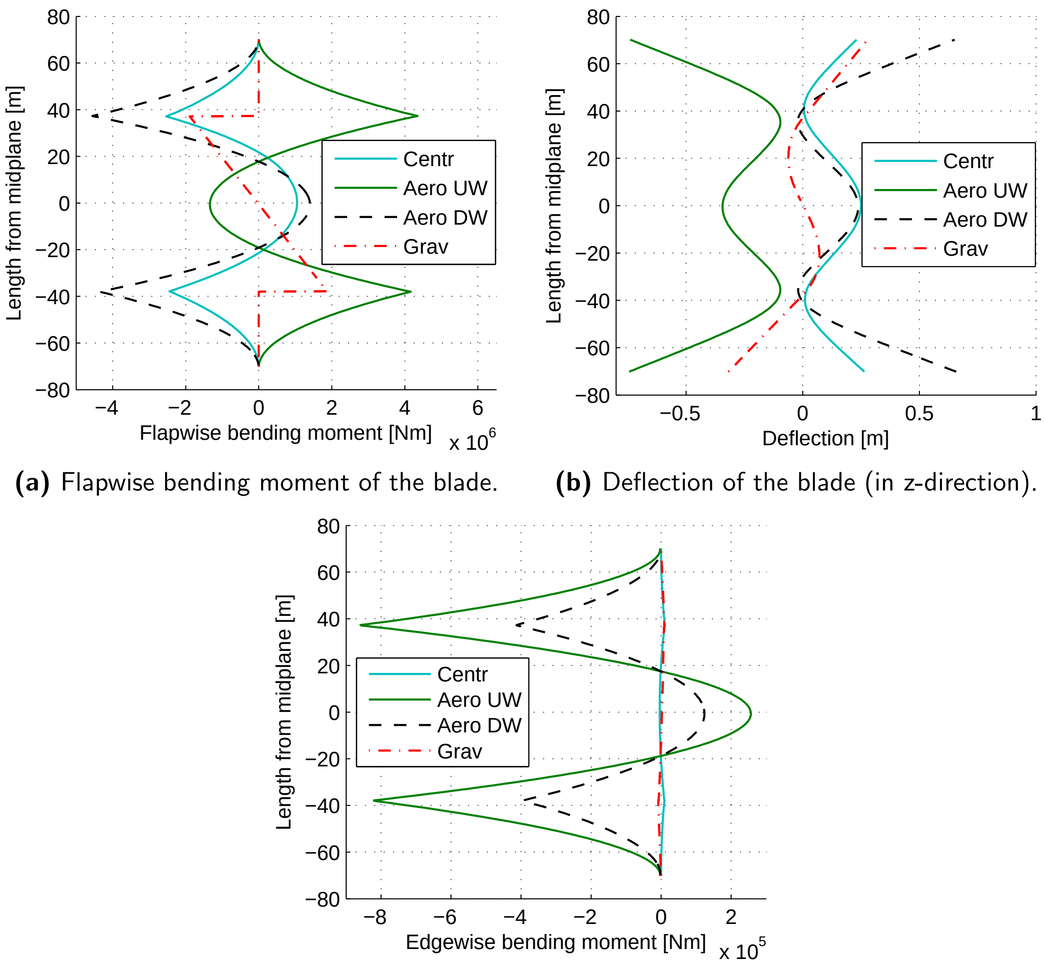

(a) Flapwise bending moment of the blade. **(b)** Deflection of the blade (in z-direction). **(c)** Edgewise bending moment of the blade.

Figure 5.27: Decomposition of the internal loads of the H-rotor blade.

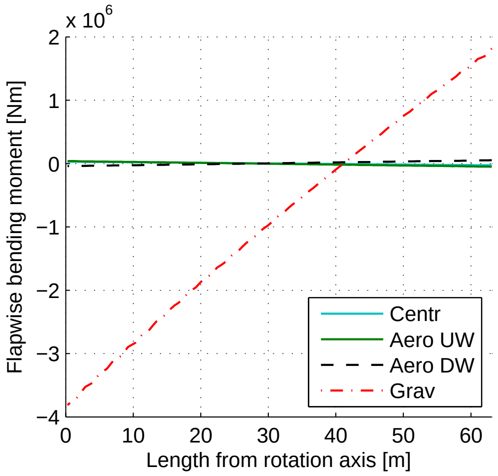

(a) Flapwise bending moment of the lower strut.

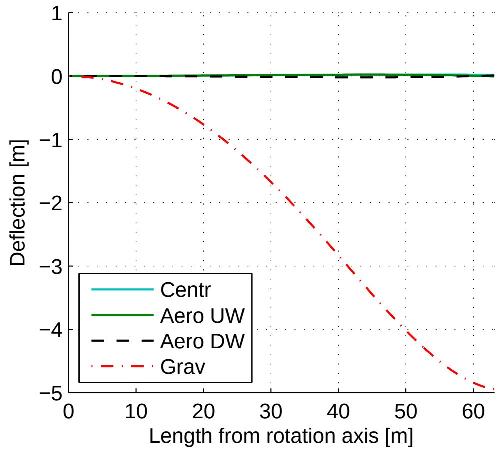

(b) Deflection of the lower strut (in x-direction).

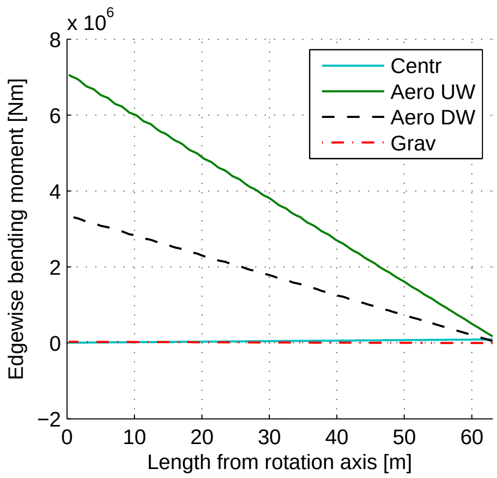

(c) Edgewise bending moment of the lower strut.

Figure 5.28: Decomposition of the internal loads of the (lower) H-rotor strut.

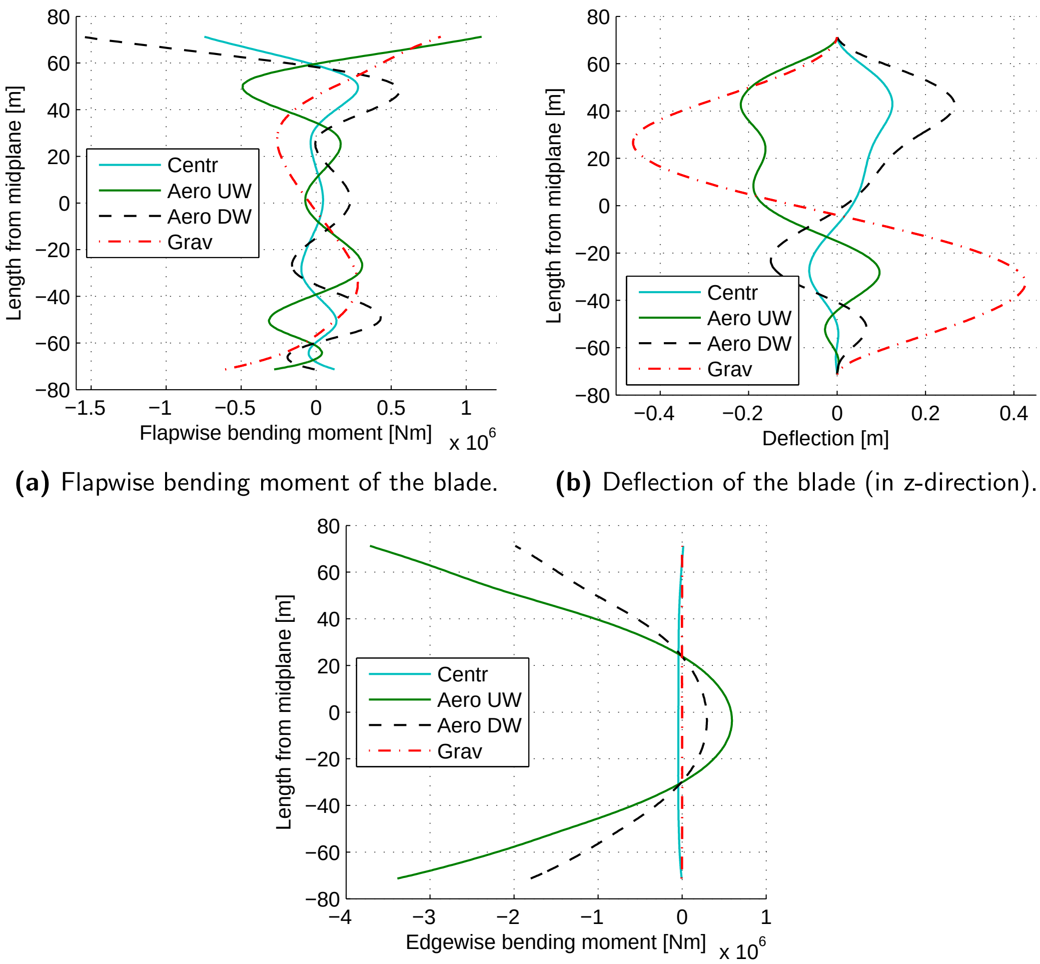

(a) Flapwise bending moment of the blade.

(b) Deflection of the blade (in z-direction).

(c) Edgewise bending moment of the blade.

Figure 5.29: Decomposition of the internal loads of the Darrieus rotor.

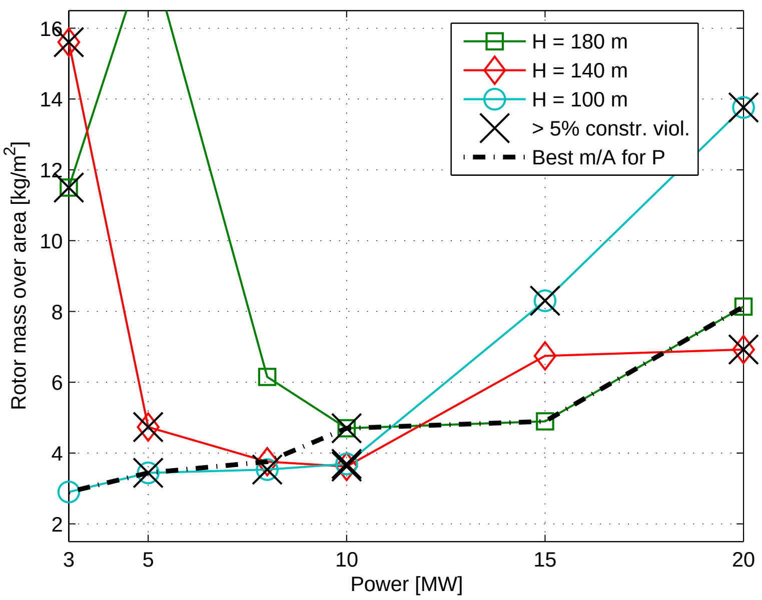

Figure 5.30: Optimization objective versus power for the evaluated points of the H-rotor.

5.5 Scaling trends

Scaling trends are identified for the VAWT rotor to analyze how the size influences the design of the rotor. First of all multiple optimizations are performed to generate data points to which a curve can be fitted. The values of the optimization objective are plotted against the power capacity in Figure 5.30 and Figure 5.32. The optimized points which yield a constraint violation of more than 5% are marked with a cross. The evaluation points minimizing the objective function for the power capacity are connected by the dashed line. (The points which violate the constraints are disregarded. If all the points violate the constraints for a certain size, then the point with minimum constraint violation is selected.) The dashed line illustrates the lower boundary of the optimization objective. In Figure 5.31 and Figure 5.33, the optimization objective is plotted against the diameter-to-height ratio.

Scaling laws for HAWT's are often formulated as function of the rotor diameter, as discussed in Chapter 2.3. For HAWT's the power capacity of the turbine is highly dependent on the rotor diameter. For VAWT's the power capacity of the turbine is, next to the rotor diameter, also highly dependent on the rotor height. Therefore, there is opted for formulating the trends as a function of the power capacity P. Scaling trends are constructed of rotor design parameters, internal loads, and masses. The loading and mass scaling trends are constructed using a power curve fit: aP^b, in which a is the curve coefficient and b is the curve exponent.

The rotors corresponding to the lower boundaries of the optimization objective versus the power capacity (dashed lines in Figure 5.30 and Figure 5.32) are used to construct scaling trends. These rotor designs deviate from the best design solutions, since they are, amongst others, not optimized for rotor height. Therefore, observation based on the trends should be interpreted with care.

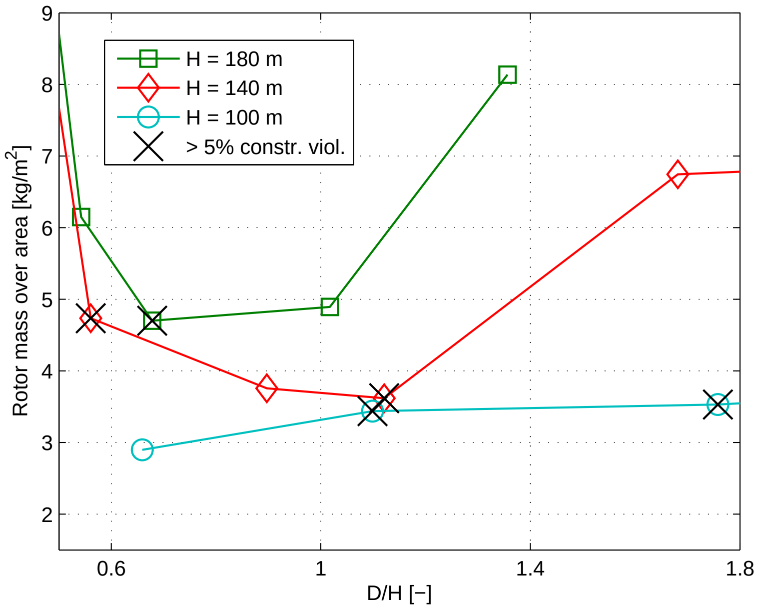

Figure 5.31: Optimization objective versus diameter-to-height ratio for the evaluated points of the H-rotor.

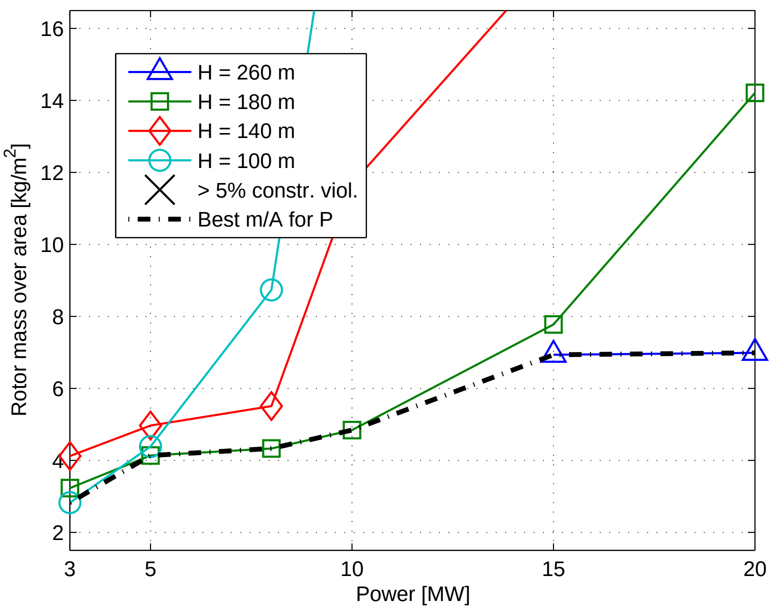

Figure 5.32: Optimization objective versus power for the evaluated points of the Darrieus rotor.

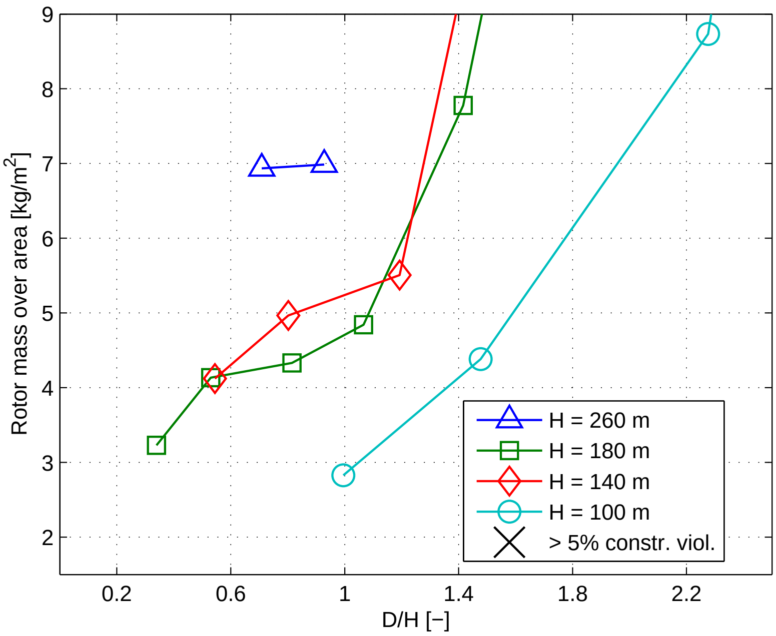

Figure 5.33: Optimization objective versus diameter-to-height ratio for the evaluated points of the Darrieus rotor.

5.5.1 Design scaling trends

In Figure 5.34, the optimum diameter-to-height ratio scaling trend for the H-rotor is illustrated by the dashed line. The optimum diameter-to-height ratio seems to fluctuate around 1. In Figure 5.35, the optimum diameter-to-height ratio scaling trend for the Darrieus rotor is illustrated by the dashed line. The evaluated rotors with a relatively low diameter-to-height ratio appear to be the optimum rotor designs.

In Figure 5.36, the scaling trend is shown of the normalized location of the H-rotor struts. The negative lines show the lower strut location, the positive lines show the upper strut location. In Figure 5.37, the scaling trend is shown of the normalized location of the maximum radius of the Darrieus rotor blade. In the latter figures, a normalized location of -0.5 indicates the bottom of the rotor, a value of 0.5 indicates the top of the rotor.

Figure 5.38 and Figure 5.39 show the failure index scaling trends for respectively the H-rotor and the Darrieus rotor. For both rotor configurations, all the failure indices stay roughly constant for the power capacity.

5.5.2 Loading scaling trends

In Figure 5.40, the scaling trends of maximum flapwise bending moment in normal operation, downwind blade position are shown. The bending moment in the H-rotor blade appears to be near linear for the power. The curve exponent of the Darrieus rotor is 1.74. Despite the higher curve exponent, the bending moment in the Darrieus rotor blade stays smaller than the bending moment in the H-rotor blade in the analyzed domain of the rotor power capacity.

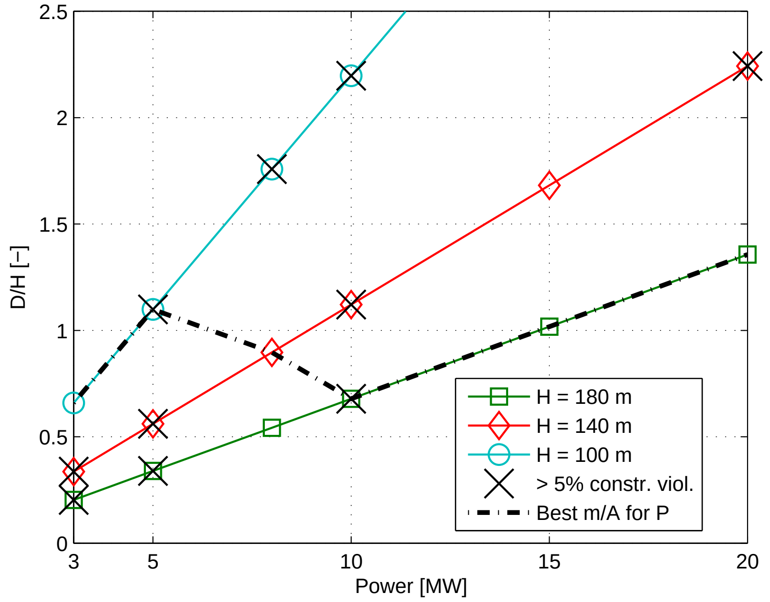

Figure 5.34: Diameter-to-height ratio versus power for the evaluated points of the H-rotor.

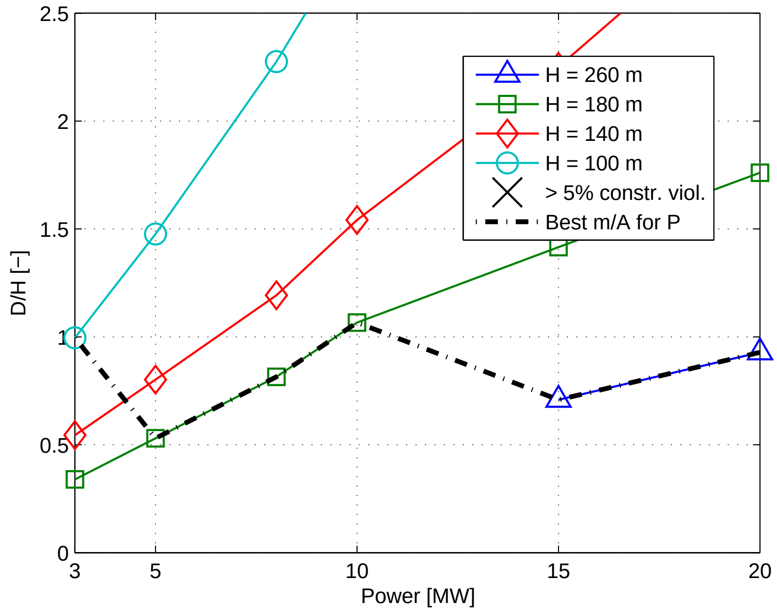

Figure 5.35: Diameter-to-height ratio versus power for the evaluated points of the Darrieus rotor.

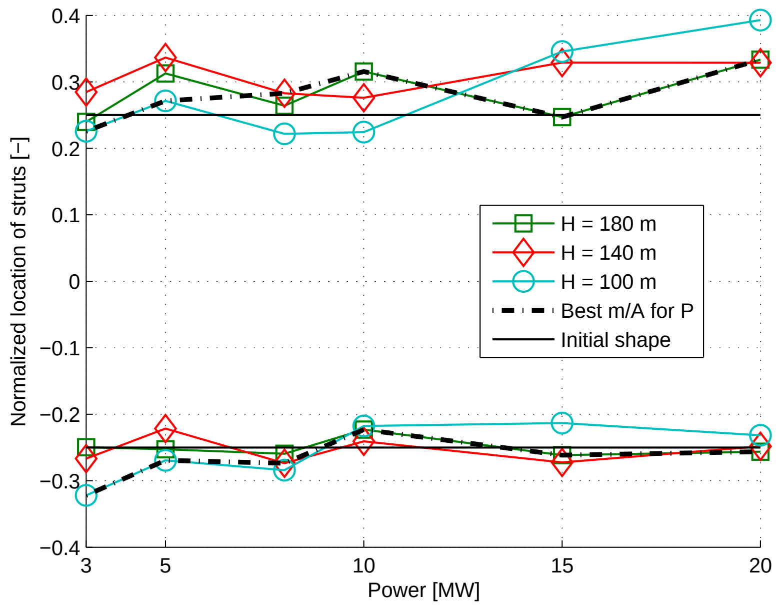

Figure 5.36: Strut locations versus power for the evaluated points of the H-rotor.

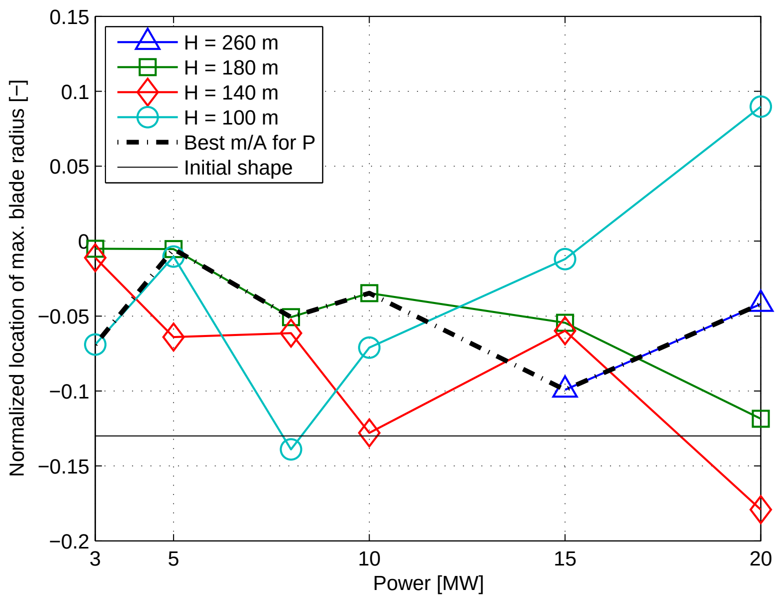

Figure 5.37: Location of maximum blade radius versus power for the evaluated points of the Darrieus rotor.

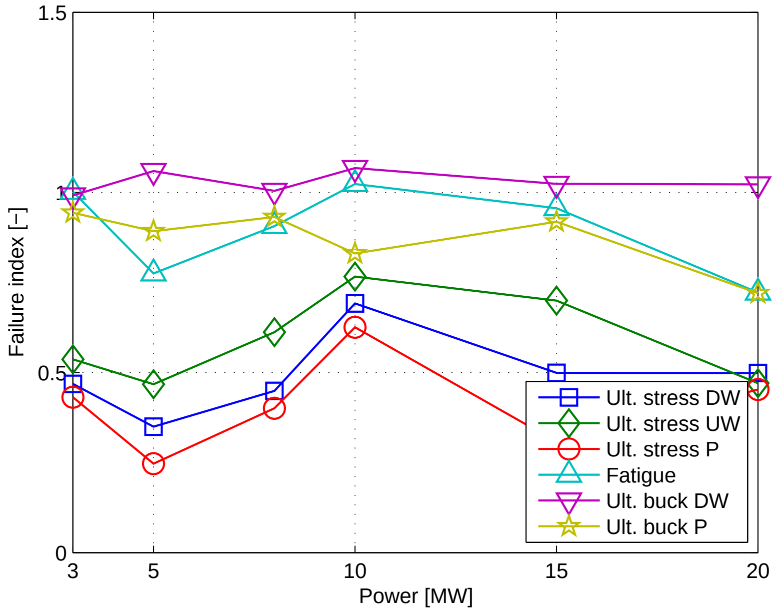

Figure 5.38: Maximum failure index scaling trends for the H-rotor.

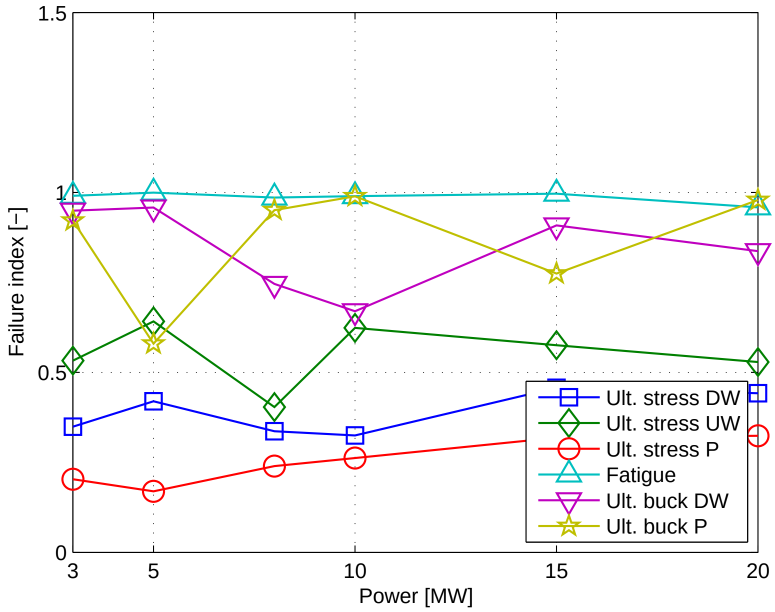

Figure 5.39: Maximum failure index scaling trends for the Darrieus rotor.

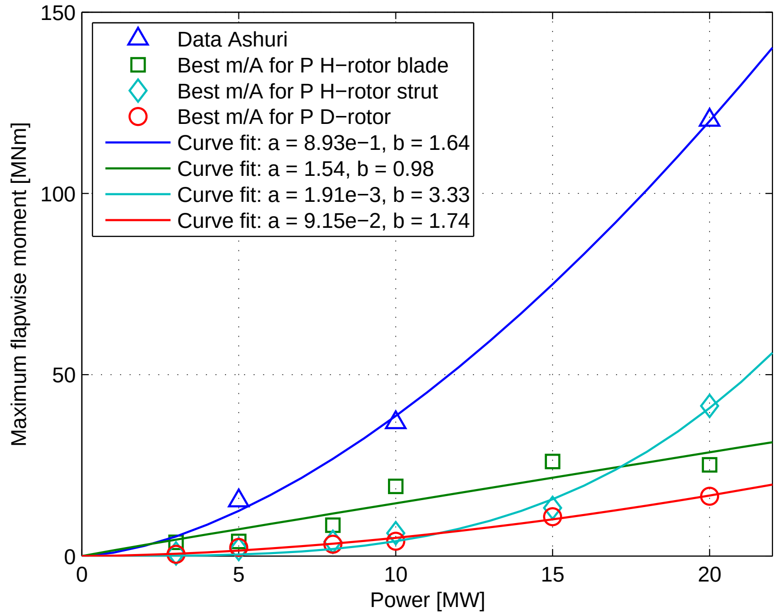

Figure 5.40: Maximum flapwise bending moment scaling trends.

In Figure 5.41, the scaling trends of maximum edgewise bending moment in normal operation, upwind blade position are shown. The edgewise bending moment in the H-rotor blade is relatively low. The scaling trend for the Darrieus rotor blade appears to be in the neighborhood of the scaling trend for the strut of the H-rotor. The curve exponent of the scaling trend for the strut is larger, therefore the edgewise bending moment in the strut is larger for higher power capacities.

Figure 5.42 shows the scaling trends of the maximum difference in flapwise bending moment in normal operation between the downwind and upwind blade position. The difference in flapwise bending moment is relatively low for the H-rotor strut. The blade of the H-rotor shows a near linear scaling trend. The scaling trend for the Darrieus rotor blade starts below that for the H-rotor blade. Despite of its higher curve exponent, the trend of the Darrieus rotor blade does not cross the trend for the H-rotor blade in the analyzed domain of the rotor power capacity.

5.5.3 Mass scaling trends

Figure 5.43 shows that the total mass of the Darrieus rotor is larger than the total mass of the H-rotor up to approximately 17 MW. The curve exponents of the mass scaling trends are 1.95 and 1.40 for respectively the H-rotor and the Darrieus rotor.

Figure 5.44 shows how fast the masses of the individual structural members of the H-rotor grow with respect to each other. The scaling trends for the structural members of the blade roughly have the same curve exponent.

Figure 5.44 shows how fast the masses of the individual structural members of the Darrieus rotor grow with respect to each other. No large differences exist in the curve exponent of the girders and skin mass scaling trends. The curve exponent of the shear web mass scaling

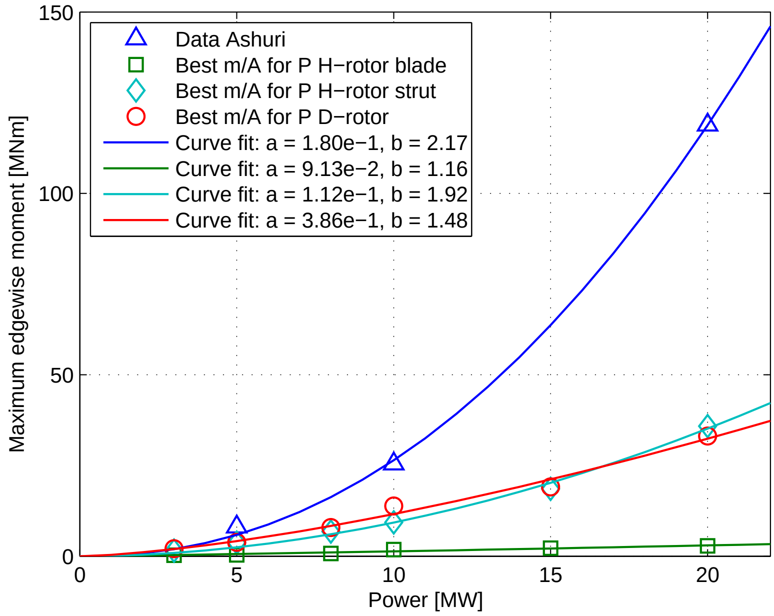

Figure 5.41: Maximum edgewise bending moment scaling trends.

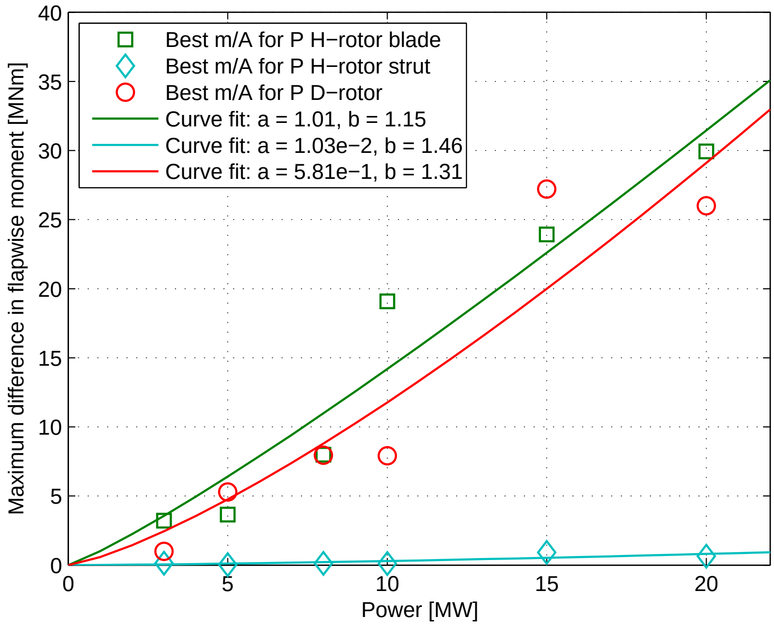

Figure 5.42: Maximum difference in flapwise bending moment scaling trends.

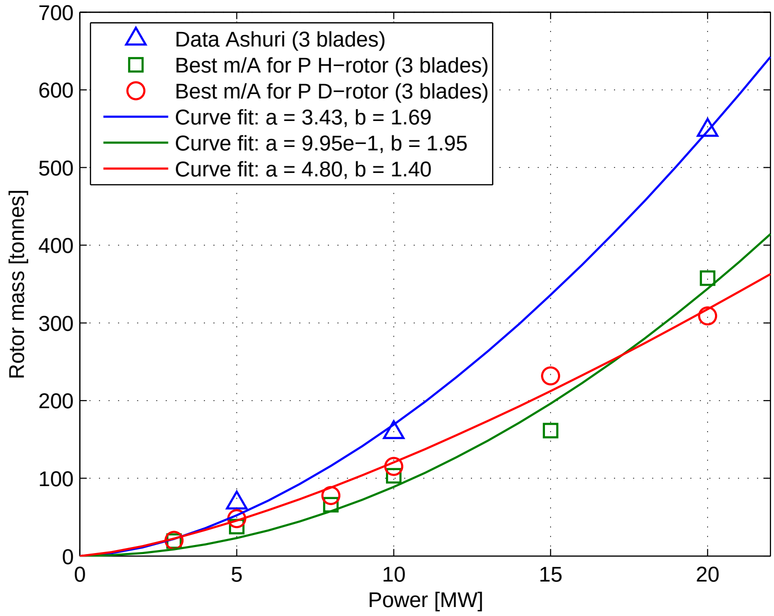

Figure 5.43: Scaling trends of the mass of the rotor blades and struts.

trend is significantly larger. Despite the large curve exponent, the shear web remains the lightest structural member for the analyzed domain of the rotor power capacity.

5.6 Scaling trends for the rotor of a horizontal axis wind turbine

In the work of Ashuri [16]; 5, 10, and 20 MW HAWT's are optimized to minimize the cost of energy. The results are used to construct scaling laws for a modern offshore HAWT. The trends for the HAWT fiberglass rotor blades are used to compare with the developed trends for the VAWT blades and struts. First of all, Ashuri presents the blade flapwise and edgewise moment trends, being respectively $M_{\text{fw}} = 0.0441 \cdot D^{2.62}$ and $M_{\text{ew}} = 0.0005 \cdot D^{3.41}$. Data points are extracted from these trends. The data points are used to construct new scaling trends as function of the power capacity. The trends of the blade flapwise and edgewise moment are illustrated in Figure 5.40 and Figure 5.41.

Ashuri also presents the optimized, total masses of the fiberglass rotor blades for the 5, 10, and 20 MW HAWT's; and the corresponding scaling trend: $m_{\text{blade}} = 0.0571 \cdot D^{2.64}$. A new scaling trend is constructed from the data points as function of the power capacity. The resulting trend is illustrated in Figure 5.43.

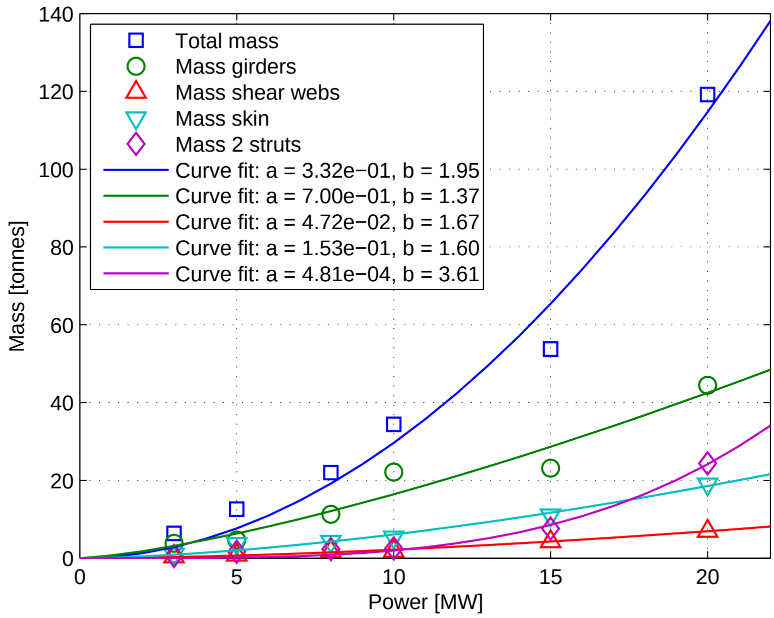

Figure 5.44: Scaling trends of the masses of the individual structural members of the H-rotor.

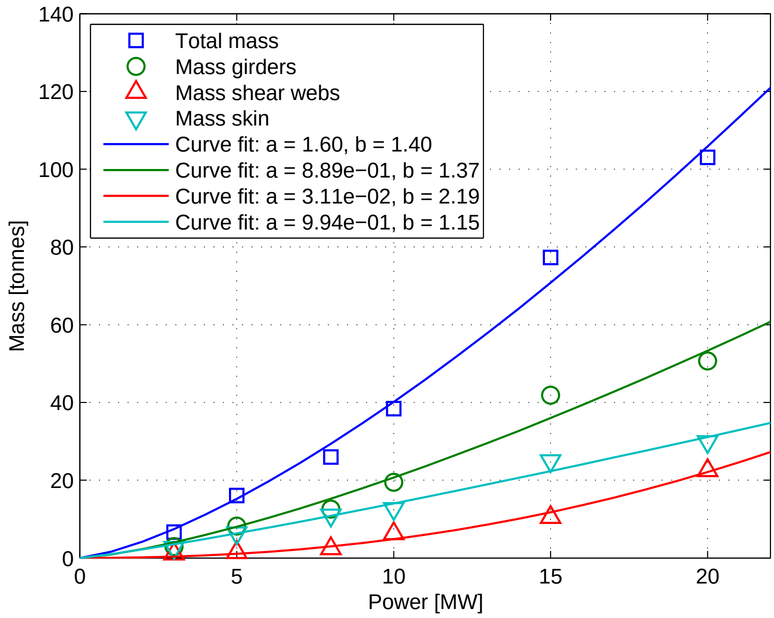

Figure 5.45: Scaling trends of the masses of the individual structural members of the Darrieus rotor.

Chapter 6

Discussion of the optimization results

This chapter discusses the results presented in the previous chapter. First, the performance of the optimization is reviewed. Subsequently, the critical failure modes, design-driving loads, and optimum H-rotor and Darrieus rotor shapes are identified. The chapter is concluded with a comparison between VAWT and HAWT scaling trends.

6.1 Performance of the optimization

Different optimization approaches are applied to the rotor optimization. The approaches are reviewed based on their performance. The section is concluded with a review of the performance of the gradient-based optimization algorithm in the optimization.

6.1.1 Difference between the single section and multiple sections optimization

The multiple sections optimization results show large differences between the minimum and maximum thicknesses of the structural members, namely for the girders, skin, and struts. These differences indicate a lot of material can be saved by using a variable laminate thickness along the length of the blade and struts. This conclusion is confirmed by the difference in the objective function of the single section and multiple sections optimization.

In general, it is expected that an optimum design is found in the proximity of multiple constraint boundaries of different load cases. A value close to, or larger than 1 for the failure index indicates an active constraint. For the multiple sections optimization, more load cases have a failure index close to 1 than for the single section optimization (with exception of the combined optimization of the Darrieus rotor). This indicates better design solutions are found for the multiple sections optimization. Also this conclusion is confirmed by the difference in the objective function of the single section and multiple sections optimization.

6.1.2 Difference between the sizing, shape, and combined optimization

One way of optimizing both the sizing and shape parameters is by sequentially performing separate sizing and shape optimizations, using the result of the prior optimization as the starting point of the new optimization. Another way is optimizing the sizing and shape variables at the same time, earlier defined as combined optimization. These two approaches are compared for the single section optimization. Only a single iteration of the sequential optimization is evaluated.

The sizing optimization yields a reduction of the objective function of 32% and 12% for respectively the H-rotor and Darrieus rotor. The optimized laminate thicknesses are fed to the shape optimization.

The shape optimization of the H-rotor stops virtually at the same point as the starting point and does not improve the objective function, because no reduction of the objective function is possible for the H-rotor. Both the mass of the rotor and the projected rotor area are linear functions of the rotor radius. Notice that the blade chord increases equally with the rotor radius, because the rotor solidity is kept constant in the optimization. In contrast, the shape optimization of the Darrieus rotor reduces the objective function significantly. The radius of the rotor is reduced by 16%, while the projected rotor area is reduced by only 9%. The loss in projected rotor area is limited due to the relatively full shape of the rotor. A 19% mass reduction of the blade is achieved mainly by reducing the chord of the blade.

The combined optimization yields relatively small values for the objective function. For the H-rotor, the radius is increased by 2%. For the Darrieus rotor, the radius is increased by 5%. Similar to the shape optimization, the shapes tend to be symmetric with respect to the midplane.

The resulting values for the objective function of both optimization approaches are summarized in Table 6.1. Notice that the optimization approaches use different starting points. The combined optimizations yield 15% and 54% lower objective functions for respectively the H-rotor and Darrieus rotor. The resulting Darrieus rotor shapes of the sequential and combined optimization head into different directions. It is believed that the sequential optimization requires numerous iterations to realize the same reduction of the objective function as the combined optimization. Therefore, the relative computational cost of the sequential optimization is believed to be high.

Table 6.1: Comparison of the objective functions obtained by different optimization approaches.

Configuration	Optimization approach	Optimized objective [-]	
H-rotor	sequential sizing-shape	5.00	100%
	combined	4.27	-15%
D-rotor	sequential sizing-shape	7.11	100%
	combined	3.28	-54%

6.1.3 Performance of the gradient-based optimization algorithm

In the shape optimization of the H-rotor, the effect of the rotor radius on the objective function and the constraints is evaluated. When zooming in on the constraints at the region near the original rotor radius, it is observed that the values for the failure indices make sudden jumps, see Figure 5.12b. The optimization constraints are based on the failure indices and will also show these sudden jumps. The jumps are believed to be caused by the discretization of the model. The sensitivity analysis performed by the optimization at each evaluation point is likely to experience noise in the constraint functions, which leads to misjudgments of the gradients.

The optimizations are not expected to converge to the global minimum of the design problem. However, some get stuck prematurely when arriving at the boundary of a single constraint, yielding a high value for the objective function with respect to the global minimum. Other optimizations yield a high constraint violation at the point of convergence. The formulation of the constraints can have a significant effect on the outcome of the optimization.

Practical convergence times of the optimization of approximately 1 day to 2 weeks are common, despite the use of parallel computing (8 processors) by the optimization functions in Matlab.

6.2 Discussion of the loads, failure modes, and materials

Based on the post optimization analysis of the previous chapter, the structural analysis performed in the optimization is reviewed. Next, the critical failure modes and the design-driving loads are identified. This section is concluded with a brief discussion of the laminate layups.

6.2.1 Assessment of the considered load cases and mesh densities

From the resonance analysis, it can be concluded that resonance of the multiple sections, combined optimized rotors is likely to occur at the rated wind speed. Further analysis is required to assess the strength of the resonance. If the analysis shows the modes are excited by the harmonic frequency, then modification of the rotor designs is required. The rotor speeds, at which resonance occurs, can be avoided with the use of a controller. In this case, the critical rotor speed corresponds to the rotor speed at the rated wind speed. Avoiding this rotor speed is not considered an option, since at the rated wind speed the rotor would need to operate at a different tip speed ratio than its design tip speed ratio.

The buckling analysis shows poor convergence of the buckling eigenvalues. A higher mesh density is required for a reliable buckling analysis. Furthermore, the buckling analysis shows pre-stiffening of the structure in MSC Nastran is required for a reliable buckling analysis.

The extended fatigue analysis shows an increase in fatigue damage at the inboard section of the rotors (the root of the strut and blade for respectively the H-rotor and Darrieus rotor). The extended fatigue analysis accounts for torque ripple, in contrast to the fatigue analysis performed during the optimizations. The torque ripple is caused by the the tangential aerodynamic force. The tangential aerodynamic force has maxima at the upwind and downwind section, and minima at the windward and leeward section of the blade rotation, shown in Figure 3.10. To take the effect of the torque ripple into account in the fatigue analysis, a minimum of four blade positions need to be evaluated. These blade positions should correspond to the maxima and minima of the tangential aerodynamic force.

In the evaluation of the emergency stop braking time, the failure index of buckling in parked conditions shows a jump between a braking time of 17.5 and 20 seconds, see Figure 5.25. The jump is caused by a change of the first occuring buckling mode. In the optimization, the optimizer did not account for reasonable braking times of the rotor. The optimizer could indirectly account for braking of the rotor by changing the maximum allowable failure index to a value lower than 1.

6.2.2 Identification of the design-driving loads

In chapter 5.4.5, the internal loads of the blade and struts are decomposed in the centrifugal, aerodynamic (UW & DW), and gravitational loads. The internal loads are obtained by a linear analysis. The resulting load of any combination of these loads can be obtained by superposition. In the parked condition only the gravitational load is active. In the normal operation condition the centrifugal, aerodynamic, and gravitational loads are all active. This section identifies the driving loads in the normal operation condition.

For the strut of the H-rotor, the flapwise bending moment and deflection are clearly driven by the gravitational load. The bending moment at the strut tip is introduced in the blade. In the blade, the aerodynamic loads are the largest contributors to the flapwise bending moment and deflection. In the blade of the Darrieus rotor, the gravitational load is the largest contributor to the blade deflection. At the upper end of the blade, the flapwise bending moment due to the gravitational load and the centrifugal load roughly cancel each other out. The total flapwise bending moment at this position is roughly equal to the aerodynamic contribution, which has the largest absolute contribution of the three loads. At the lower end of the blade, the gravitational load is the largest contributor to the flapwise bending moment.

For the blade and strut of the H-rotor, the aerodynamic loads are the only contributors to the edgewise bending moment. In the strut, their contribution goes to zero towards the tip, therefore no moment is introduced in the blade. Also for the Darrieus rotor the aerodynamic loads are the only contributors to the edgewise bending moment.

The centrifugal and gravitational loads are not dependent on the blade position. Therefore, they do not contribute to the difference in flapwise bending moment between the up- and downwind position.

6.2.3 Major fatigue-causing and buckling-causing loads

The scaling trends of the failure indices show that fatigue and buckling (DW & P) are the critical failure modes. No clear effect of the rotor size on the failure indices is observed.

In the fatigue analysis of the optimization, the amplitude of the stress cycle does not depend on the centrifugal and gravitational loads. The stress variation is only caused by the changing aerodynamic load. Notice that the centrifugal and gravitational loads affect the fatigue analysis by their contribution to the mean stress of the stress cycle.

In the Darrieus rotor blade, at the outboard section of the rotor, the contributions of all the loads fluctuate around zero. At this location, the flexibility of the shape of the blade allows minimizing the flapwise bending moment. The maximum flapwise bending moment is found at the blade roots. It is the function of the girders to carry this flapwise bending moment. The flapwise bending moment is believed to be the major buckling-causing load in the Darrieus rotor, since the structure is most likely to buckle first in the girders at the blade roots, see Figure 5.6c.

In the H-rotor blade, buckling is likely to occur fist at the strut connections. The maximum flapwise bending moment is found at the location of the strut connection. Therefore, the flapwise bending moment is identified as the major buckling-causing load in the H-rotor blade. In the strut, both the flapwise and the edgewise bending moment are likely to cause buckling. The shape of the cross-section controls which bending moment causes buckling first.

The optimization does not take into account that buckling can be relatively easy prevented by local reinforcement near the root for the Darrieus rotor and near the strut connection for the H-rotor. Accounting for local reinforcement in the optimization could further reduce the mass of the rotors.

6.2.4 Discussion of the laminate layups

From Figure 5.11, it can be observed that the girders at the outboard section of the sizing optimized Darrieus rotor blade have the highest fatigue damage in transverse direction of the laminate. The laminate of the girders is tailored to primarily carry axial loads, therefore the fatigue strength in the transverse direction may be insufficient. Figure 5.6b shows a high fatigue damage occurs at the (lower) outboard section. Applying a laminate with a better transverse strength may allow further optimization of the blade.

6.3 Optimum rotor shapes

The separate shape optimization is believed to be trivial for judging the optimum rotor shapes, since its rotor shapes head into different directions with respect to the combined optimization. The optimum rotor shapes are identified based on the combined optimization.

6.3.1 Optimum rotor size

In Figure 5.30, the lines for the 140 and 180 meter tall H-rotor seem to be convex (disregarding the 3 MW point for the 180 meter tall H-rotor, since it has a large constraint violation). For these rotor heights, the minima of the objective function are believed to lie in the analyzed domain of the rotor power capacity.

In Figure 5.32, none of the lines corresponding to the rotor heights show a minimum. It is believed that for the 100, 140, and 180 m tall rotors a minimum of the objective function can be found below 3 MW. Taller rotors should be evaluated more extensively to identify optimum rotor designs in the analyzed domain of the rotor power capacity.

The optimum rotor size minimizes the optimization objective function. For both the H-rotor and Darrieus rotor, the lower boundary of the optimization objective versus the power capacity (dashed lines in Figure 5.30 and Figure 5.32) shows a positive slope in the analyzed domain of the rotor power capacity. Therefore, the optimum rotor size lies outside the analyzed domain. The positive slope implies the optimum rotor size can be found below 3 MW.

6.3.2 Optimum diameter-to-height ratio

The optimum diameter-to-height ratio minimizes the optimization objective function. In Figure 5.31 and Figure 5.33, the objective function versus the diameter-to-height ratio is plotted for the H-rotor and Darrieus rotor. The lines in the latter figures correspond to the evaluated rotor heights. For the H-rotor, the lines of the 140 and 180 meter tall rotor seem to be convex. For these rotor heights, the minima of the objective function are believed to lie in the evaluated domain of the diameter-to-height ratio. The 100 meter tall rotor is evaluated for relatively high diameter-to-height ratios. More points need to be evaluated for this rotor height to identify a possible minimum.

Also the lines of the Darrieus rotor need more points to identify a possible minimum. It is believed that the minima of the objective function can be found for lower values of the diameter-to-height ratio. Notice that low diameter-to-height ratios look promising for the Darrieus rotor design on a subsystem level, but may yield poor performance on a system level. For example a decrease in the diameter-to-height ratio increases rotor tower length, which can have an adverse effect on the cost of energy.

In Figure 5.34, the optimum diameter-to-height ratio seems to fluctuate around 1 for the H-rotor. All the evaluated points are displayed to show the restrictions of identifying the optimum rotor designs for the power capacity. Many of the rotor designs show a constraints violation of more than 5%. The designs that do not violate the constraints with more than 5% have a diameter-to-height ratio close to 1.

In Figure 5.35, the optimum diameter-to-height ratio scaling trend for the Darrieus rotor is illustrated by the dashed line. In this case, the evaluated rotors with a relatively low diameter-to-height ratio appear to be the optimum rotor designs. However, data points for lower diameter-to-height ratios are missing (except for the 3 MW design). Therefore, the optimum diameter-to-height ratio of the Darrieus rotor is hard to judge. Notice that only the 15 and 20 MW Darrieus rotors are evaluated for a 260 m rotor height. For these rotor sizes, the additional evaluated rotor height provides more variation in the diameter-to-height ratio of the optimized Darrieus rotors, which can affect the scaling trends of the Darrieus rotor.

6.3.3 Optimum blade curvature of Darrieus rotor

The combined optimization of the Darrieus rotors yield near symmetric shapes with respect to the midplane, shown in Figure 5.15. In Figure 5.37, the scaling trend of the maximum blade radius location is shown. A sound, midplane-symmetric Darrieus rotor design would yield a value of zero for the maximum blade radius location (maximum radius is located at the midplane). The trend shows the location of maximum blade radius tends to move upwards relative to its initial location. All the maximum radius locations are negative, with the exception of 1 point. No clear effect of the size of the rotor on the maximum radius locations is observed.

6.3.4 Optimum strut location of H-rotor

The resulting H-rotors of the combined optimization show small variations in the strut positions, see Figure 5.14. In Figure 5.36, the strut location scaling trend shows the upper strut tends to move upwards relative to its initial location. The lower strut stays closer to its initial location. The size of the rotor appears to have no effect on the optimum strut locations.

6.4 Comparison between scaling trends

A relation between the mass of the structural members and the internal loads is sought based on a comparison between the mass and load scaling trends. The discussion of the results is concluded with a comparison of the VAWT and HAWT scaling trends.

6.4.1 Comparison of the mass and load scaling trends

The effect of the rotor size on the mass contribution of the structural members is shown in Figure 5.44 and Figure 5.44.

For the H-rotor, the scaling trends for the structural members of the blade (the girders, shear webs, and skin) roughly have the same curve exponent. Therefore, the fraction of mass contribution of the structural members to the total mass of the blade stays nearly constant for the power capacity. The mass of the struts grows faster than the mass of the structural members of the blade, therefore its mass contribution gets more dominant for an increase in power capacity.

For the Darrieus rotor, no large differences exist in the curve exponent of the girders and skin mass scaling trends. However, the curve exponent of the shear web mass scaling trend is significantly larger. Despite the large curve exponent, the shear web remains the lightest structural member for the analyzed domain of the rotor power capacity.

Figure 5.40, Figure 5.41, and Figure 5.42 show the scaling trends of respectively the flapwise, edgewise, and difference in flapwise bending moment. The curve exponents of the mass scaling trends are compared to those of the load scaling trends. Table 6.2 presents the curve exponents obtained by the scaling trend fits.

The values of the curve exponents of the H-rotor strut mass and flapwise bending moment scaling trends lie close to each other. This implies a linear relation between the mass of the strut and the flapwise bending moment. However, further analysis is required to draw rigid conclusions about the relation between the mass and load scaling trends.

Table 6.2: Comparison of the curve exponents of the mass and load scaling trends fits.

Configu- ration	Structural member	Curve exponent [-] m	M_{fw}	M_{ew}	dM_{fw}
H-rotor	girder	1.37			
	shear web	1.67	0.98	1.16	1.15
	skin	1.60			
	strut	3.61	3.33	1.92	1.46
D-rotor	girder	1.37			
	shear web	2.19	1.74	1.48	1.31
	skin	1.15			

6.4.2 Comparison of the VAWT and HAWT mass scaling trends

The bending moments for the VAWT rotors are a lot smaller than the bending moments for the HAWT rotor. This can be explained by the material choice of the designs. Notice that the VAWT blade and strut designs use carbon-fiber laminates and the HAWT blade design uses fiberglass laminates.

In Table 6.3 the masses of the HAWT rotors and the optimized VAWT rotors are stated for three power capacities. Furthermore, it states the mass reductions for the VAWT rotors with respect to the HAWT rotors per size. The mass reduction obtained by the H-VAWT appears to decrease for larger rotor size. In contrast to the mass reduction obtained by the Darrieus VAWT, which appears to increase for larger rotor sizes. A 20 MW Darrieus VAWT reduces the rotor mass by 44%. However, the cost of fiberglass is approximately 7 to 10 times cheaper than carbon-fiber. Therefore, the material cost of the HAWT rotor will be significantly smaller. Notice that the material cost of the rotor structure is only a small fraction of the total system cost.

Table 6.3: Optimized rotor masses [tonnes].

Turbine	5 MW		10 MW		20 MW	
HAWT	68.6	100%	159.0	100%	548.3	100%
H-VAWT	37.8	-45%	103.3	-35%	357.6	-35%
Darrieus VAWT	48.1	-30%	115.3	-28%	309.1	-44%

Chapter 7

Conclusion and recommendation

This chapter starts with a critical discussion on the methodology. Next, conclusions are drawn concerning the thesis objective. Subsequently the main conclusions of each chapter are discussed. The report is concluded with recommendations on future work.

7.1 Conclusions

This thesis provides a good comparison between two rotor configurations of Vertical Axis Wind Turbines (VAWT): the H-rotor and Darrieus rotor. Both designs are assessed for the same failure modes and use the same material assumptions and loading conditions. This justifies comparing the optimization results of the different rotor configurations. The rotor geometry representation enables variations within the two rotor configurations; e.g. the H-rotor can be evaluated with a variable number of struts. However, the optimization is computationally expensive; for this reason variations of the two rotor configurations are not explored.

The methodology of this thesis forms a good basis for developing scaling trends for VAWT's. The scaling trend of a rotor is constructed by a power curve fit. The fit uses a limited number of data points, which correspond to the optimized designs. A change of a single data point can have a significant effect on the fitted curve, and thereby the scaling trend. Therefore, it is important to use representative data points, which are obtained by optimization. A representative data point is a good approximation of the global optimum of the optimization problem. Furthermore, a representative data point should correspond to a sound design solution. This requires that the formulation of the optimization problem yields a good representation of the design problem.

For the formulation of the optimization problem, it is possible to use almost every rotor design parameter as variable. In general, expanding the design space yields better design solutions, however this comes at the cost of a more computationally expensive and complex optimization. The formulation of the optimization problem uses some important restrictions and assumptions to confine the design space, which are listed below.

- Restrictions on the blade and strut shape; e.g. airfoil shape and constant chord distribution.
- Imposing a constant tip speed ratio and rotor solidity.
- Applied materials and corresponding material strengths.
- Laminate and sandwich layups.
- Considered loading conditions.
- Considered failure modes and the corresponding criteria.
- Values for the applied safety factor.

The objective of this thesis is to gain knowledge about the influence of the size (power capacity) of the turbine on the structural rotor performance of multi-megawatt VAWT's. Scaling trends are constructed based on optimized VAWT rotor designs for rotor sizes ranging from 3 MW to 20 MW. The optimized designs minimize the ratio of the rotor mass over projected area. The constructed mass scaling trends show the total mass of the Darrieus rotor is larger than the total mass of the H-rotor up to approximately 17 MW. For larger rotor sizes the H-rotor becomes heavier than the Darrieus rotor. Rotor mass reductions for the carbon-fiber 20 MW H-VAWT and Darrieus VAWT of respectively 35% and 44% are obtained with respect to the fiberglass HAWT rotors. Despite this mass reduction, the material cost of the HAWT rotor will be significantly smaller.

The mathematical geometry representation of the rotor offers enough flexibility for the purpose of this thesis. The blade geometry is generated using Non-Uniform Rational Basis Splines (NURBS), requiring a limited number of parameters to initiate a blade design. The flexibility of the NURBS is mainly utilized for defining the blade curvature of the Darrieus rotor blades. The limited required number of parameters enable a confined set of design variables for the optimizations. Furthermore, the NURBS offer easy discretization of the model to generate input for Finite Element Method (FEM) software. For the struts of the rotor a simple, straight tapered beam with rectangular cross-section suffices.

A FEM model of the rotor structure is used to perform the structural analysis, which offers flexibility. A fine mesh is required for an accurate buckling analysis, which results in a long run time. This makes the model less desirable to use in numerical optimization. Furthermore, the FEM analysis leads to misjudgments of the gradients determined by the gradient-based optimization, because of the discretization of the model. The misjudged gradients cause the optimization to get stuck at a local minimum.

A distinction is made between the sizing, shape, and combined optimization. Optimizations are performed using a single section along the blade and struts, and using multiple sections along the blade and struts. For each blade section a laminate thickness is assigned to the girders, shear webs, and skin. Each strut section uses the same laminate thickness along the cross-section. The combined optimizations show that the rotor mass over projected rotor area ratio for the multiple sections optimized H-rotor is approximately 16% smaller compared to the single section optimized H-rotor. The rotor mass over projected rotor area ratio for the multiple sections optimized Darrieus rotor is approximately 5% smaller compared to the single section optimized Darrieus rotor. The combined optimization is thought to be a more efficient optimization approach with respect to sequential sizing-shape optimizations.

The rotor structure is only analyzed for normal operation and parked load conditions. For normal operation load conditions, the structure is analyzed for maximum stress, fatigue, and buckling. For parked load conditions, the structure is analyzed for maximum stress and buckling. A more extensive and additional analysis is performed on the designs resulting from the combined optimizations of the baseline rotors. Analysis of the eigenmodes of the rotor structures shows resonance is likely to occur near the design rotational speeds of the optimized baseline rotors. A buckling analysis is performed for a higher mesh density and using pre-stiffening of the structure. Both pre-stiffening of the rotor structure and a higher mesh density appear to be required for performing an accurate buckling analysis. The extended fatigue analysis shows that evaluating the loads in the structure at two azimuthal positions is not sufficient to judge the fatigue of the structure. From the minimum braking time analysis, it is noticed that the optimizer does not account for a reasonable braking time. Changing the maximum allowable failure index to a value lower than 1 is one way to account for braking of the rotor in the optimization.

In the fatigue analysis of the optimization, the amplitude of the stress cycle does not depend on the centrifugal and gravitational loads. The stress variation is only caused by the changing aerodynamic load. In the Darrieus rotor blade, at the outboard section of the rotor, the flexibility of the shape of the blade allows minimizing the flapwise bending moment. For the Darrieus rotor blade, the maximum flapwise bending moment is found at the blade roots. For the H-rotor blade, the maximum flapwise bending moment is found at the location of the strut connection. At the latter locations buckling is likely to occur first. For both blades, the flapwise bending moment is identified as the major buckling-causing load.

The optimum diameter-to-height ratio can not be adequately judged, because the variety in the evaluated rotor-to-diameter ratios of the optimized designs is too small. The optimizations yield rough approximations of the best design solutions, since the diameter-to-height ratio is driving the structural rotor performance. Therefore, the conclusions based on the mass scaling trends should be interpreted with care.

7.2 Recommendations for future work

As discussed in the beginning of this chapter, it is important to use representative data points to ensure a representative scaling trend. Therefore, the data should ideally correspond to the best design solution for the given rotor size. The recommendations on better approximating the best design solution can be separated in two categories, listed below. A third category provides recommendations on comparing the VAWT and HAWT rotor scale trends.

1. Recommendations on a better formulation of the optimization problem.

   To allow sufficient variation of the diameter-to-height ratio of the rotor, optimizations should be performed with a variable rotor height. The optimizations will yield better design solutions and the optimum diameter-to-height ratio can be better identified. To do so, it may be interesting to use a genetic algorithm for the optimization, and include the optimized designs of this thesis in the initial population. In general, genetic algorithms take more time to converge than gradient-based algorithms. The convergence time of a genetic optimization is dependent on the size of its population. The required population size depends on the number of design variables.

   The optimization should enable a better controlled analysis. The analysis should ignore trivial failure modes, such as local buckling at the strut connections and blade roots. Buckling can be relatively easy prevented by local reinforcement at these locations.

   To gain more control in the optimization, the section division of the blade and strut should be re-evaluated. One way to gain control, is to increase the number of sections, however smarter alternatives exist. For example a non-linear distribution of the section could be considered.

   The power capacity of the rotors is determined using many assumptions. A more detailed aerodynamic model can better determine the power. This allows the addition of design parameters to the design space, which have a significant effect on the power capacity of the rotor. For example, the chord distribution, the tip speed ratio, the solidity, and the airfoils can be varied in the optimizations.

   The laminate layups are predefined. By varying material properties in the optimization, further reduction of the objective function can be achieved. The material properties can be varied by including the laminate layups to the design space.

   The optimization should ideally be performed on system level. Amongst others, the tower and the generator should be included in the optimization. A good optimization objective for a system level optimization is the cost of energy. This would require a representative cost model.

2. Recommendations on better approximating the global optimum.

   The optimization gets stuck regularly at a local minimum. This is thought to be caused by the combination of the gradient-based algorithms and the FEM model. Replacing the FEM model by analytic models is believed to improve convergence of the optimization. Furthermore, the analytic models can reduce the computation time of structural analysis significantly. ESDU could provide helpful, validated design tools.

In general, genetic optimization algorithms take longer to converge to a solution than gradient-based algorithms. Genetic algorithms could be useful for optimizing the shape variables of the rotor. Before evaluating genetic algorithms, it is advised to reduce the design evaluation time of the optimizer.

3. Recommendations on the comparison of VAWT and HAWT rotor scale trends

   It is troublesome to compare the scaling trend for a carbon-fiber VAWT rotor to the scaling trend for a fiberglass HAWT rotor. It is recommended to perform VAWT rotor optimizations using fiberglass laminates, to construct the scaling trend for a fiberglass VAWT rotor. This scaling trend can be used for direct comparison with the HAWT rotor scaling trend. Furthermore, it is interesting to compare the scaling trends for a carbon-fiber and a fiberglass VAWT rotor.

The design problem should be well understood before expanding the design space. Understanding the outcome of the optimization can be complex. For the confined set of design variables in this thesis, identifying the relation of the structural member mass and load scaling trends is proved to be challenging.

References

[1] S. Eriksson, H. Bernhoff, and M. Leijon. Evaluation of Different Turbine Concepts For Wind Power. *Renewable and Sustainable Energy Reviews*, 12:1419–1434, 2008.

[2] I. Paraschivoiu. *Wind Turbine Design: With Emphasis on Darrieus Concept.* École Polytechnique de Montréal, Canada, 2002.

[3] T. D. Ashwill, H. J. Sutherland, and D. E. Berg. A Retrospective of VAWT Technology. Technical Report SAND2012-0304, Sandia National Laboratories, Albuquerque, New Mexico, United States, 2012.

[4] B. Richards and S. Quareshi. The Design, Fabrication and Installation of Project Eole 4 MW Prototype VAWT Generator. In *European Wind Energy Conference and Exhibition '86*, number 1, pages 609–614, Rome, Italy, 1986.

[5] I. D. Mays and C. A. Morgan. The 500 kW VAWT 850 Demonstration Project. In *European Wind Energy Conference and Exhibition '89*, number 2, pages 1049–1053, London, United Kingdom, 1989.

[6] T. J. Price. UK Large-Scale Wind Power Programme from 1970 to 1990: The Carmarthen Bay Experiments and the Musgrove Vertical-Axis Turbines. In *Wind Engineering*, volume 30, pages 225–242, Brentwood, United Kingdom, 2006.

[7] O. Ljungstrom. L-180 Poseidon - A New System Concept in Vertical Axis Wind Turbine Technology. In *Wind Energy Systems '80*, pages 333–355, Copenhagen, Denmark, 1980.

[8] O. Ljungstrom. Some Innovative Concepts in Axial Flow and Cross Flow Wind Turbine Systems. In *European Wind Energy Conference and Exhibition '86*, number 1, pages 657–668, Rome, Italy, 1986.

[9] D. J. Sharpe and D. A. Taylor. The Aerodynamic Performance of the Vee Type Vertical Axis Wind Turbine. In *Wind Energy Conversion '85*, pages 155–159, London, United Kingdom, 1985.

[10] M. Raciti Castelli, A. Dal Monte, M. Quaresimin, and E. Benini. Numerical evaluation of aerodynamic and inertial contributions to Darrieus wind turbine blade deformation. *Renewable Energy*, 51:101–112, 2013.

[11] H. G. Reimerdes. A Vertical Axis Wind Energy Converter With Straight Blades. In *Wind Energy Systems '80*, pages G2–1–G2–20, Copenhagen, Denmark, 1980.

[12] K. J. Touryan, J. H. Strickland, and D. E. Berg. Electric Power From Vertical Axis Wind Turbines. *Journal of Propulsion and Power*, 3:481–493, 1987.

[13] D. E. Berg. Structural design of the Sandia 34-meter VAWT. Technical Report SAND84-1287, Sandia National Laboratories, Albuquerque, New Mexico, United States, 1985.

[14] D. J. Malcolm. High production Darrieus rotors. In *European Wind Energy Conference and Exhibition '86*, number 1, pages 605–608, Rome, Italy, 1986.

[15] P. Joosse. TU Delft Lecture: AE4645 Design and Manufacturing of Wind Turbine Rotor Blades - Structural Design of Wind Turbine Blades, February 2011.

[16] T. Ashuri. *Beyond Classical Upscaling: Integrated Aeroservoelastic Design and Optimization of Large Offshore Wind Turbines*. Ph.D. Thesis, Delft University of Technology, The Netherlands, 2012.

[17] E. A. Ferede, M. M. Abdalla, and G. J. W. Van Bussel. NURBS-based Parametric Modelling of Wind Turbine Blades. In *Proceedings of 9th PhD Seminar on Wind Energy in Europe*, Gotland, Sweden, 2013.

[18] L.A. Piegl and W. Tiller. *The Nurbs Book*. Springer-Verlag GmbH, 1997.

[19] C. Kassapoglou. *Design and Analysis of Composite Structures: With Applications to Aerospace Structures*. Wiley, 2011.

[20] A. Poursartip and P. W. R. Beaumont. The Fatigue Damage Mechanics of a Carbon Fibre Composite Laminate: II Life Prediction. *Composites Science and Technology*, 25:283–299, 1986.

[21] K.E. Arden. Euler Buckling. Technical report, Newport News Shipbuilding.

[22] C. J. Simao Ferreira. *The Near Wake of the VAWT*. Ph.D. Thesis, Delft University of Technology, The Netherlands, 2009.

[23] D.W. Zingg, M. Nemec, and T.H. Pulliam. A Comparative Evaluation of Genetic and Gradient-based Algorithms Applied to Aerodynamic Optimization. *European Journal of Computational Mechanics/Revue Européenne de Mécanique Numérique*, 17(1-2):103–126, 2008.

[24] K.K. Choi and N.H. Kim. *Structural Sensitivity Analysis and Optimization 1: Linear Systems*. Springer, 2005.

[25] R. Nijssen, O. Krause, and T. Philippidis. Benchmark of Lifetime Prediction Methodologies. Technical Report OB-TG1-R012 rev 001, Optimat Blades, 2005.

[26] M.A. Meggiolaro and J.T.P. Castro. Statistical Evaluation of Strain-life Fatigue Crack Initiation Predictions. *International Journal of Fatigue*, 26(5):463–476, 2004.

Appendix A

Fatigue strength of fiberglass and metals

Next to fatigue strength of carbon-fiber laminates (CFRP), the fatigue strength of fiberglass laminates (GFRP) and metals is studied. No optimizations are performed using GFRP's or metals. The data may be useful for further work.

The fatigue life of a GFRP laminate is extensively studied in the Optimat Blades research project on fatigue in GFRP rotor blades. The report of Nijssen et al. [25] discusses multiple methods to define an applied cyclic stress, lifetime curve (S-N curve). A (log-log) linear regression method formulation of the S-N curve is selected. Using the data from WMC for a $[(\pm 45/0)_4/\pm 45]$ laminate and R_σ = -1 results in the expression stated in Equation A.1. Note that σ_{max} in the latter equation is half $\Delta\sigma$ in Equation 3.2 for zero mean stress (R_σ = -1). A simple, linear Goodman constant life diagram is applied to account for non-zero mean stresses, the diagram is illustrated in Figure A.1. An equivalent stress amplitude with zero mean stress can be determined using this diagram for a given cyclic loading (mean stress and stress amplitude combination) and strength of the material. Subsequently this equivalent stress amplitude can be used in the S-N curve for R_σ = -1.

$$\begin{aligned} \sigma_{max} &= 574.5 \cdot N_{all}^{-0.107} \\ N_{all} &= \left(\frac{\sigma_{max}}{574.5}\right)^{-9.39} \end{aligned} \tag{A.1}$$

A common used method to determine the low-cycle fatigue life of metals is the Coffin-Manson method. The simplified Coffin-Manson equation is stated in Equation A.2. Meggiolaro et al. [26] have performed an extensive statistical evaluation of the Coffin-Manson parameters to develop rules of thumb to estimate fatigue properties of metals. Their results are stated in Table A.1, in which V is the coefficient of variation (defined as the ratio between the standard deviation and the mean). The large values of V for σ'_f indicate large scatter in the correlation, which stresses that these rules of thumb should only be

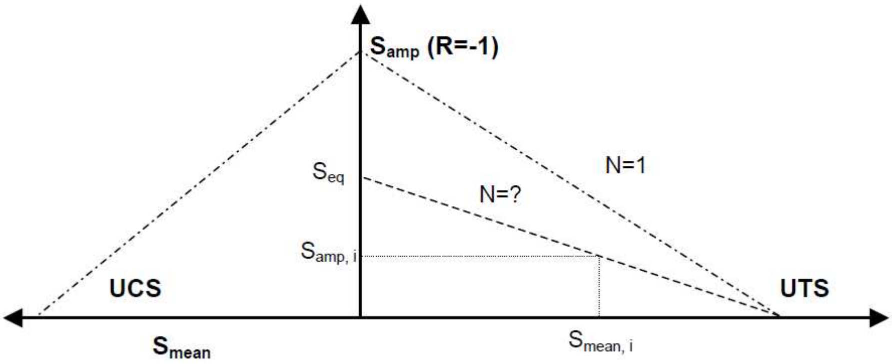

Figure A.1: Linear Goodman constant life diagram [25].

used in an early design stage. Note that the low-cycle fatigue criteria is conservative for the high-cycle region of the S-N curve, especially for steel which exhibits a fatigue limit. Effort should be made to find a methodology to assess high-cycle fatigue for the metal parts if the fatigue load case proves to be a critical load case. Once again the linear Goodman diagram is applied to account for cyclic loads with non-zero mean stresses.

$$\begin{aligned} \frac{\Delta\sigma}{2} &= \sigma'_f \cdot (2 \cdot N_{all})^b \\ N_{all} &= \frac{1}{2} \cdot \left(\frac{\Delta\sigma}{2 \cdot \sigma'_f}\right)^{1/b} \end{aligned} \tag{A.2}$$

Table A.1: Statistical evaluation of the Coffin-Manson parameters [26].

Alloy family	σ'_f **[MPa]**		b [-]		E **[GPa]**	
	Median	**V** [%]	**Median**	V [%]	**Median**	**V** [%]
Steels	1.5 $\cdot\sigma_{all,ult}$	43	-0.09	40	205	3.1
Al alloys	1.9 $\cdot\sigma_{all,ult}$	24	-0.11	28	71	4
Ti alloys	1.9 $\cdot\sigma_{all,ult}$	36	-0.1	37	108	7.4
Ni alloys	1.4 $\cdot\sigma_{all,ult}$	30	-0.08	28	211	3.4
Cast irons	1.2 $\cdot\sigma_{all,ult}$	28	-0.08	29	140	24

Appendix B

Explanation on the optimization code

This appendix elaborates on the optimization code. Chapter 4.1 briefly discusses the code and in Figure 4.1 a flow diagram of the code is presented. This appendix further explains the blocks used in the flow diagram.

BatchRun.m

The function of the batch run file is to coordinate the optimizations. The file is able to catch errors in OptRotor.m and Simulation.m, and restart the optimization when it has crashed. Log files are written to keep track of the attempts made by BatchRun.m to perform an optimization. Error files are written to monitor the occurring error types. Furthermore, to prevent time loss in between two successive optimizations, the file enables performing multiple optimizations in series. The flow diagram of BatchRun.m is shown in Figure B.1. The matlabpool function enables using multiple workers (CPU's) in parallel to perform the optimization. This function is included in the loop, since errors concerning the matlabpool function are common.

OptRotorSet.m

In the batch run file the OptRotorSet.m function is applied. This function is used to generate a structure array containing the options for executing the code. From the structure array it is very clear which options can be set. Furthermore, the OptRotor.m and Simulation.m file do not need to be altered to perform different analyses.

OptRotor.m

OptRotor.m uses the optimization options structure array to initiate the initial design. Furthermore, the optimization problem is formulated based on the options settings. The objective function and the design vector is normalized. Nested functions enable calling Simulation.m only once per evaluation. Furthermore, they enable saving the last iteration point of the optimization. The flow diagram of OptRotor.m is shown in Figure B.2.

Simulation.m

Simulation.m contains the pre-processor and post-processor for the structural analysis of the rotor. Furthermore, the file calls MSC Nastran. The code uses a lot of if-statements to allow for different analysis types. For example, for the extended fatigue analysis the code calls a function to perform a rainflow counting analysis. The flow diagrams for a normal optimization analysis are made for the pre-processor and the post-processor.

The pre-processor in Simulation.m uses the design vector provided by the optimizer to initiate the rotor geometry. The pre-processor uses a similar approach as in OptRotor.m. The laminate thicknesses (following from the design vector) and the rotor geometry are used to determine the objective function. The aerodynamic load is determined at the nodes of the blade. The FEM formulation of the rotor design and loads is generated and written to the input file for MSC Nastran. The flow diagram of the pre-processor in Simulation.m is shown in Figure B.3.

The post-processor in Simulation.m reads the output provided by MSC Nastran. The output contains the stresses for each element for the different loading conditions. The stresses are used to perform a fatigue analysis. The maximum failure indices of the failure modes are determined per section. The failure indices are processed into the inequality constraints. The flow diagram of the post-processor in Simulation.m is shown in Figure B.4.

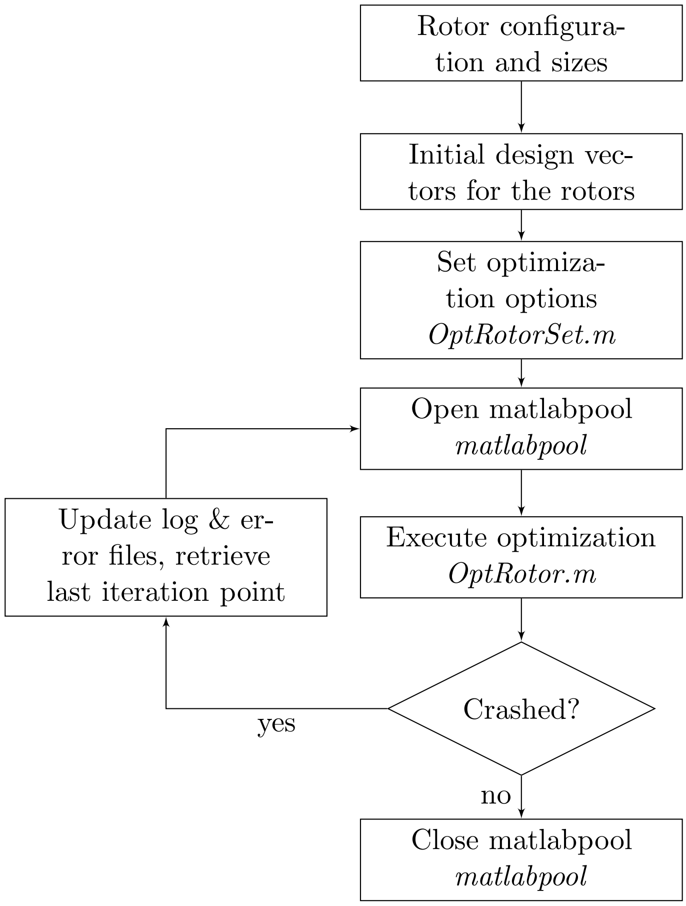

Figure B.1: BatchRun.m flow diagram.

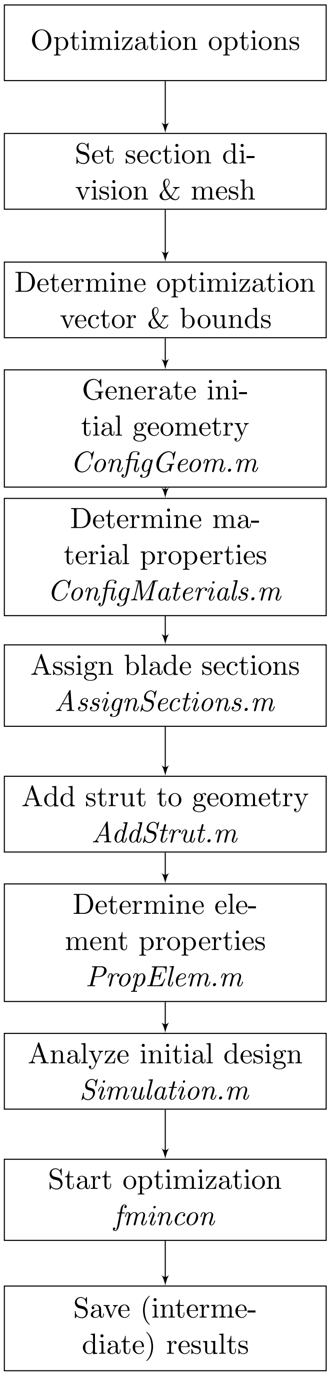

Figure B.2: OptRotor.m flow diagram.

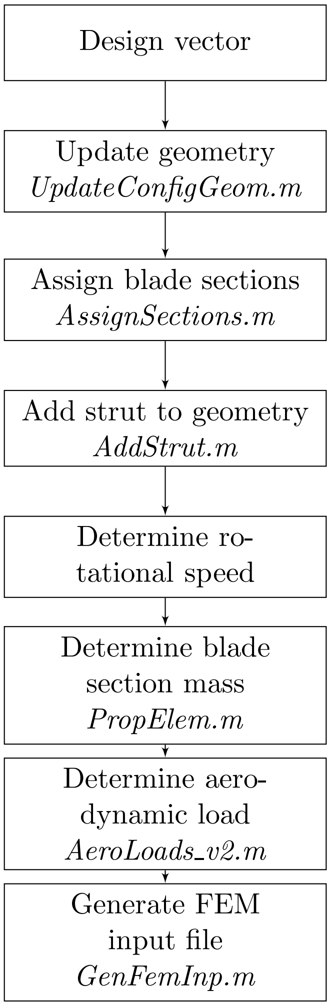

Figure B.3: Flow diagram of pre-processor in Simulation.m.

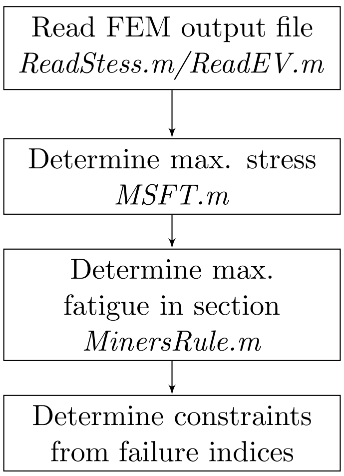

Figure B.4: Flow diagram of post-processor in Simulation.m.

Appendix C

Results sizing optimization H-rotor

In this appendix, plots of the internal loads and failure indices of the sizing optimized H-rotors are provided.

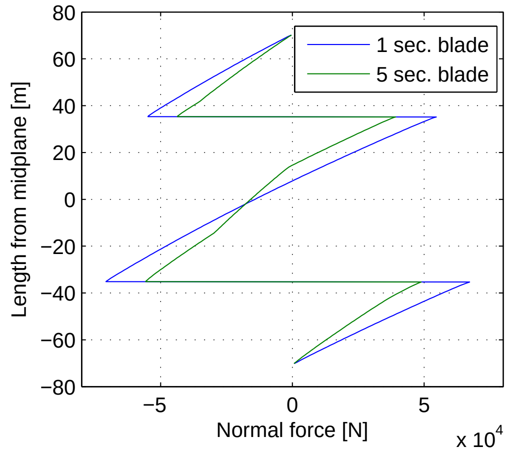

(a) Internal normal force.

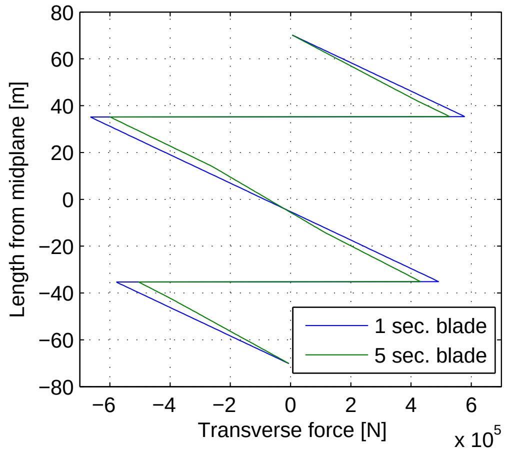

(b) Internal transverse force (in z-direction).

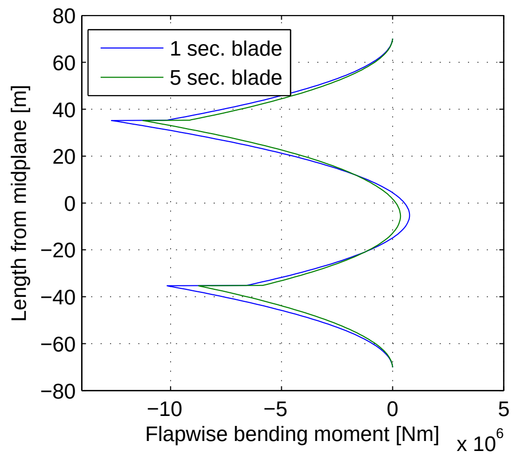

(c) Internal flapwise bending moment.

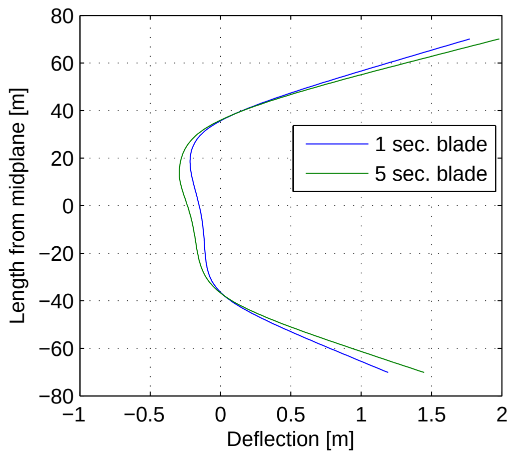

(d) Blade deflection (in z-direction).

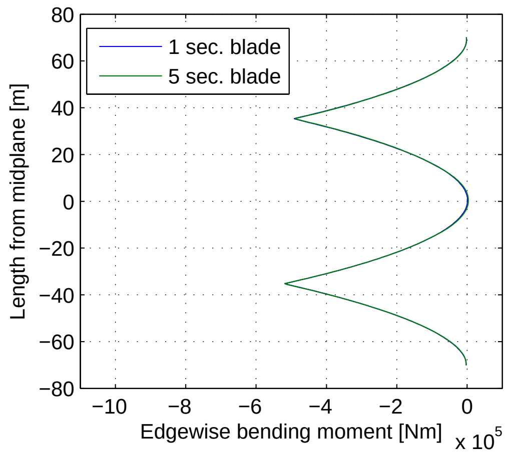

(e) Internal edgewise bending moment.

Figure C.1: Internal blade loads and blade deflection in normal operation conditions, downwind blade position.

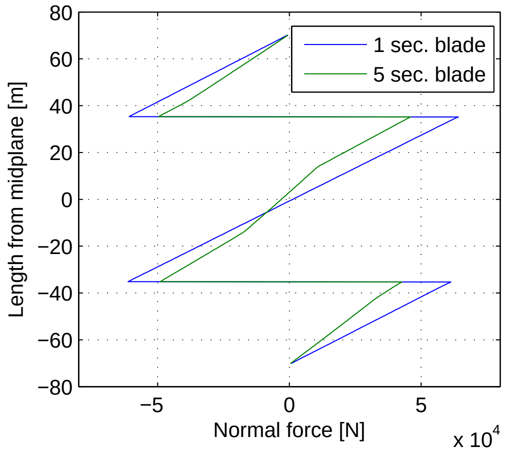

(a) Internal normal force.

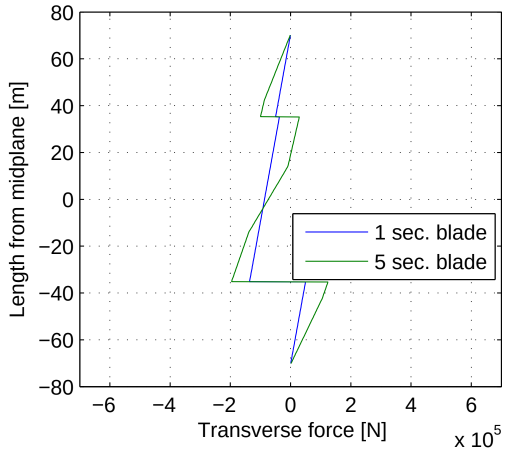

(b) Internal transverse force (in z-direction).

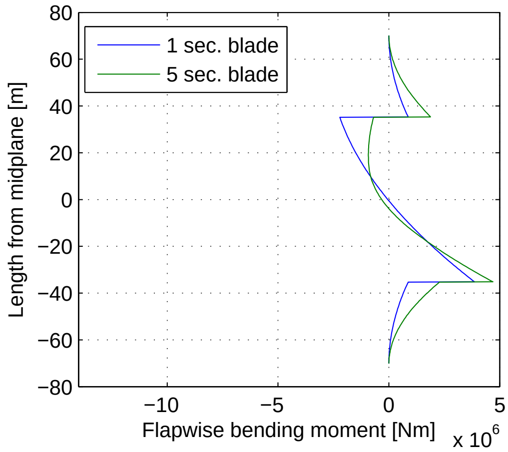

(c) Internal flapwise bending moment.

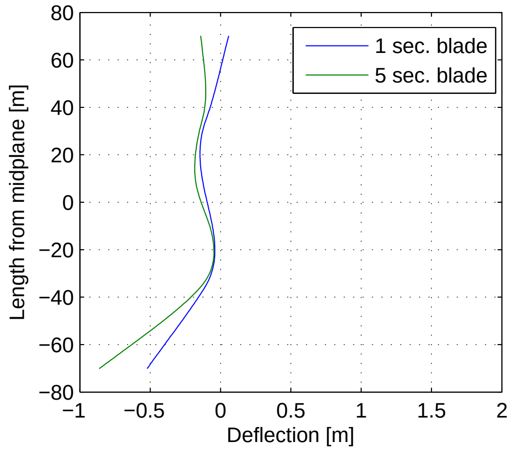

(d) Blade deflection (in z-direction).

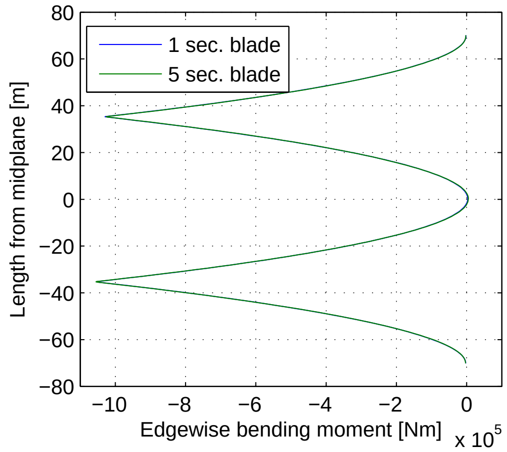

(e) Internal edgewise bending moment.

Figure C.2: Internal blade loads and blade deflection in normal operation conditions, upwind blade position.

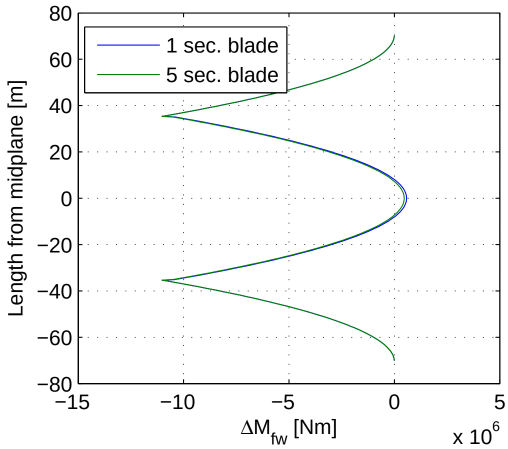

Figure C.3: Difference in flapwise bending moment in the blade between the up- and downwind position.

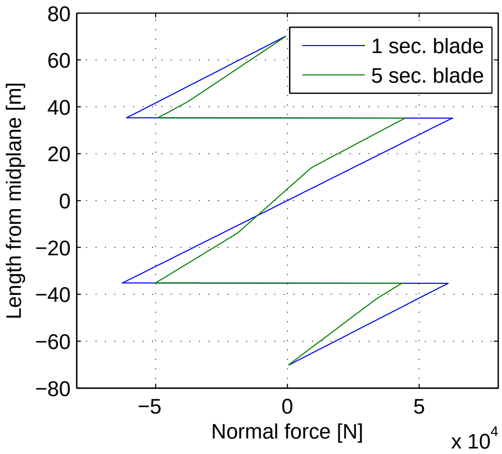

(a) Internal normal force.

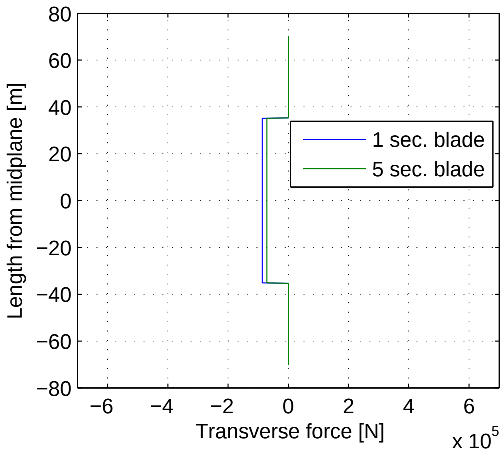

(b) Internal transverse force (in z-direction).

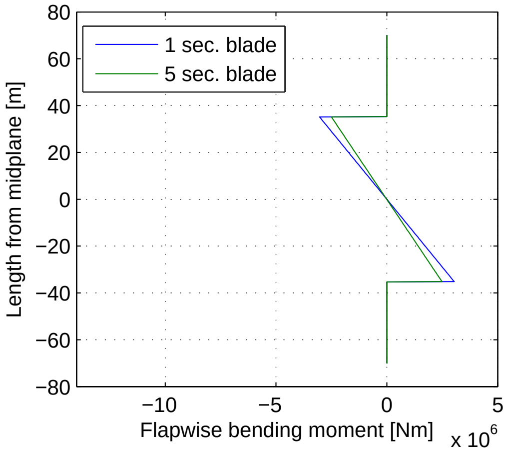

(c) Internal flapwise bending moment.

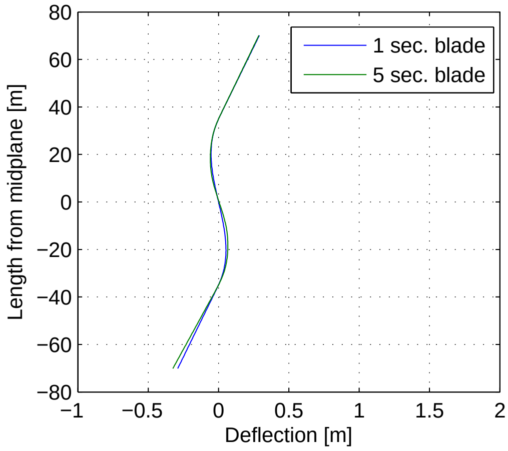

(d) Blade deflection (in z-direction).

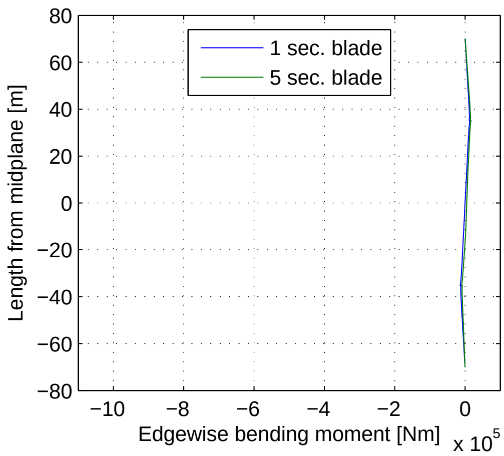

(e) Internal edgewise bending moment.

Figure C.4: Internal blade loads and blade deflection in parked conditions.

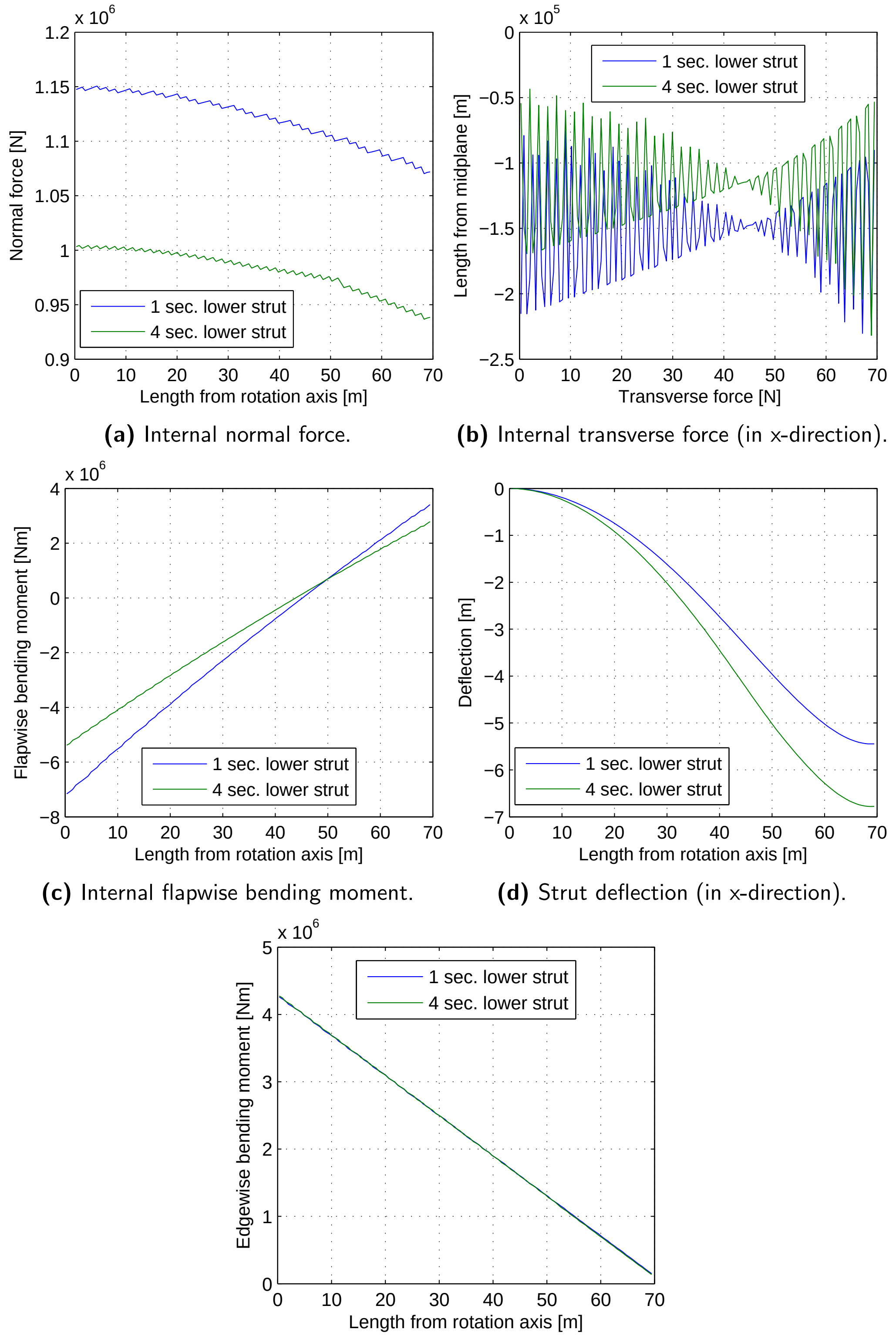

(a) Internal normal force.

(b) Internal transverse force (in x-direction).

(c) Internal flapwise bending moment.

(d) Strut deflection (in x-direction).

(e) Internal edgewise bending moment.

Figure C.5: Internal strut loads and strut deflection in normal operation conditions, downwind blade position.

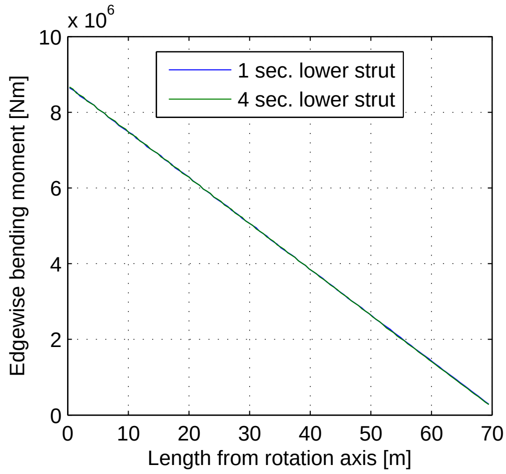

Figure C.6: Internal edgewise bending moment in the strut in normal operation conditions, upwind blade position.

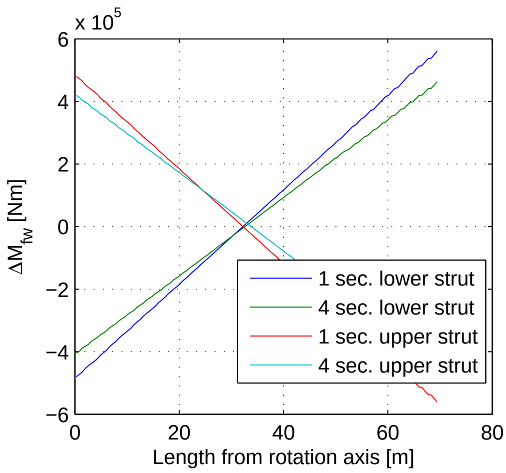

Figure C.7: Difference in flapwise bending moment in the strut between the up- and downwind position.

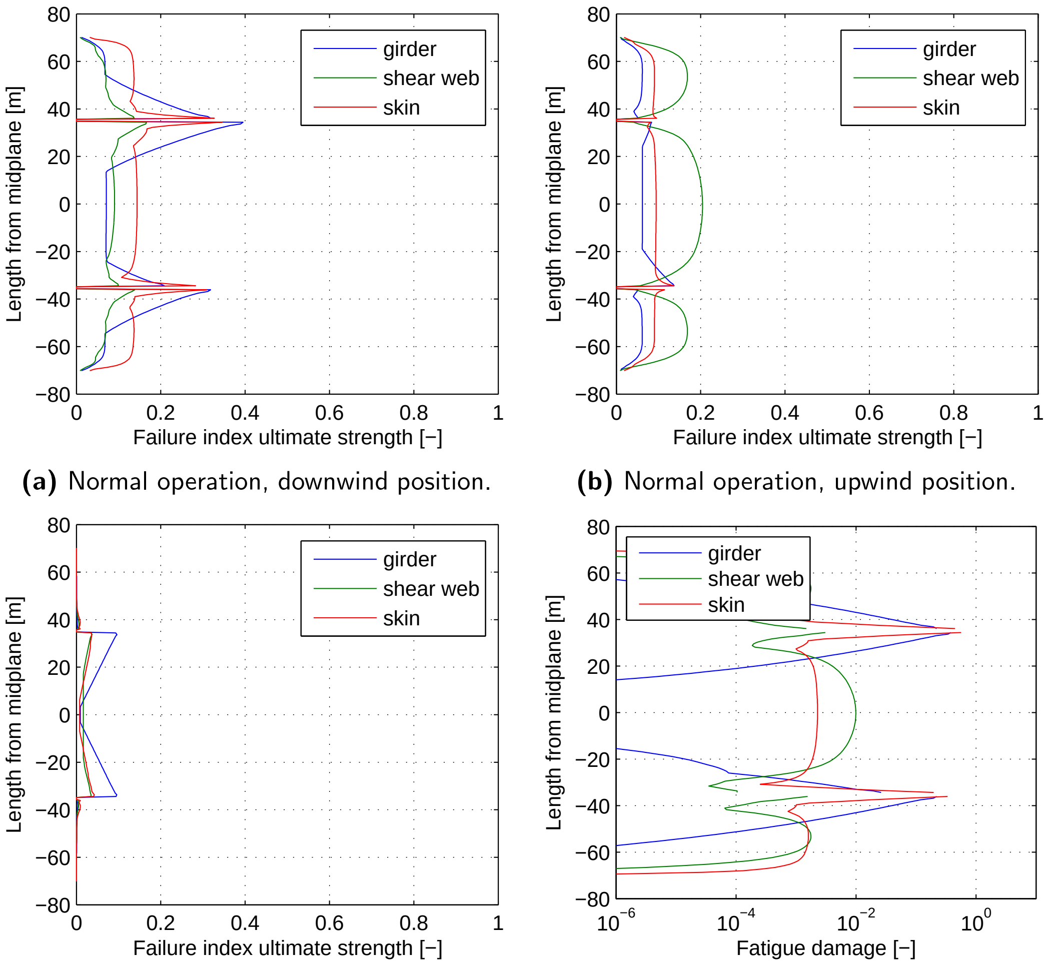

(a) Normal operation, downwind position.

(b) Normal operation, upwind position.

(c) Parked conditions.

(d) Fatigue.

Figure C.8: Failure indices of the structural members along the length of the blade: single section.

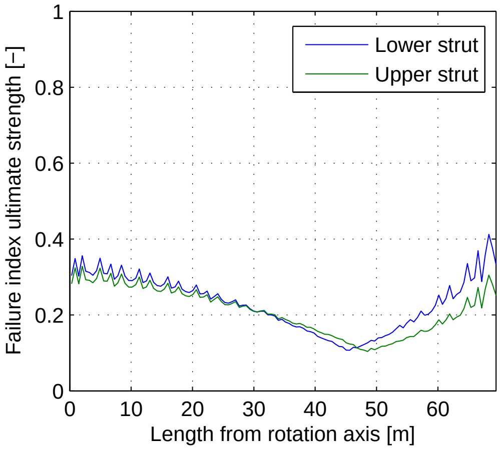

(a) Normal operation, downwind position.

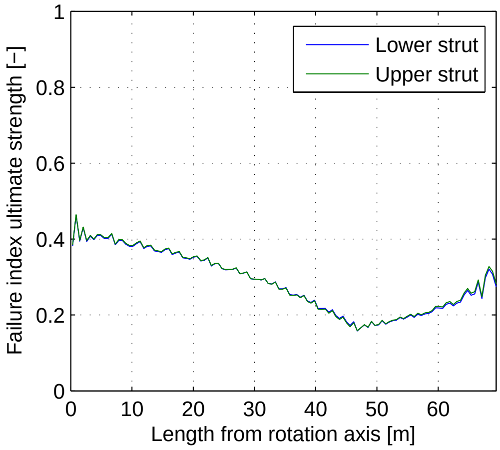

(b) Normal operation, upwind position.

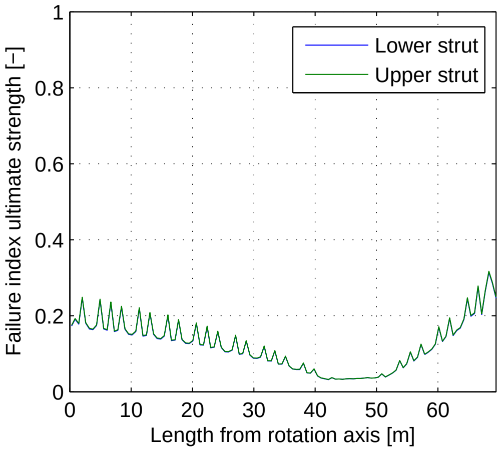

(c) Parked conditions.

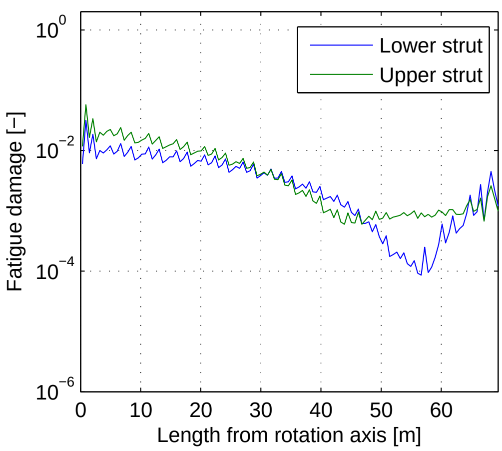

(d) Fatigue.

Figure C.9: Failure indices of the laminate along the length of the strut: single section.

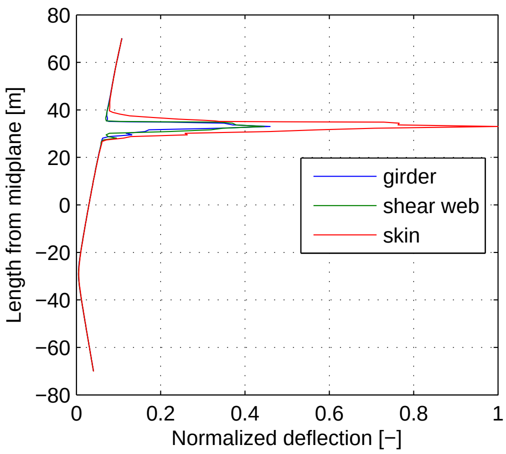

(a) First buckling mode; normal operation, downwind position (EV = 1.00).

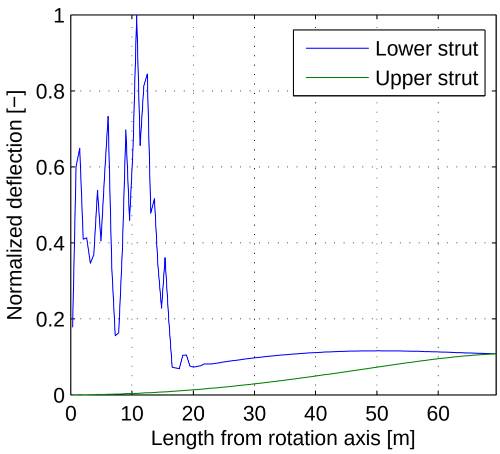

(b) First buckling mode (strut); parked conditions (EV = 1.59).

Figure C.10: Buckling deflections of the structural members: single section.

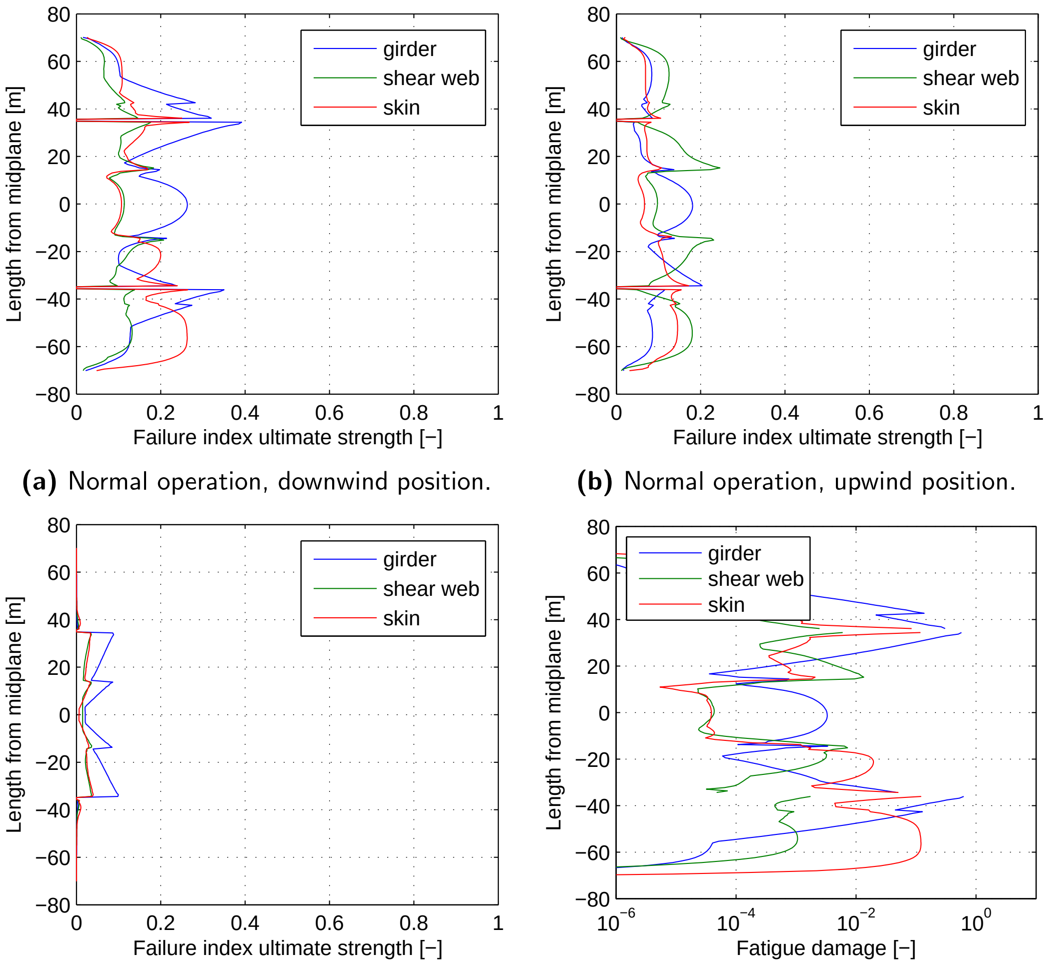

(a) Normal operation, downwind position.

(b) Normal operation, upwind position.

(c) Parked conditions.

(d) Fatigue.

Figure C.11: Failure indices of the structural members along the length of the blade: 5 sections.

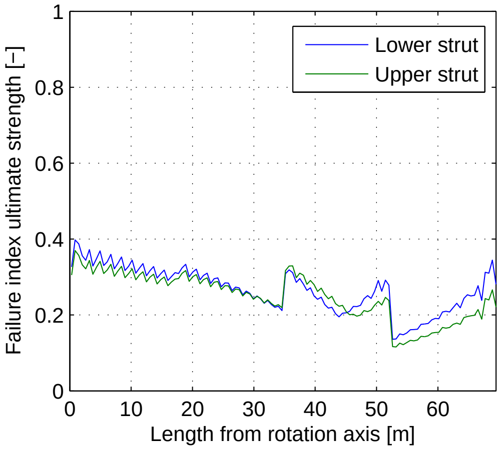

(a) Normal operation, downwind position.

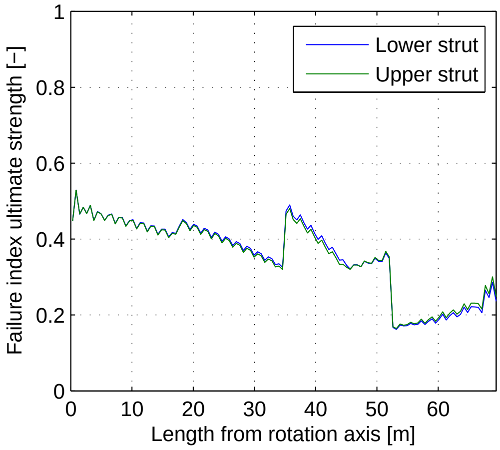

(b) Normal operation, upwind position.

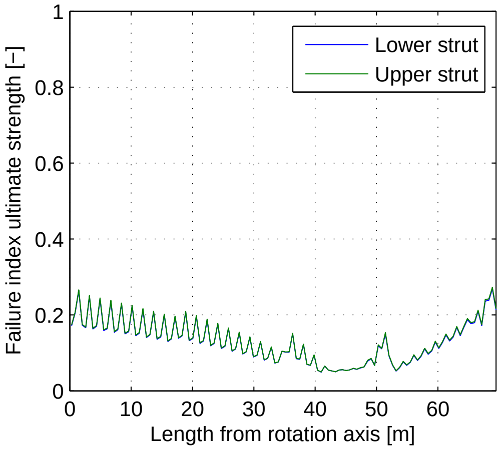

(c) Parked conditions.

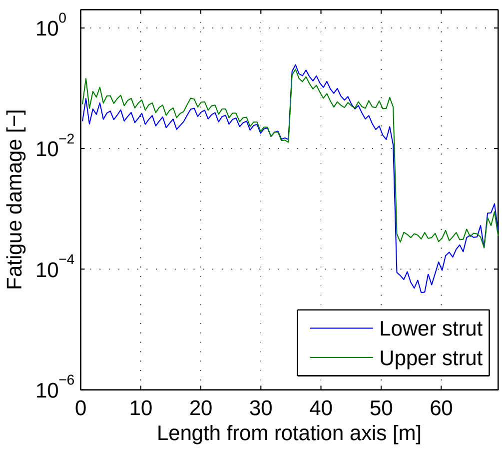

(d) Fatigue.

Figure C.12: Failure indices of the laminate along the length of the strut: 4 sections.

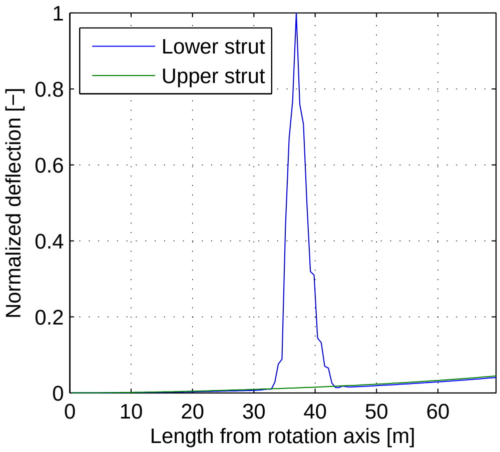

(a) First buckling mode (strut); normal operation, downwind position (EV = 0.95).

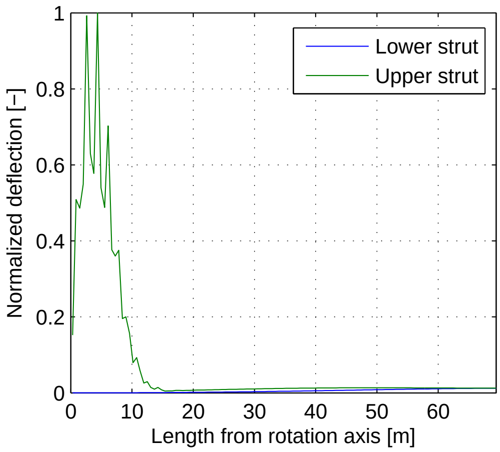

(b) First buckling mode (strut); parked conditions (EV = 1.20).

Figure C.13: Buckling deflections of the structural members: 5 sections.

Appendix D

Results sizing optimization Darrieus rotor

In this appendix, plots of the internal loads and failure indices of the sizing optimized Darrieus rotors are provided.

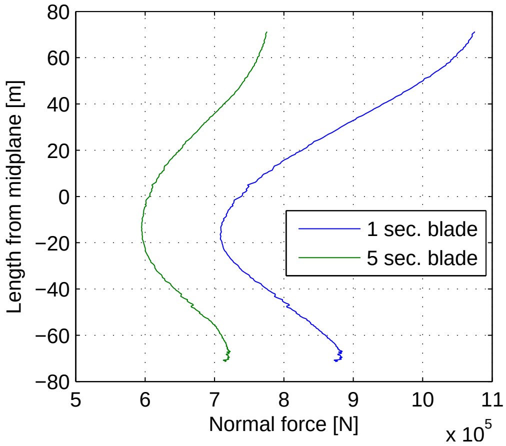

(a) Internal normal force.

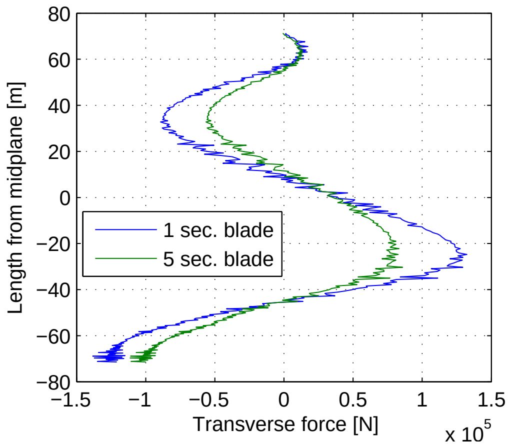

(b) Internal transverse force (in x-z plane).

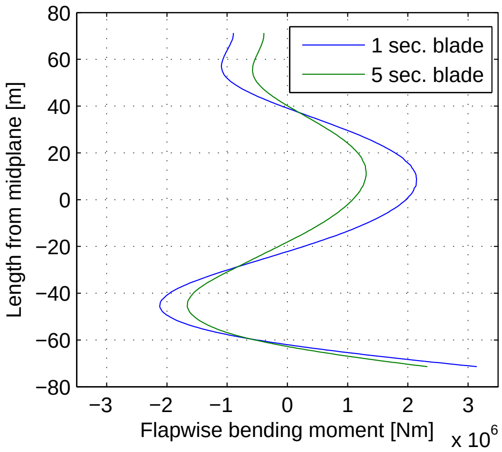

(c) Internal flapwise bending moment.

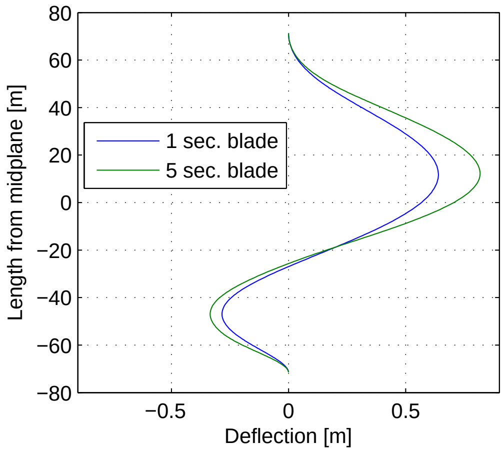

(d) Blade deflection (in z-direction).

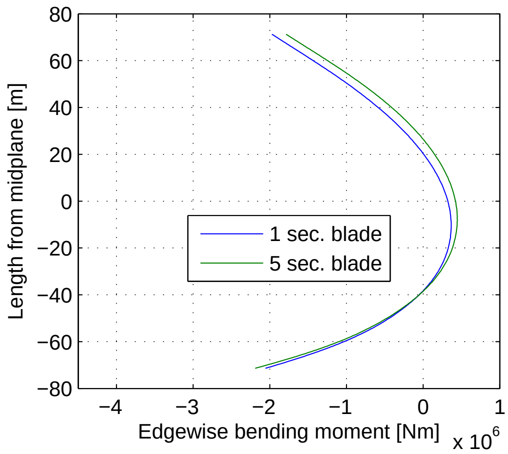

(e) Internal edgewise bending moment.

Figure D.1: Internal blade loads and blade deflection in normal operation conditions, downwind blade position.

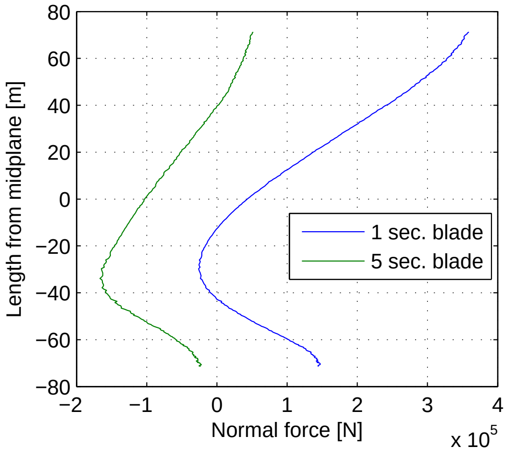

(a) Internal normal force.

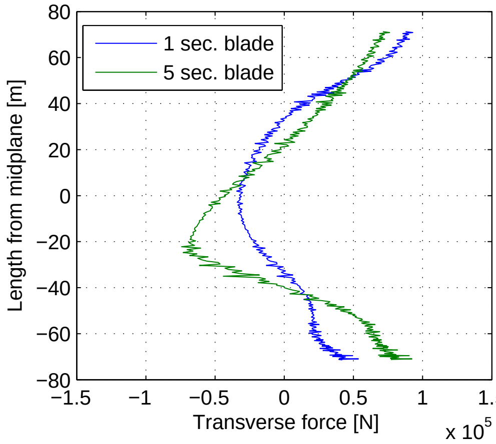

(b) Internal transverse force (in x-z plane).

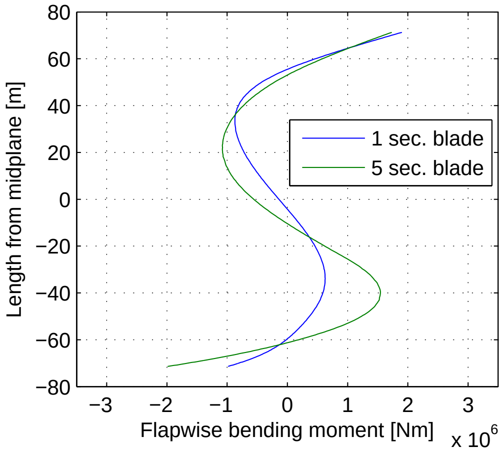

(c) Internal flapwise bending moment.

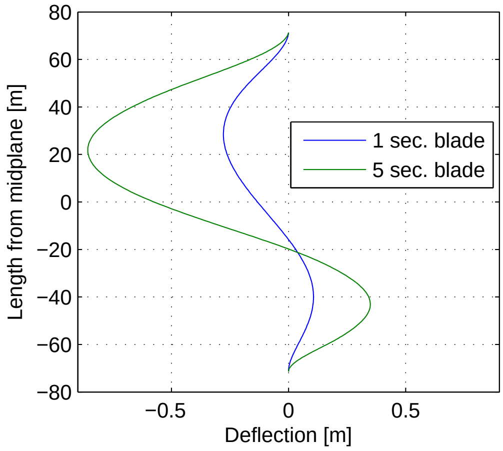

(d) Blade deflection (in z-direction).

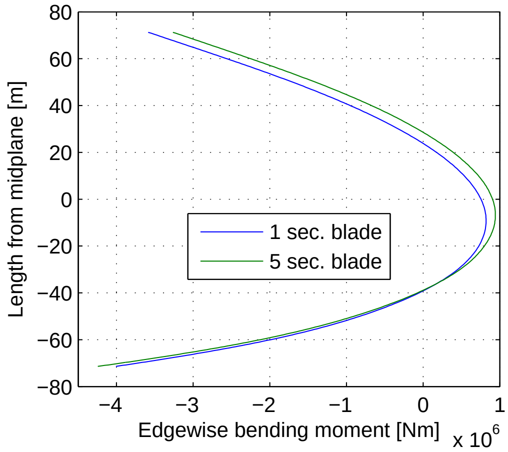

(e) Internal edgewise bending moment.

Figure D.2: Internal blade loads and blade deflection in normal operation conditions, upwind blade position.

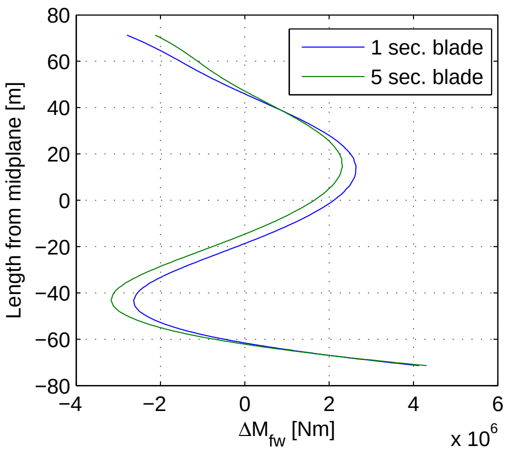

Figure D.3: Difference in flapwise bending moment in the blade between the up- and downwind position.

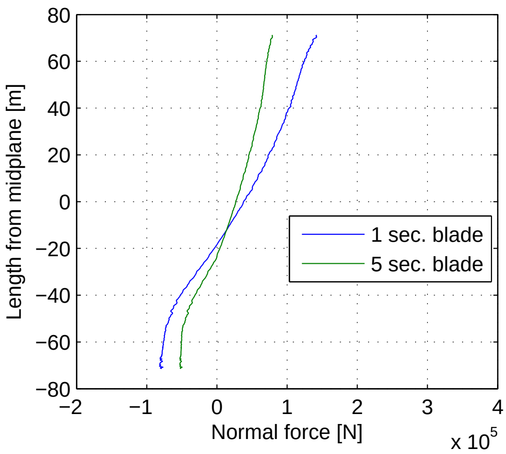

(a) Internal normal force.

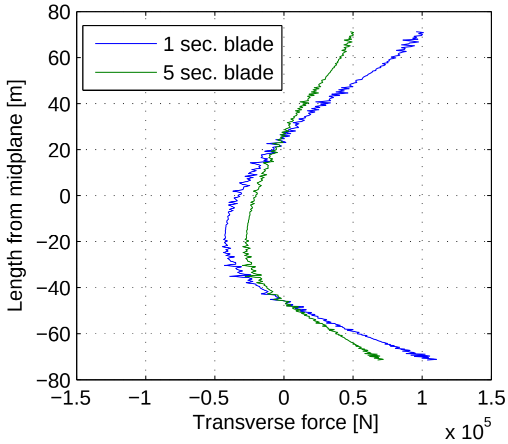

(b) Internal transverse force (in x-z plane).

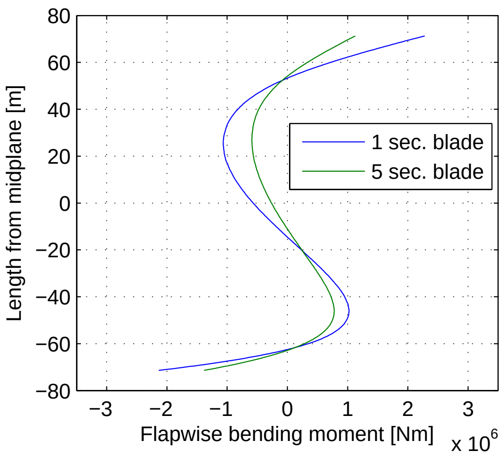

(c) Internal flapwise bending moment.

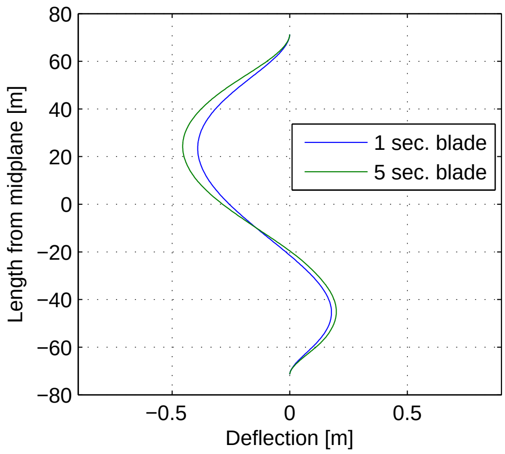

(d) Blade deflection (in z-direction).

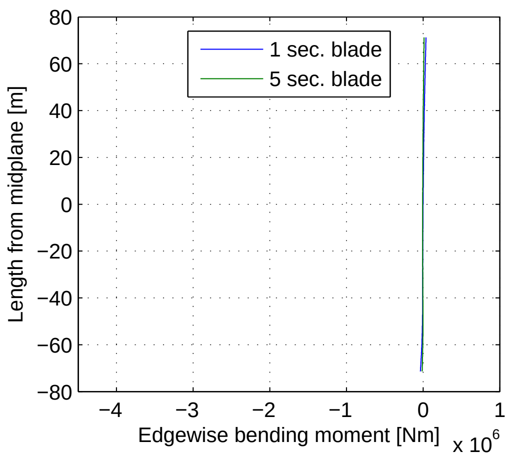

(e) Internal edgewise bending moment.

Figure D.4: Internal blade loads and blade deflection in parked conditions.

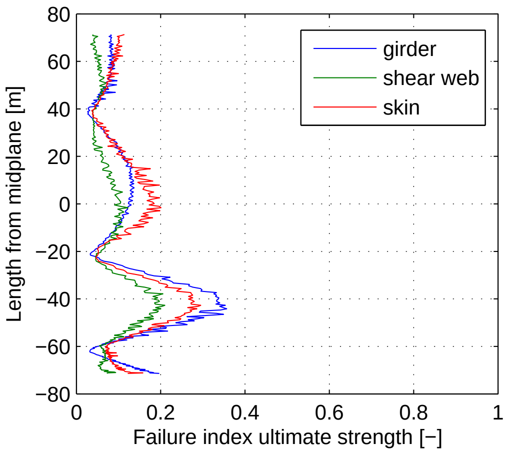

(a) Normal operation, downwind position.

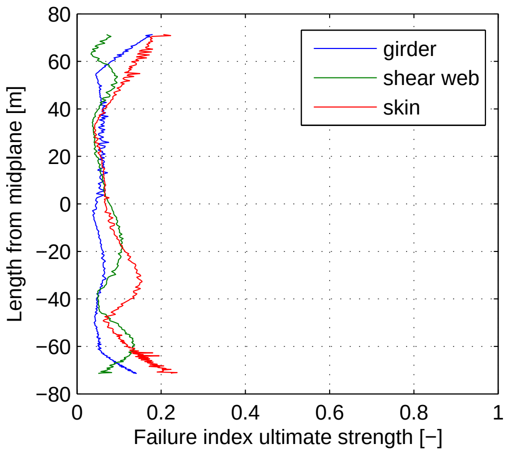

(b) Normal operation, upwind position.

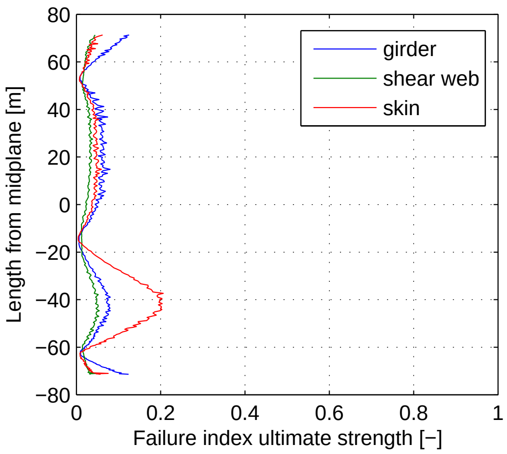

(c) Parked conditions.

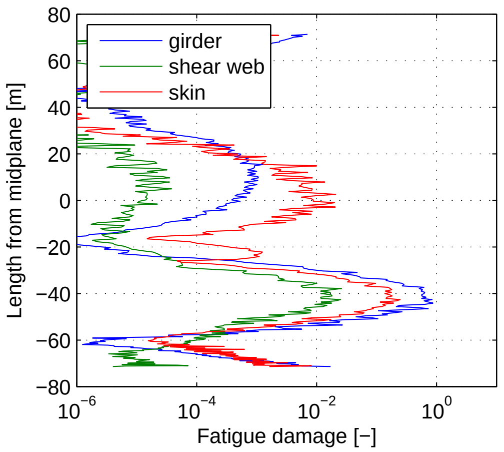

(d) Fatigue.

Figure D.5: Failure indices of the structural members along the length of the blade: single section.

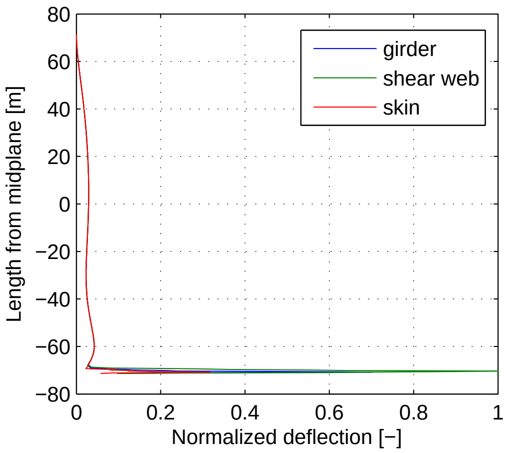

(a) First buckling mode; normal operation, downwind position (EV = 3.32).

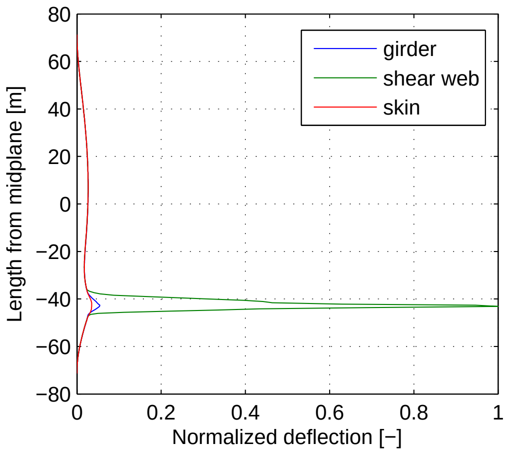

(b) First buckling mode; parked conditions (EV = 2.96).

Figure D.6: Buckling deflections of the structural members along the length of the blade: single section.

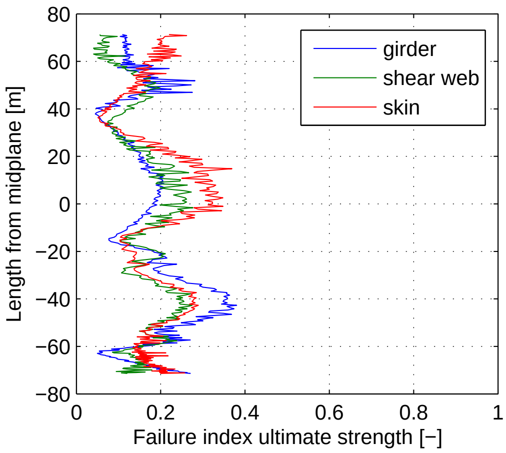

(a) Normal operation, downwind position.

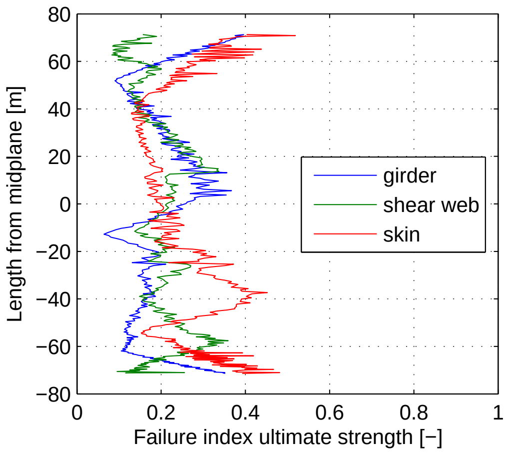

(b) Normal operation, upwind position.

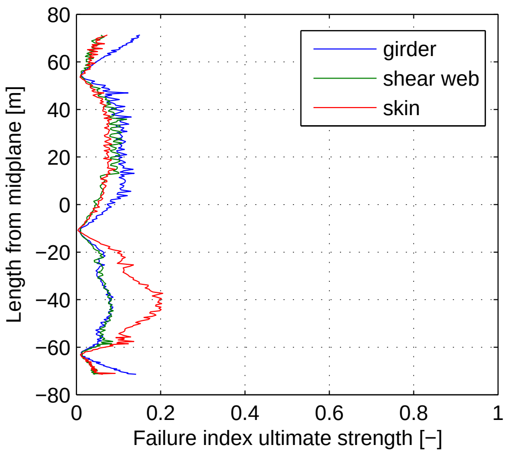

(c) Parked conditions.

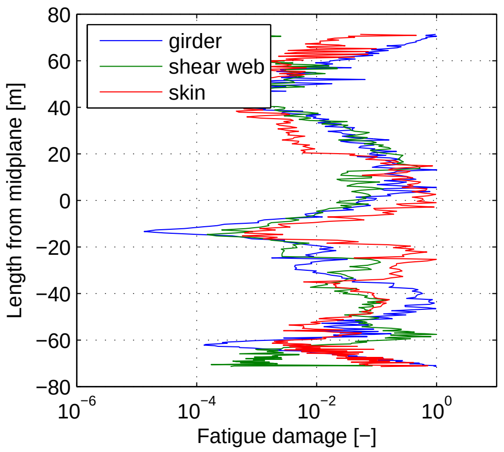

(d) Fatigue.

Figure D.7: Failure indices of the structural members along the length of the blade: 5 sections.

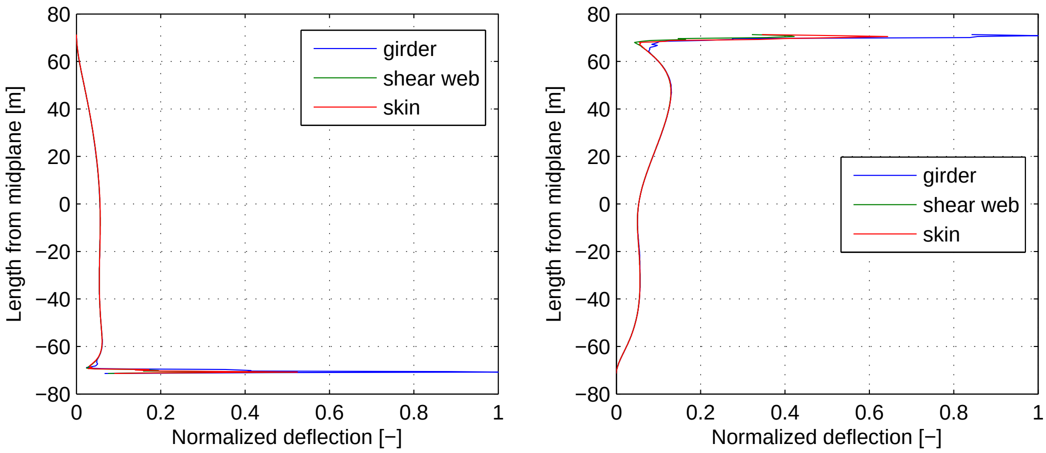

(a) First buckling mode; normal operation, downwind position (EV = 1.30).

(b) First buckling mode; parked conditions (EV = 1.37).

Figure D.8: Buckling deflections of the structural members along the length of the blade: 5 sections.

Appendix E

Results shape optimization Darrieus rotor

In this appendix, plots of the internal loads and failure indices of the shape optimized Darrieus rotor are provided.

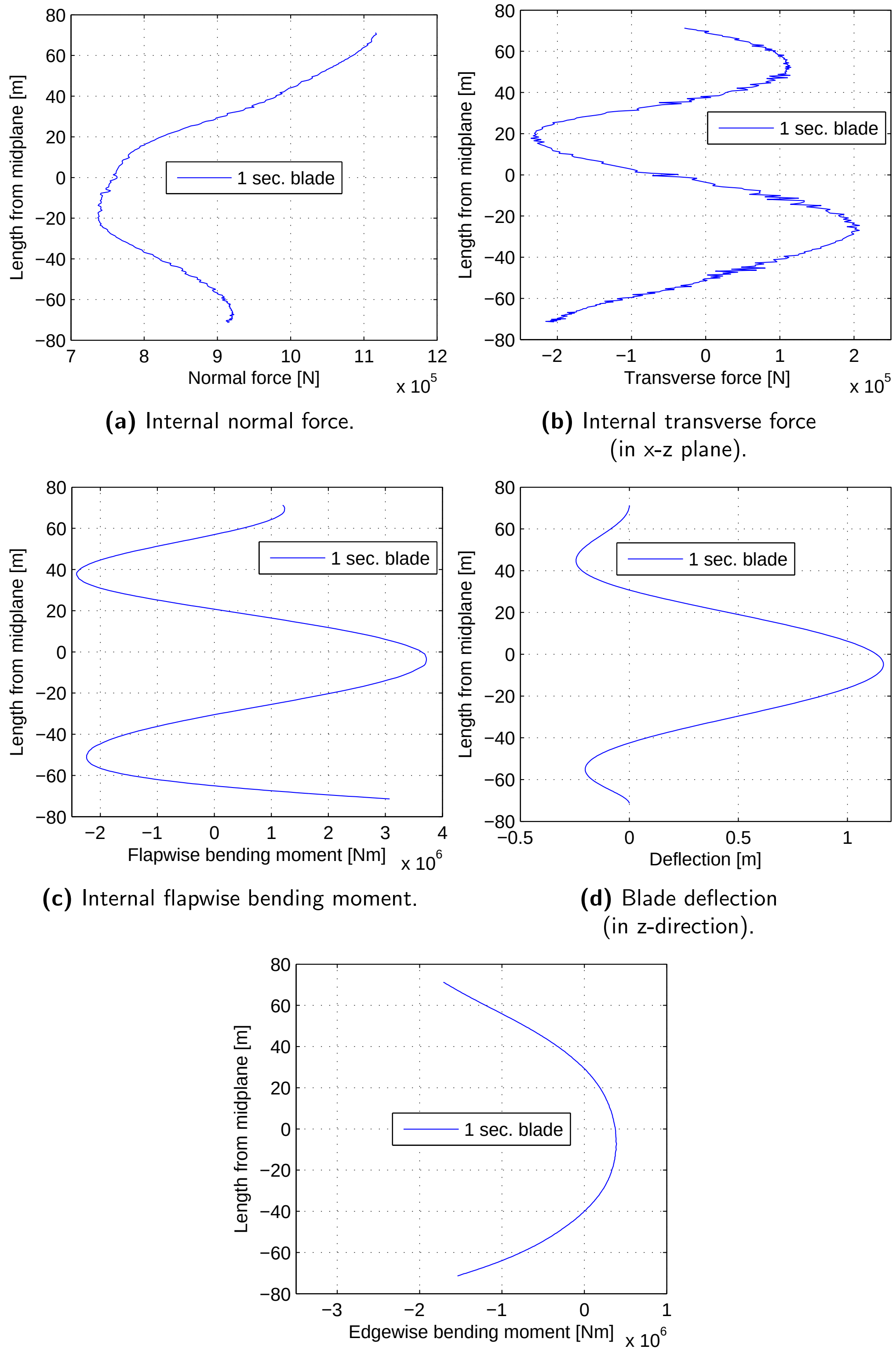

(a) Internal normal force.

(b) Internal transverse force (in x-z plane).

(c) Internal flapwise bending moment.

(d) Blade deflection (in z-direction).

(e) Internal edgewise bending moment.

Figure E.1: Internal blade loads and blade deflection in normal operation conditions, downwind blade position.

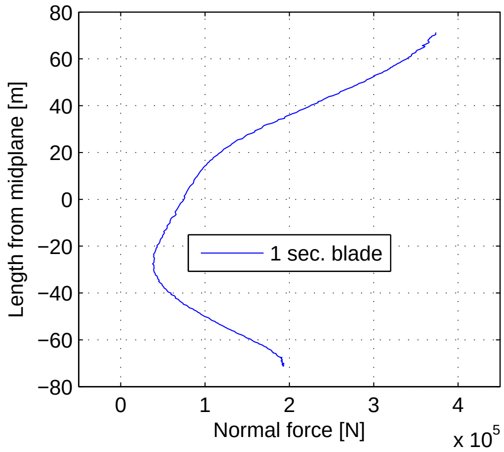

(a) Internal normal force.

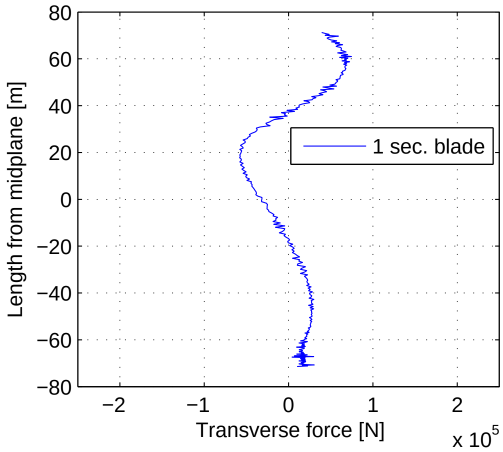

(b) Internal transverse force (in x-z plane).

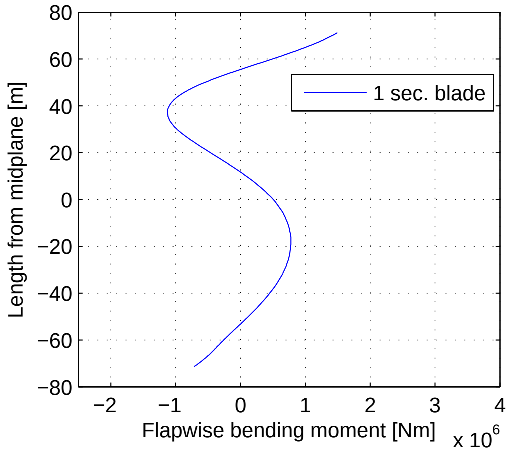

(c) Internal flapwise bending moment.

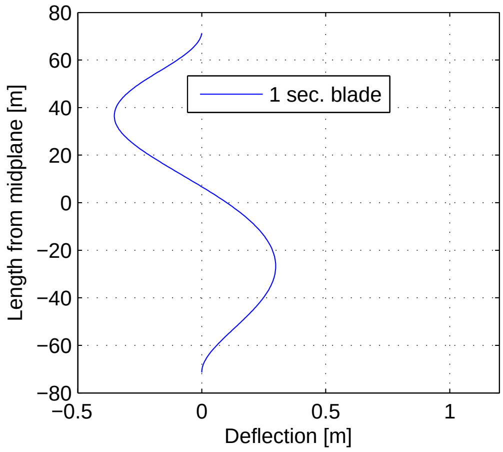

(d) Blade deflection (in z-direction).

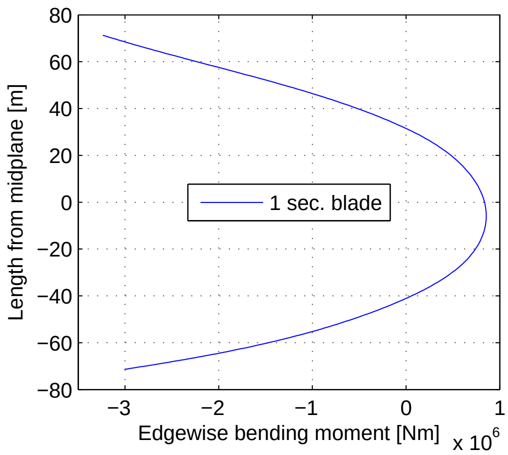

(e) Internal edgewise bending moment.

Figure E.2: Internal blade loads and blade deflection in normal operation conditions, upwind blade position.

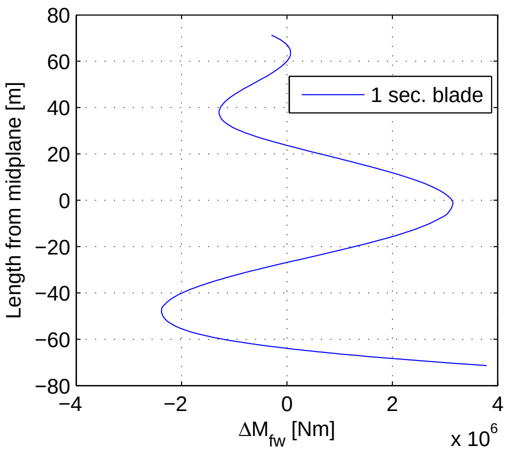

Figure E.3: Difference in flapwise bending moment in the blade between the up- and downwind position.

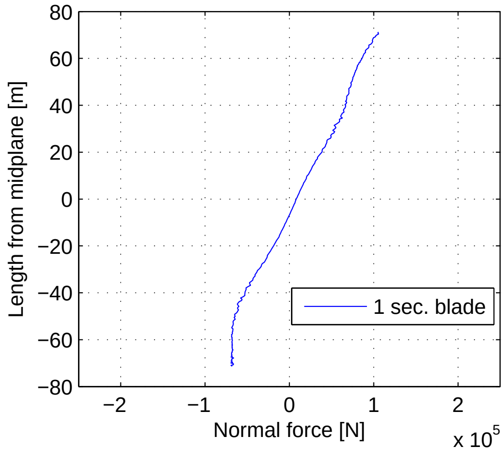

(a) Internal normal force.

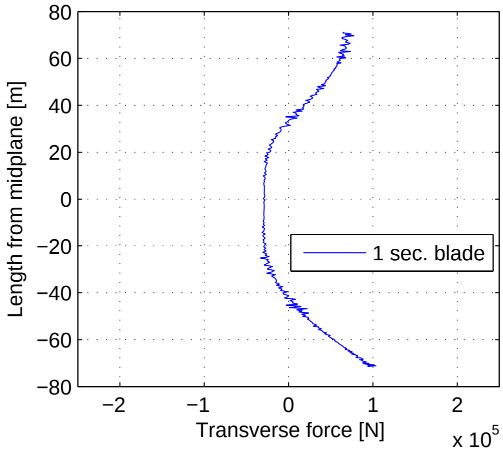

(b) Internal transverse force (in x-z plane).

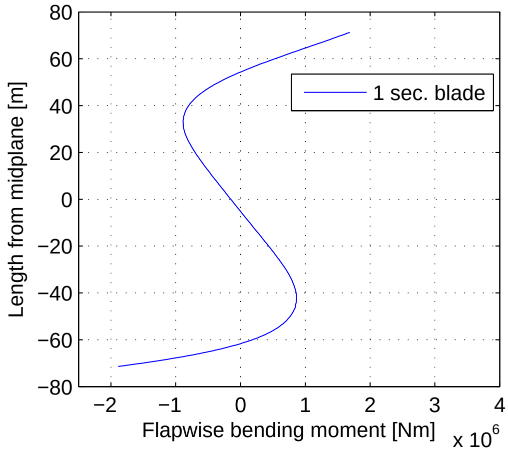

(c) Internal flapwise bending moment.

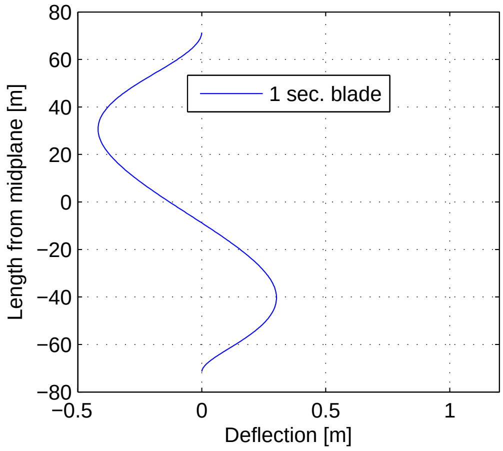

(d) Blade deflection (in z-direction).

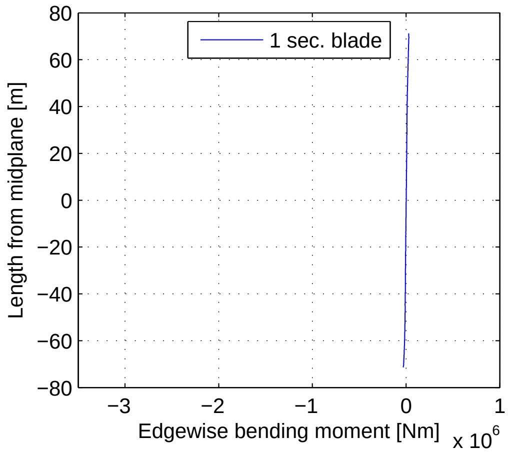

(e) Internal edgewise bending moment.

Figure E.4: Internal blade loads and blade deflection in parked conditions.

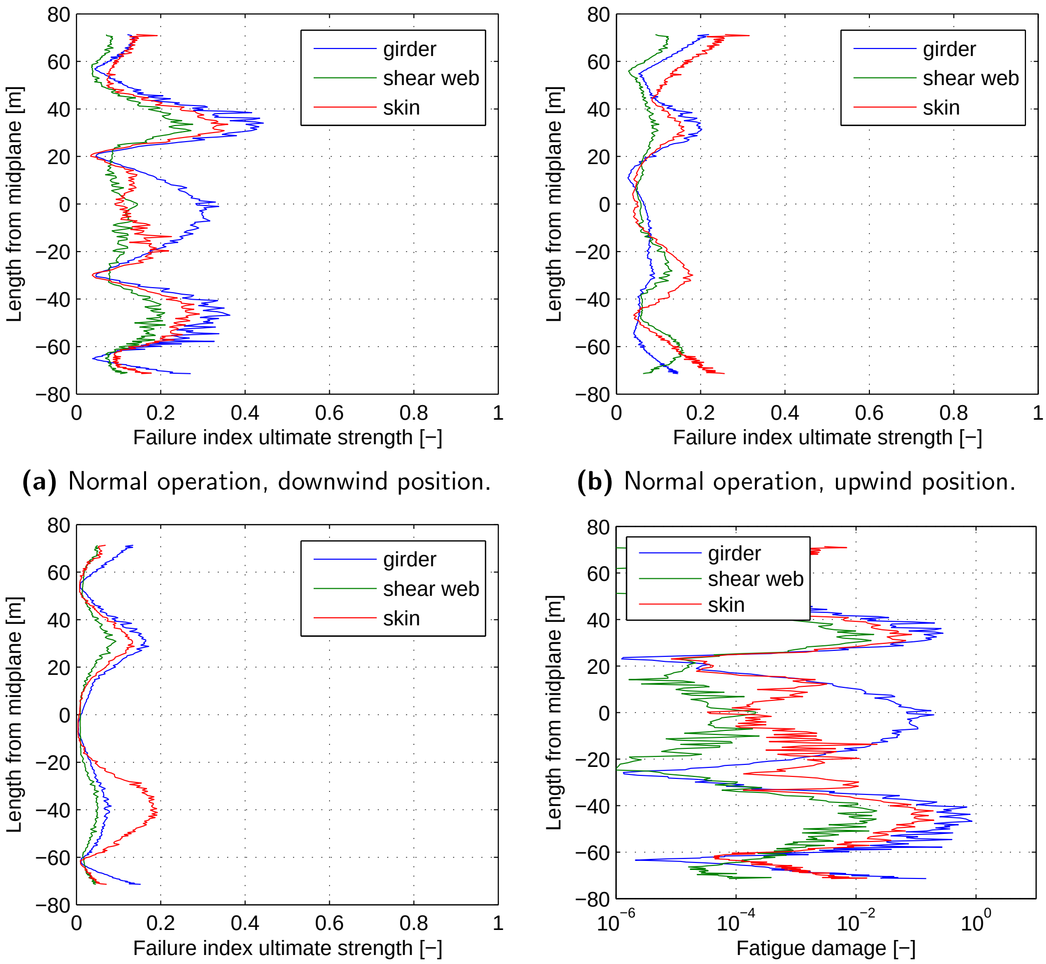

(a) Normal operation, downwind position.

(b) Normal operation, upwind position.

(c) Parked conditions.

(d) Fatigue.

Figure E.5: Failure indices of the structural members along the length of the blade: single section.

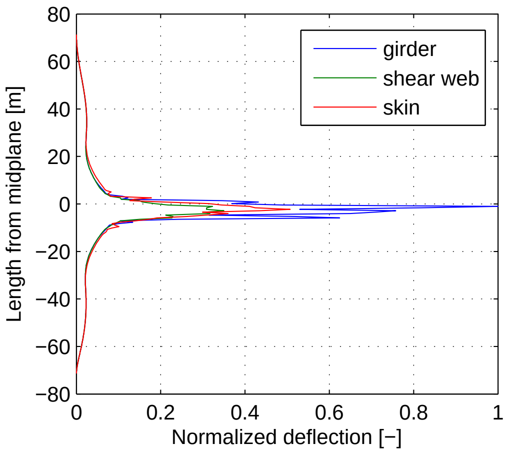

(a) First buckling mode; normal operation, downwind position (EV = 2.08).

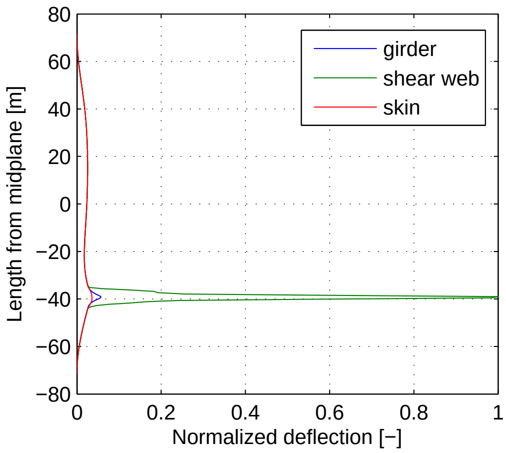

(b) First buckling mode; parked conditions (EV = 3.91).

Figure E.6: Buckling deflections of the structural members along the length of the blade: single section.

Appendix F

Results combined optimization H-rotor

In this appendix, plots of the internal loads and failure indices of the combined optimized H-rotors are provided.

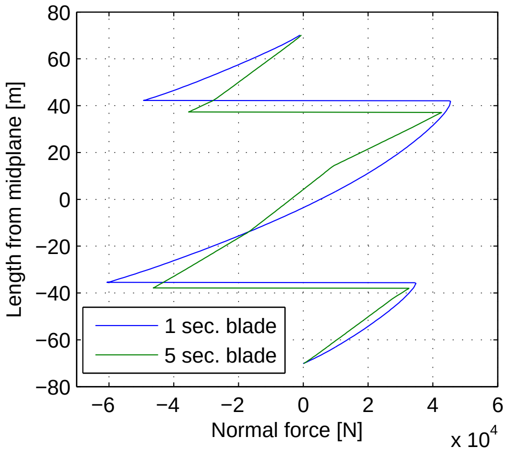

(a) Internal normal force.

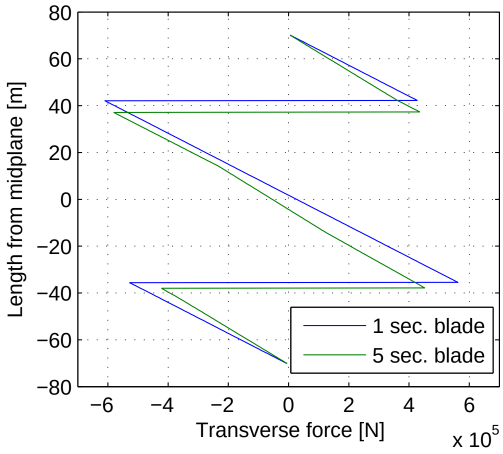

(b) Internal transverse force (in z-direction).

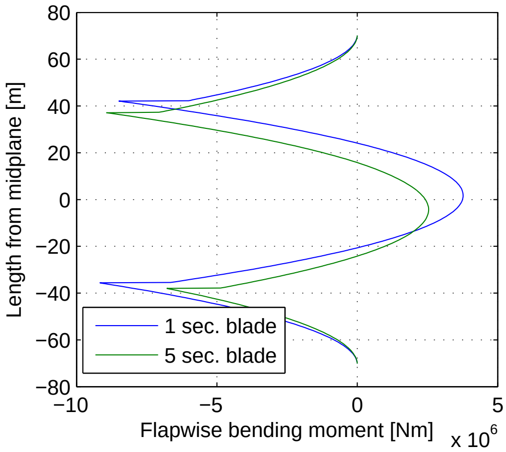

(c) Internal flapwise bending moment.

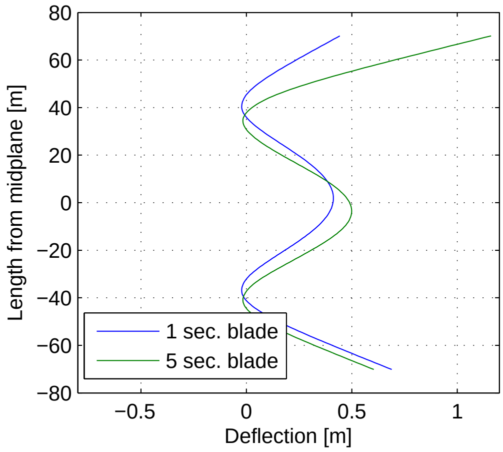

(d) Blade deflection (in z-direction).

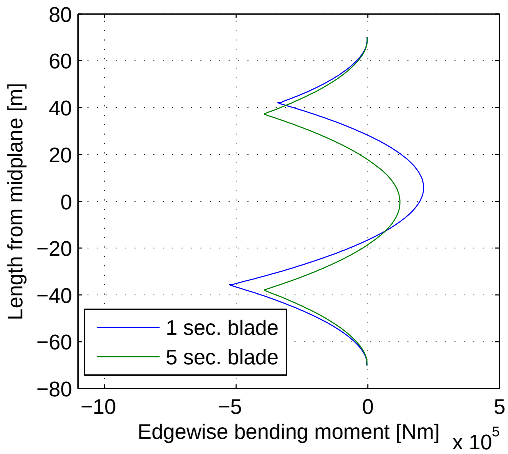

(e) Internal edgewise bending moment.

Figure F.1: Internal blade loads and blade deflection in normal operation conditions, downwind blade position.

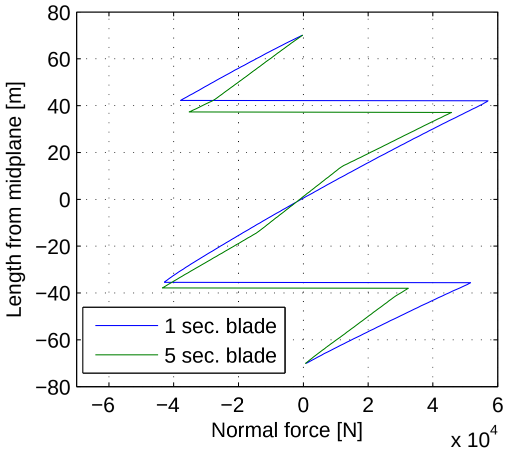

(a) Internal normal force.

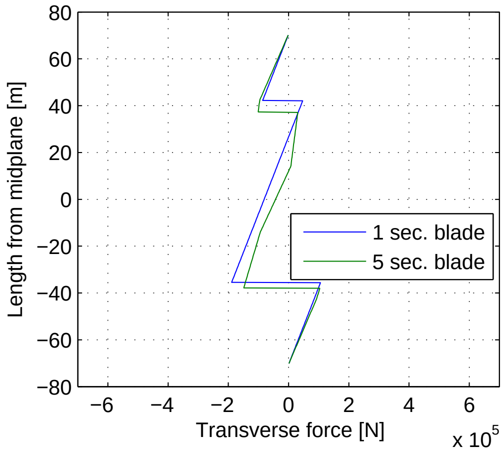

(b) Internal transverse force (in z-direction).

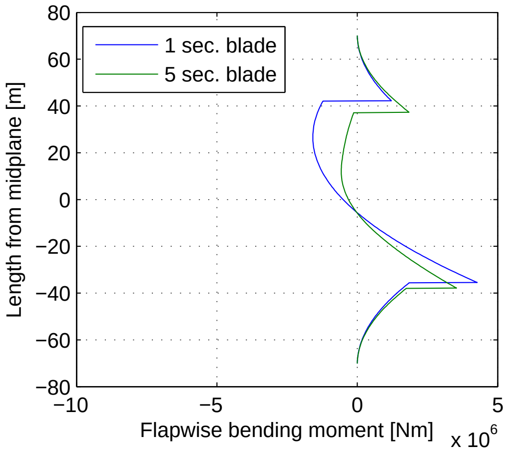

(c) Internal flapwise bending moment.

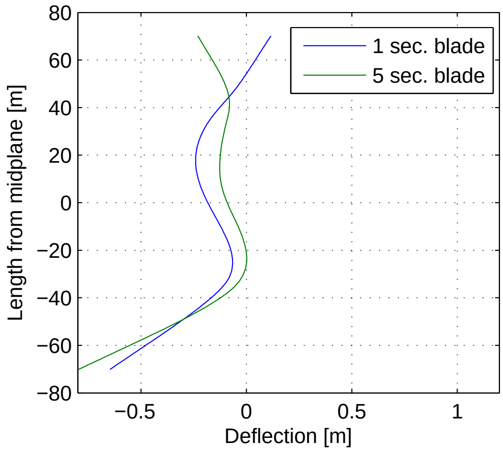

(d) Blade deflection (in z-direction).

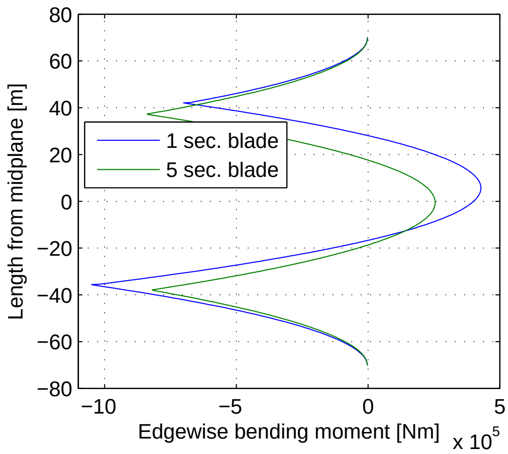

(e) Internal edgewise bending moment.

Figure F.2: Internal blade loads and blade deflection in normal operation conditions, upwind blade position.

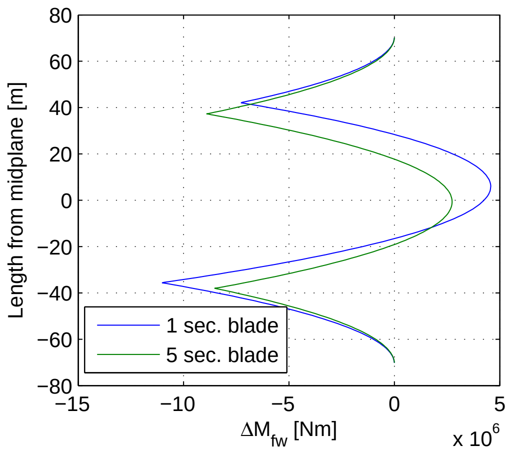

Figure F.3: Difference in flapwise bending moment in the blade between the up- and downwind position.

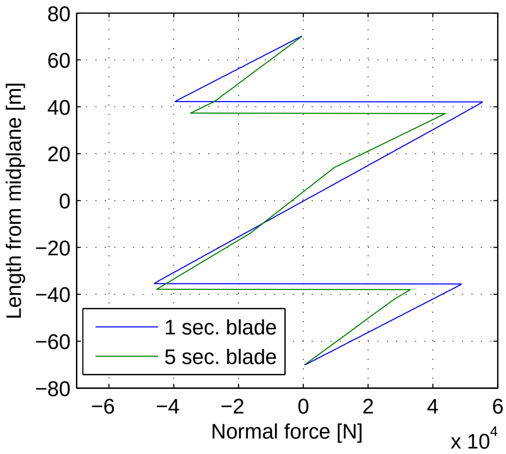

(a) Internal normal force.

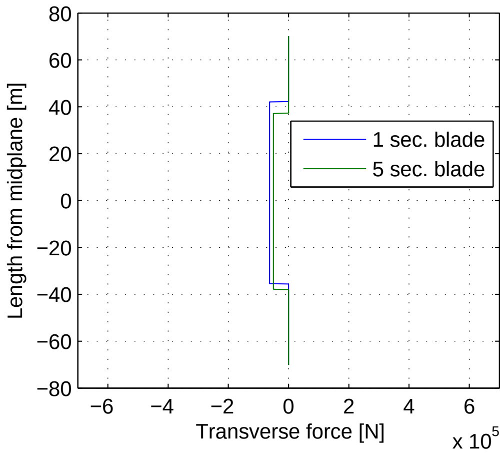

(b) Internal transverse force (in z-direction).

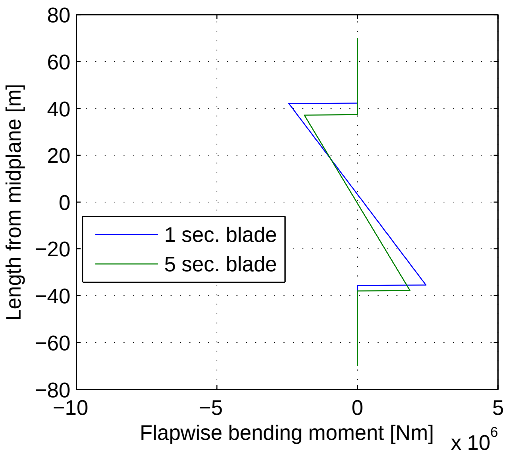

(c) Internal flapwise bending moment.

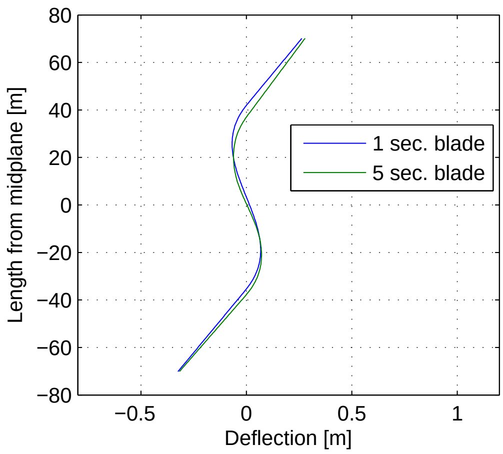

(d) Blade deflection (in z-direction).

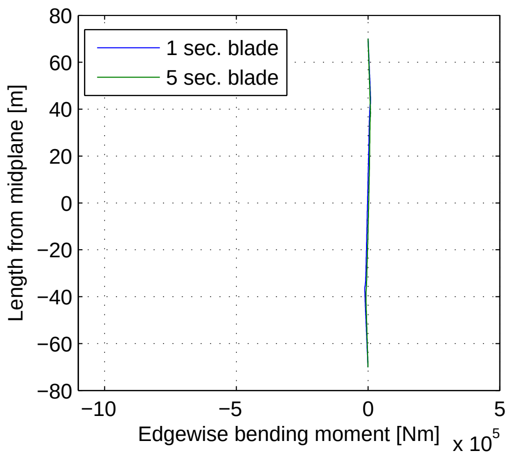

(e) Internal edgewise bending moment.

Figure F.4: Internal blade loads and blade deflection in parked conditions.

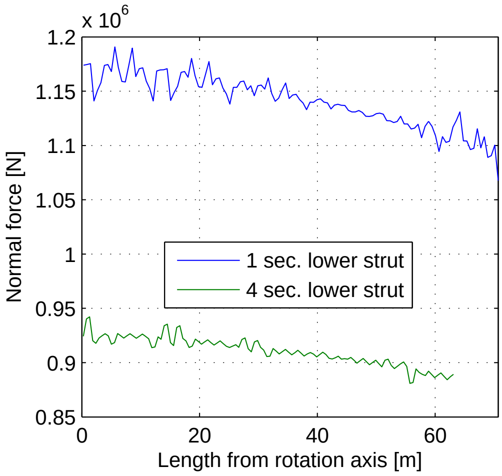

(a) Internal normal force.

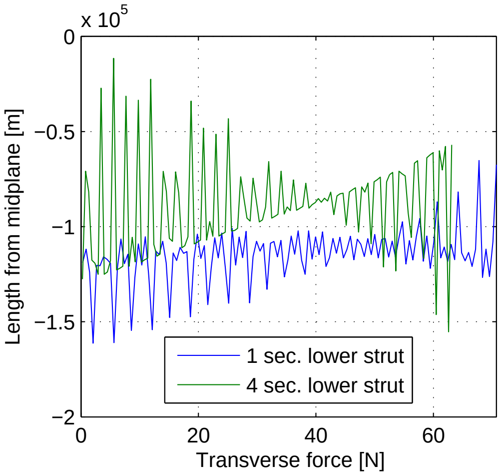

(b) Internal transverse force (in x-direction).

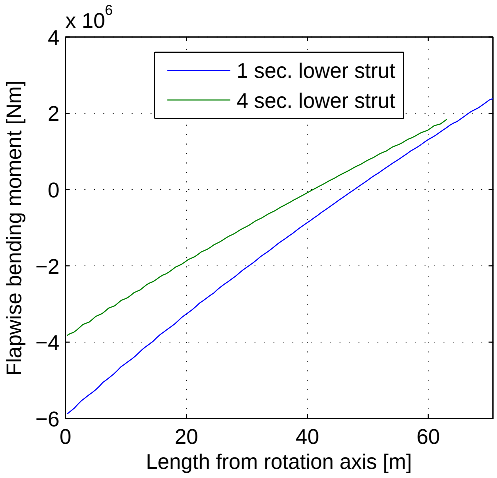

(c) Internal flapwise bending moment.

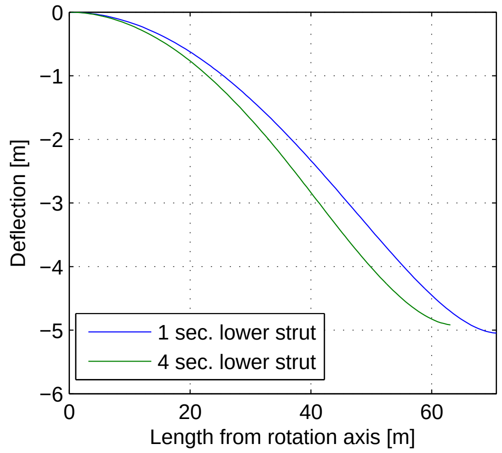

(d) Strut deflection (in x-direction).

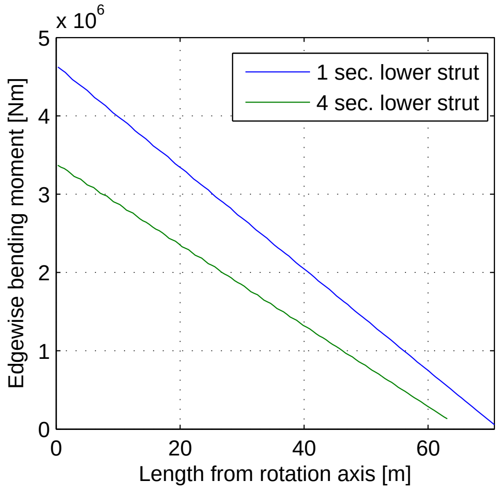

(e) Internal edgewise bending moment.

Figure F.5: Internal strut loads and strut deflection in normal operation conditions, downwind blade position.

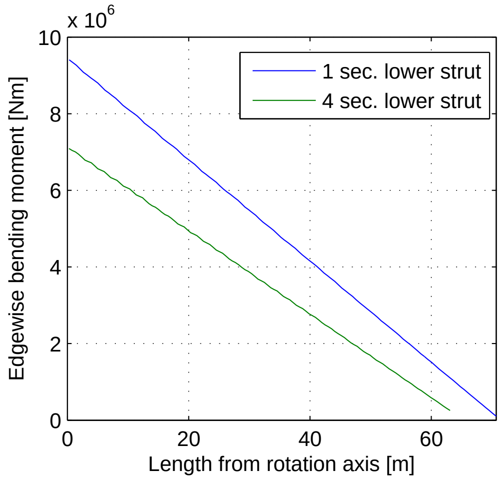

Figure F.6: Internal edgewise bending moment in the strut in normal operation conditions, upwind blade position.

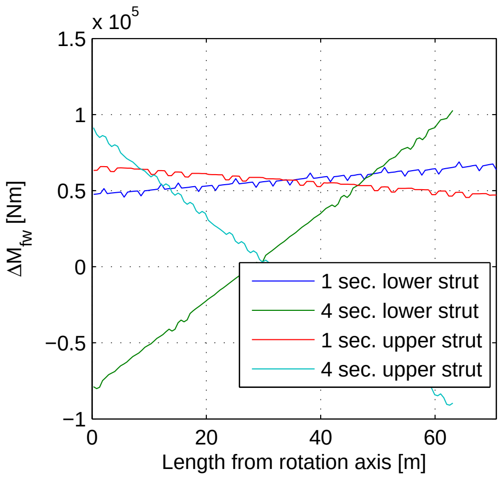

Figure F.7: Difference in flapwise bending moment in the strut between the up- and downwind position.

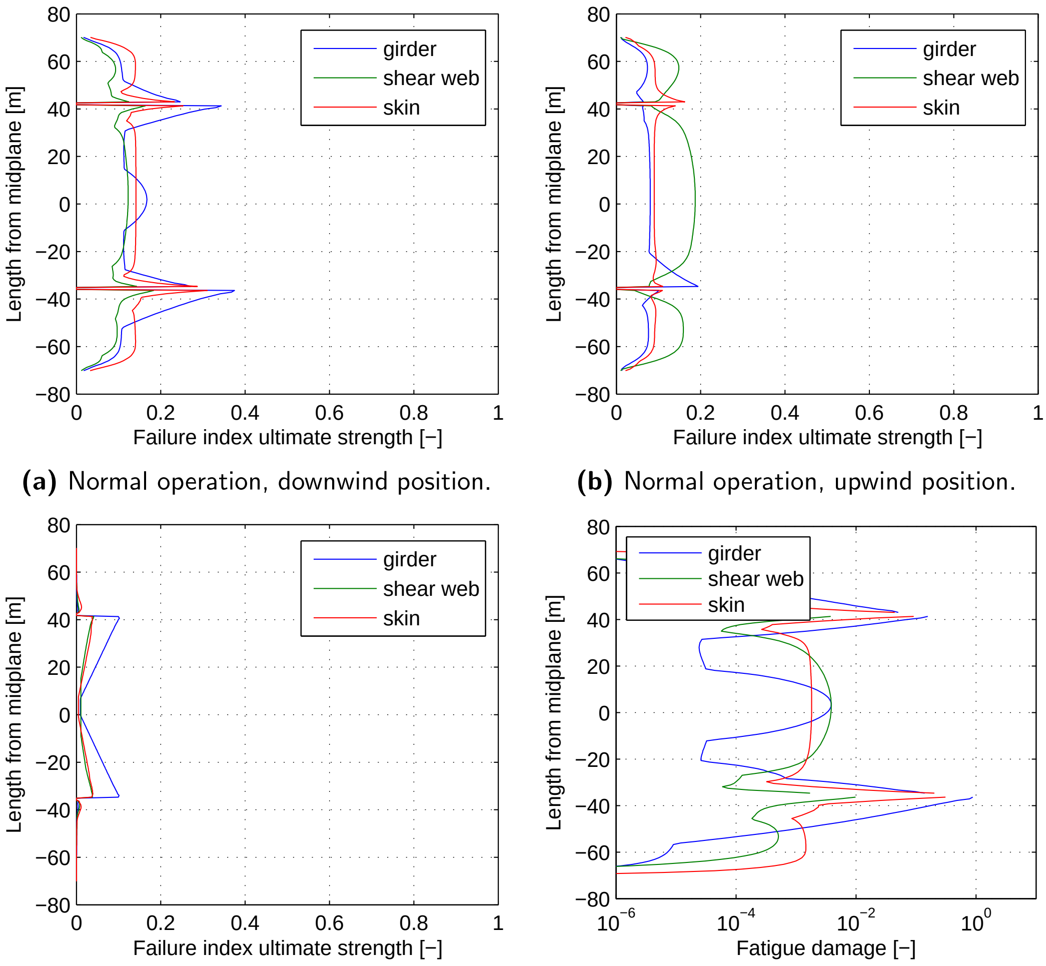

(a) Normal operation, downwind position.

(b) Normal operation, upwind position.

(c) Parked conditions.

(d) Fatigue.

Figure F.8: Failure indices of the structural members along the length of the blade: single section.

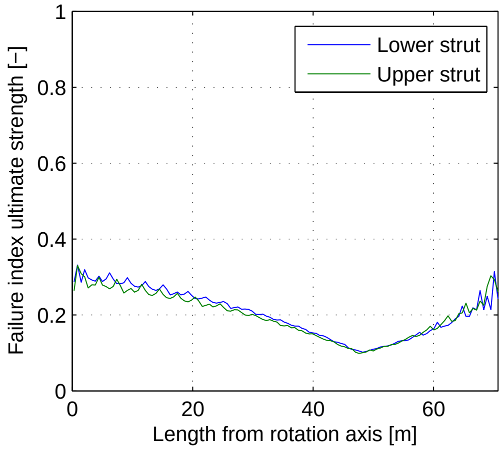

(a) Normal operation, downwind position.

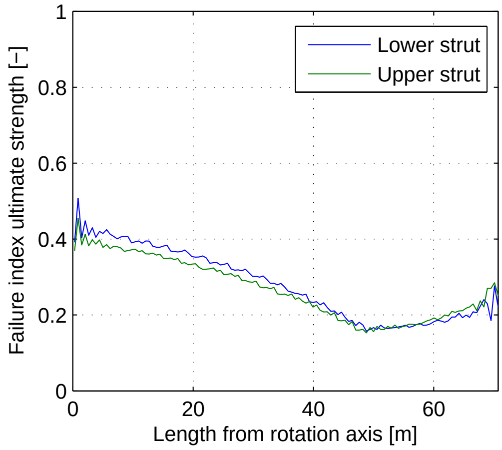

(b) Normal operation, upwind position.

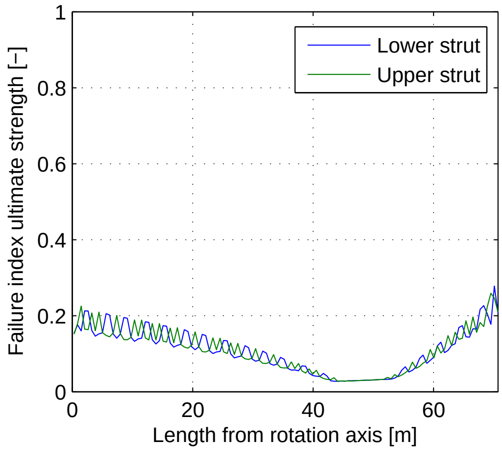

(c) Parked conditions.

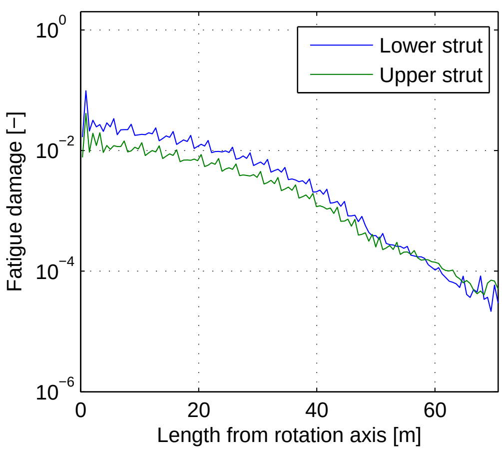

(d) Fatigue.

Figure F.9: Failure indices of the laminate along the length of the strut: single section.

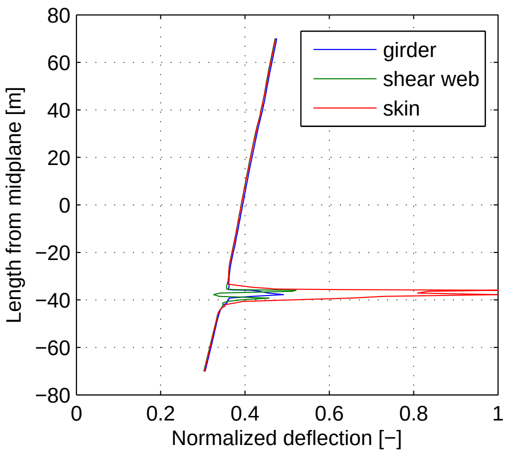

(a) First buckling mode; normal operation, downwind position (EV = 1.00).

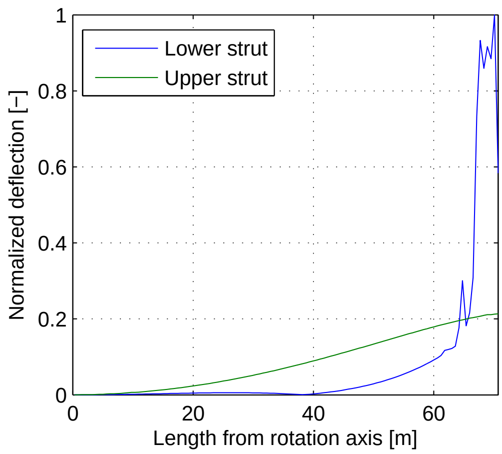

(b) First buckling mode (strut); parked conditions (EV = 2.01).

Figure F.10: Buckling deflections of the structural members: single section.

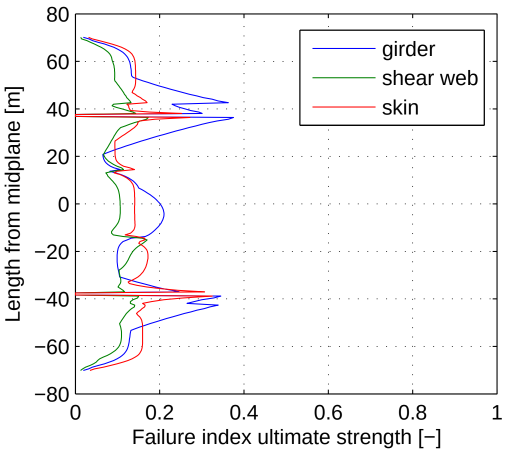

(a) Normal operation, downwind position.

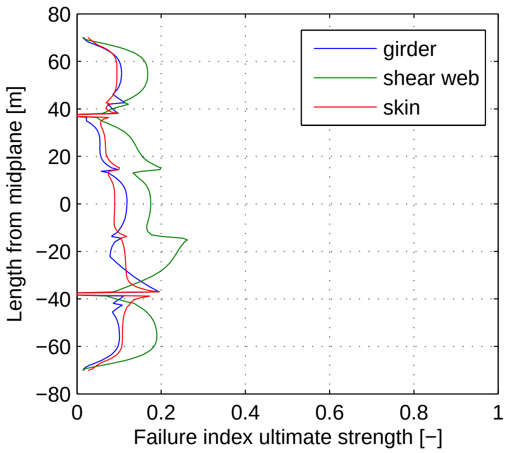

(b) Normal operation, upwind position.

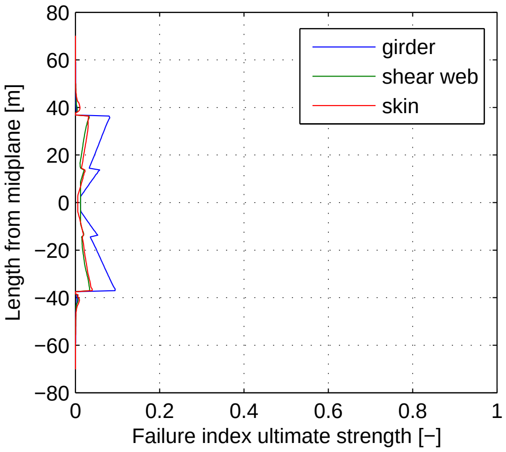

(c) Parked conditions.

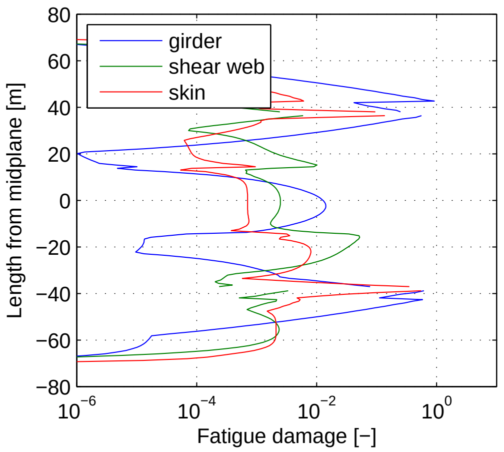

(d) Fatigue.

Figure F.11: Failure indices of the structural members along the length of the blade: 5 sections.

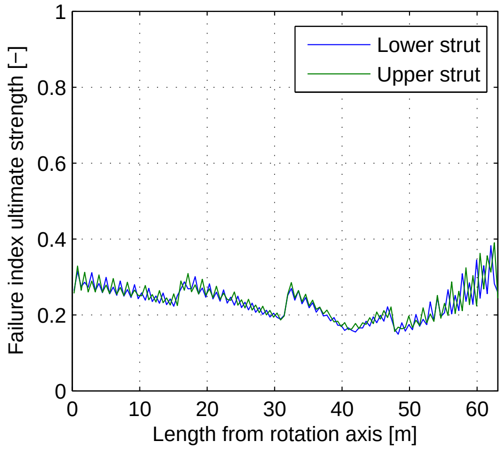

(a) Normal operation, downwind position.

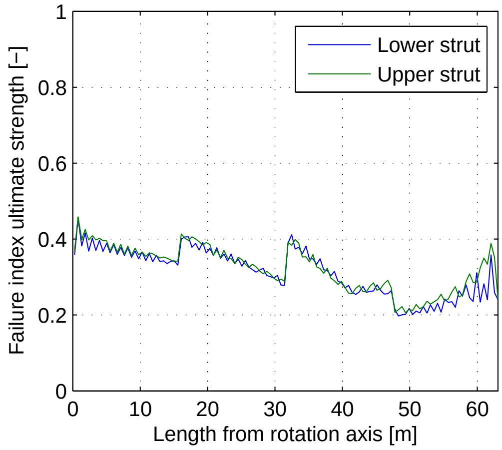

(b) Normal operation, upwind position.

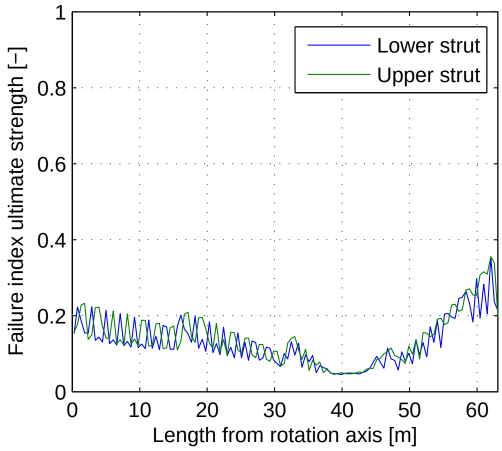

(c) Parked conditions.

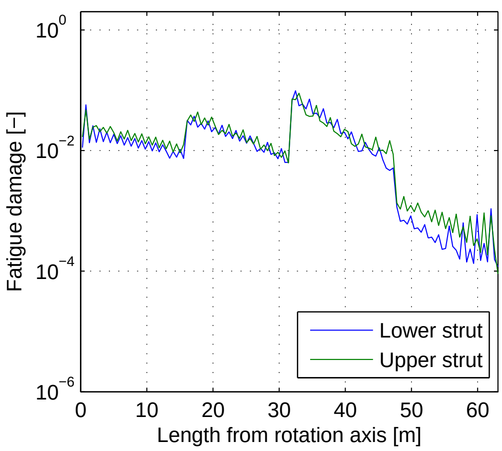

(d) Fatigue.

Figure F.12: Failure indices of the laminate along the length of the strut: 4 sections.

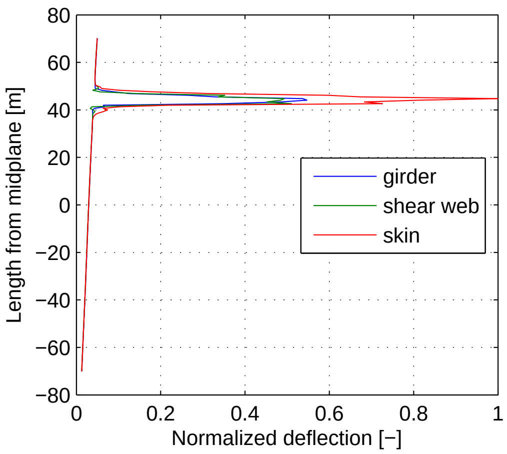

(a) First buckling mode; normal operation, downwind position (EV = 0.92).

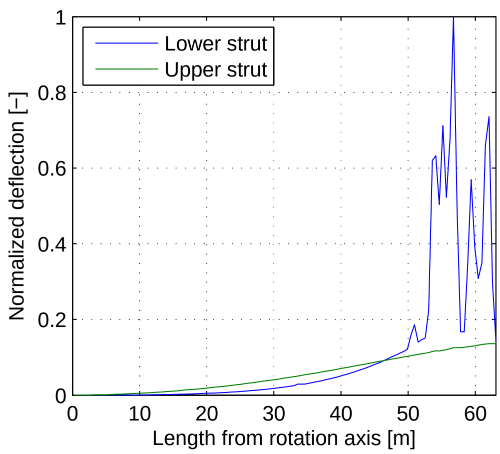

(b) First buckling mode (strut); parked conditions (EV = 1.25).

Figure F.13: Buckling deflections of the structural members: 5 sections.

Appendix G

Results combined optimization Darrieus rotor

In this appendix, plots of the internal loads and failure indices of the combined optimized Darrieus rotors are provided.

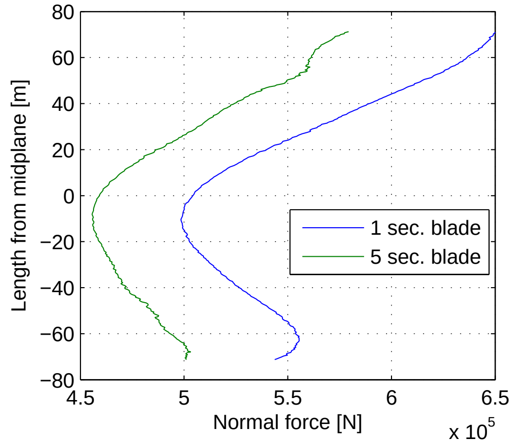

(a) Internal normal force.

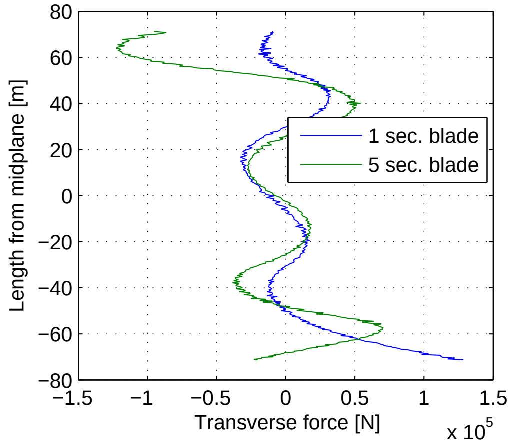

(b) Internal transverse force (in x-z plane).

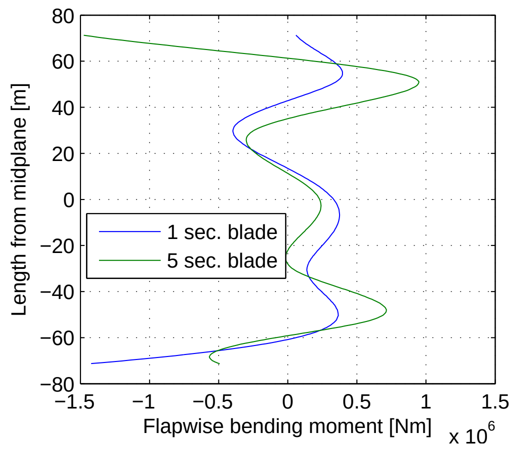

(c) Internal flapwise bending moment.

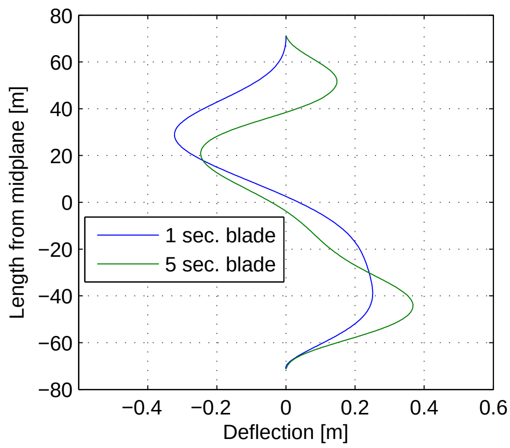

(d) Blade deflection (in z-direction).

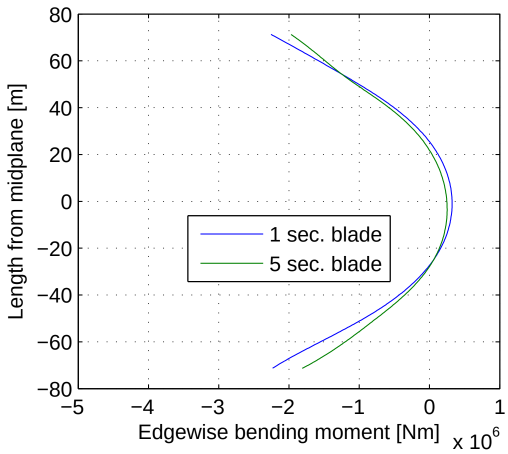

(e) Internal edgewise bending moment.

Figure G.1: Internal blade loads and blade deflection in normal operation conditions, downwind blade position.

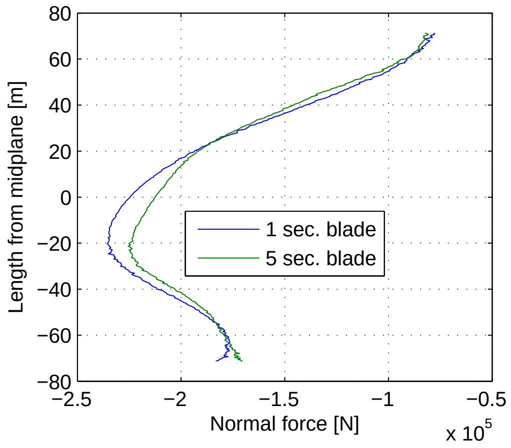

(a) Internal normal force.

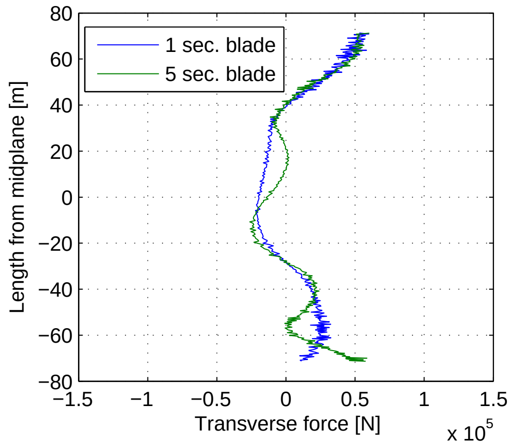

(b) Internal transverse force (in x-z plane).

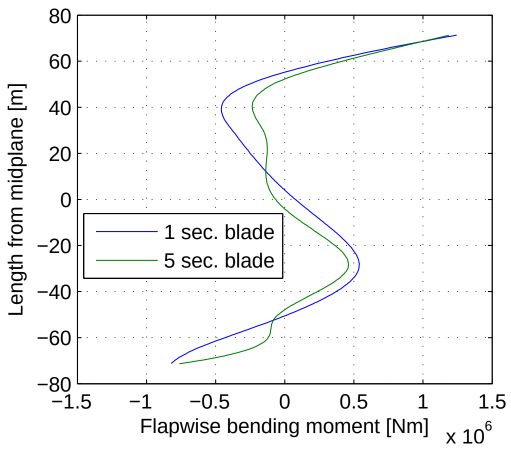

(c) Internal flapwise bending moment.

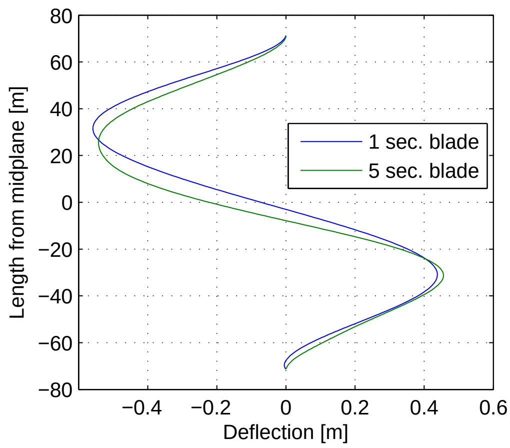

(d) Blade deflection (in z-direction).

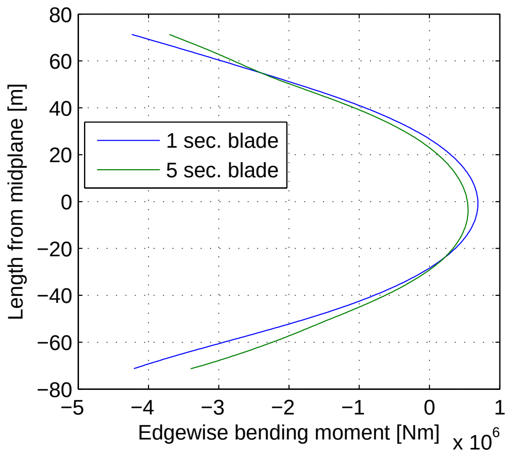

(e) Internal edgewise bending moment.

Figure G.2: Internal blade loads and blade deflection in normal operation conditions, upwind blade position.

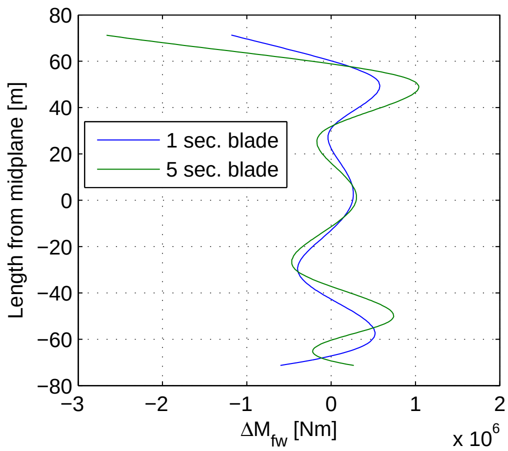

Figure G.3: Difference in flapwise bending moment in the blade between the up- and downwind position.

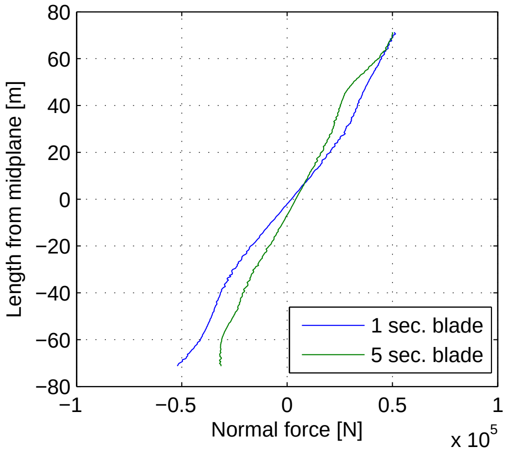

(a) Internal normal force.

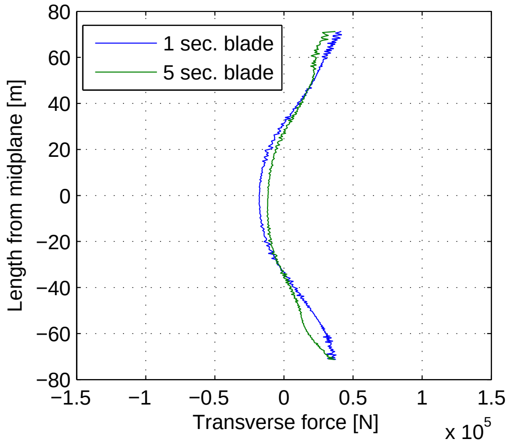

(b) Internal transverse force (in x-z plane).

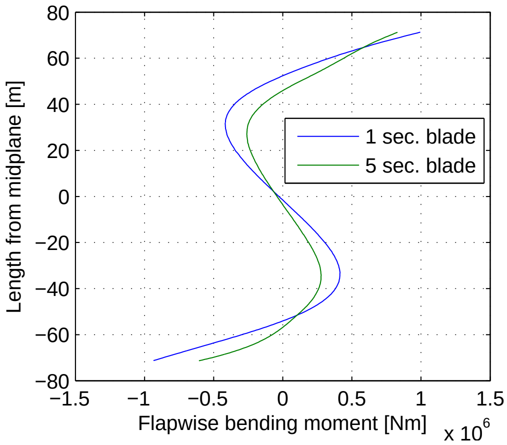

(c) Internal flapwise bending moment.

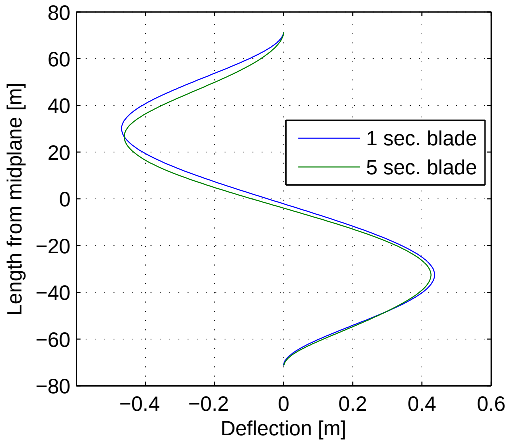

(d) Blade deflection (in z-direction).

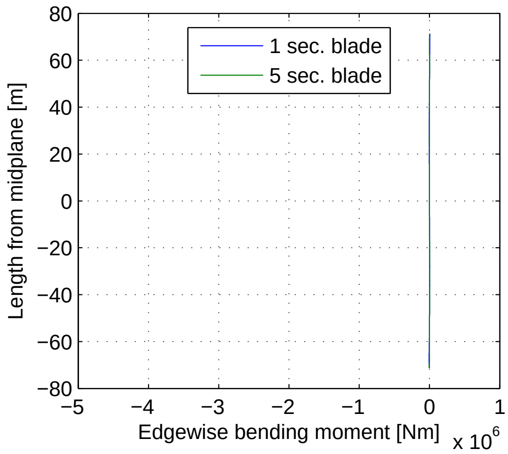

(e) Internal edgewise bending moment.

Figure G.4: Internal blade loads and blade deflection in parked conditions.

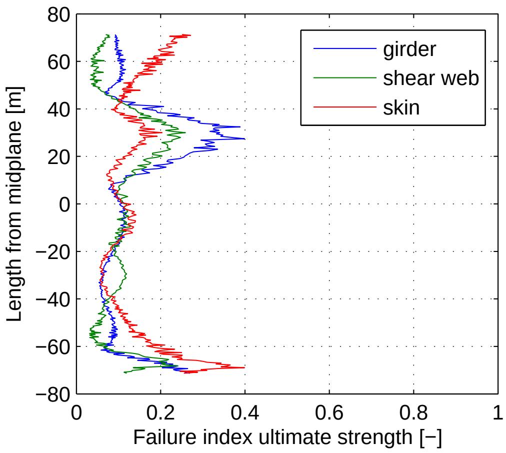

(a) Normal operation, downwind position.

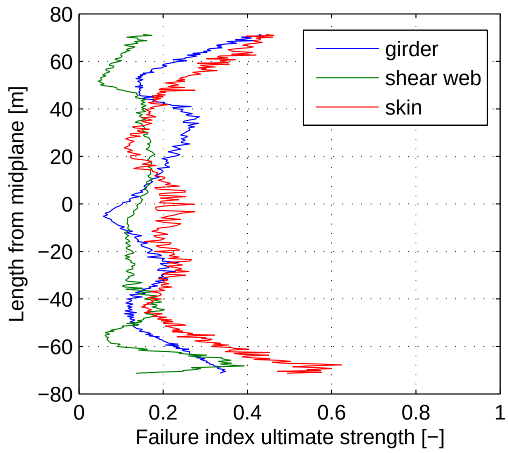

(b) Normal operation, upwind position.

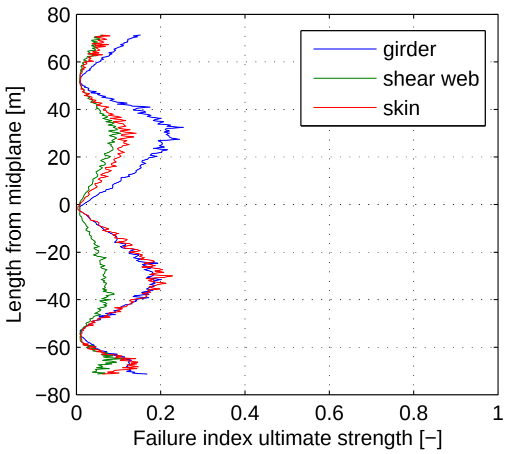

(c) Parked conditions.

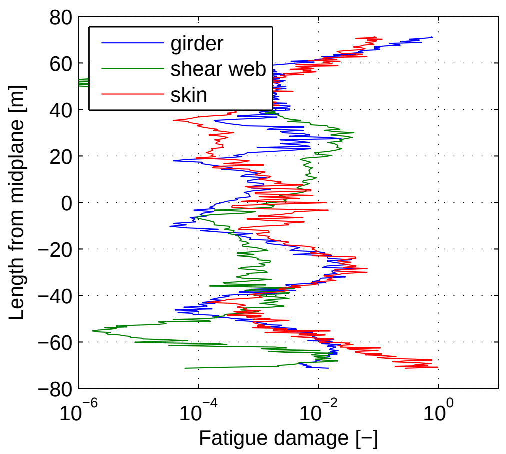

(d) Fatigue.

Figure G.5: Failure indices of the structural members along the length of the blade: single section.

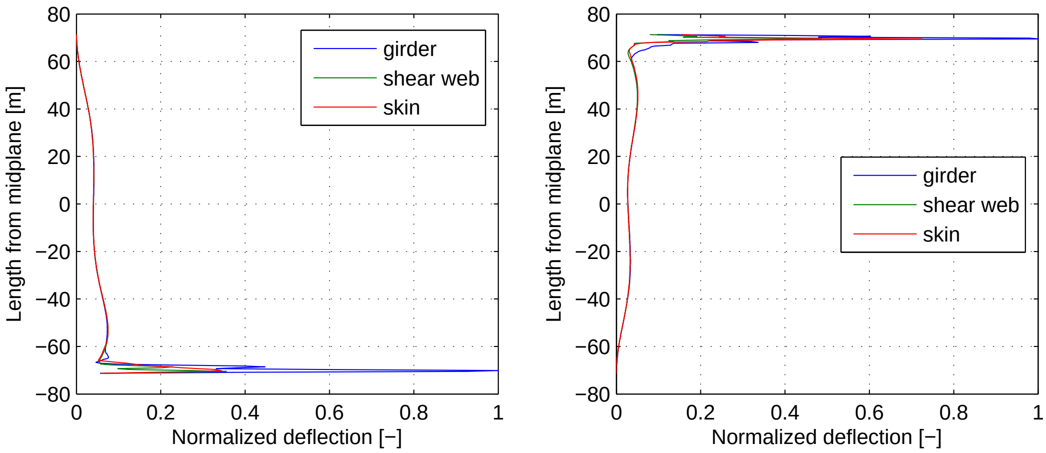

(a) First buckling mode; normal operation, downwind position (EV = 1.00).

(b) First buckling mode; parked conditions (EV = 1.00).

Figure G.6: Buckling deflections of the structural members along the length of the blade: single section.

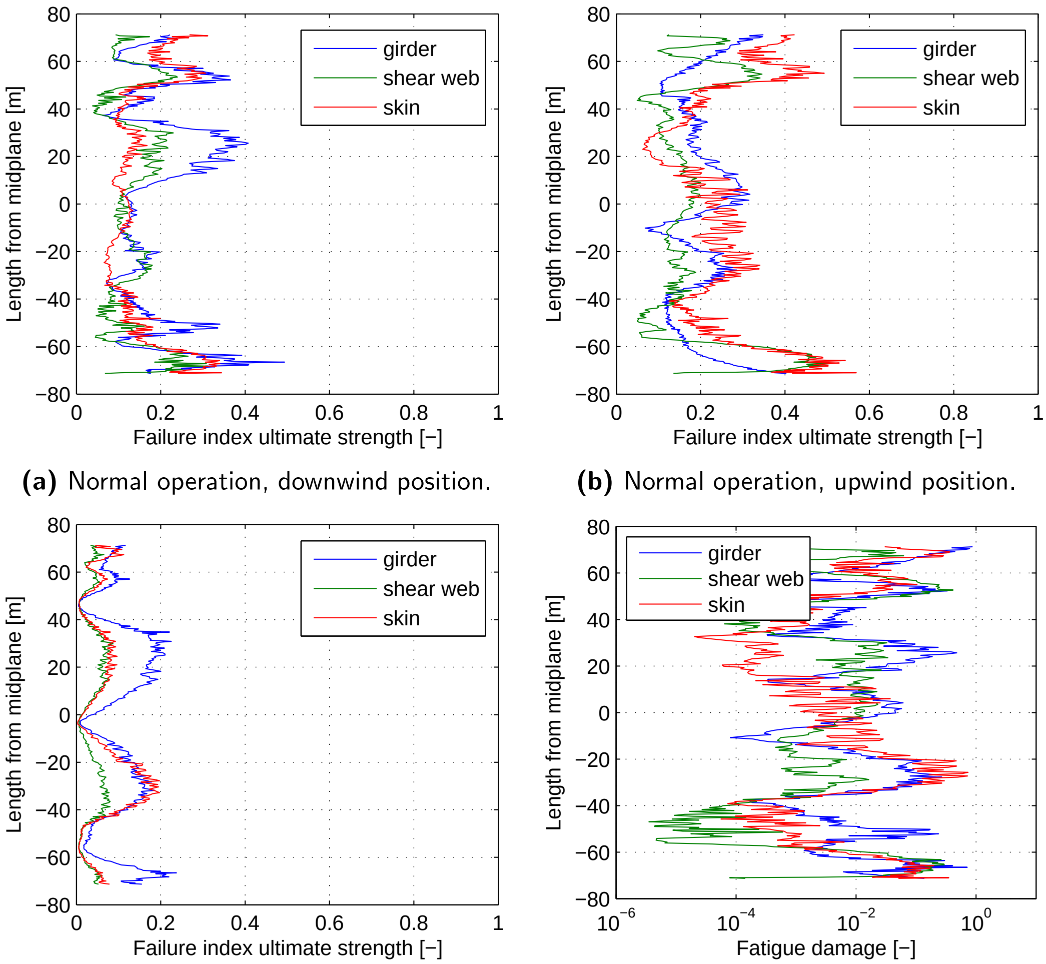

(a) Normal operation, downwind position.

(b) Normal operation, upwind position.

(c) Parked conditions.

(d) Fatigue.

Figure G.7: Failure indices of the structural members along the length of the blade: 5 sections.

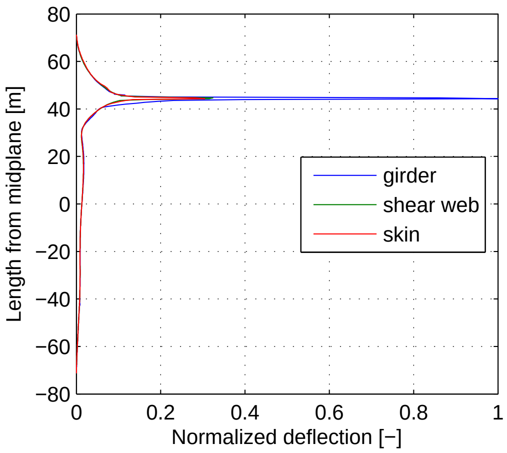

(a) First buckling mode; normal operation, downwind position (EV = 1.03).

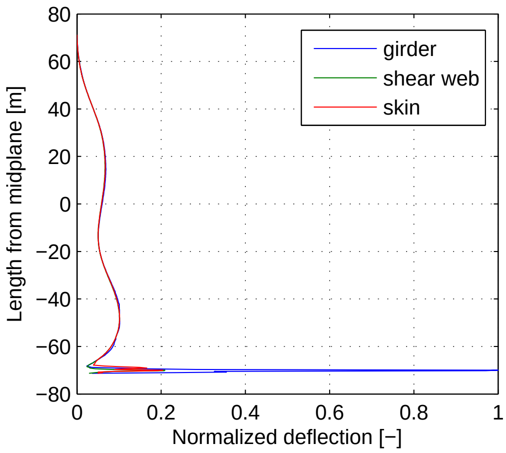

(b) First buckling mode; parked conditions (EV = 1.23).

Figure G.8: Buckling deflections of the structural members along the length of the blade: 5 sections.